Search for New Physics in Dielectron Events in 1.96 TeV Proton-Antiproton Collisions

March 2004

Koji Ikado

Submitted in partial fulfillment
of the requirements for
the degree of Doctor of Philosophy
in Waseda University

Preface

We have searched for new physics beyond the Standard Model of elementary particle physics in dielectron decay mode at the CDF (Collider Detector at Fermilab) experiment in $\bar{p}p$ collisions at $\sqrt{s} = 1.96$ TeV . The data were collected during the 2002-2003 runs corresponding to an integrated luminosity of 200 pb^{-1}. Many extensions of the Standard Model have been proposed. Grand Unified Theories (GUT) assumes a larger gauge symmetry group and predict new gauge bosons. GUT has the hierarchy problem in it and there have been many attempts to solve the hierarchy problem. Solutions for the hierarchy problem are supersymmetry, technicolor, large extra dimensions, warped extra dimensions and little Higgs models.

We analyze the differential distribution of dielectron events in terms of their invariant mass and no significant excess is found in very high mass region. We present a 95% confidence level limit on the production cross section times branching ratio for new resonant particles decaying into an electron pair as a function of invariant mass. New resonant particles include new neutral gauge boson Z', Randall-Sundrum graviton, R-parity violating sneutrino, and technicolor particles. We also present limits on the effective Planck scale of large extra dimensions.

Acknowledgments

I would like to thank Professor Kunitaka Kondo for his support throughout my graduate carrier. He provided me consistently good advice and helpful criticisms. I am grateful for him to careful reading of the text.

I wish to express the deepest appreciation to Dr. Kaori Maeshima, who has been my practical adviser for this analysis. Without her continuous guidance and encouragement in all phases of this work, this thesis could never be done.

Many people have helped me greatly in this analysis. Especially, I am grateful to Müge Karagöz Ünel and Tim Nelson for their continuous support and encouragement.

I want to thank Professor Shinhong Kim for his continued encouragement and support. He provided me with the opportunity to work at Fermilab. My special thanks go to Steve Worm, Stephan Lammel, John Conway and all other members of CDF exotic physics group for their encouragement and cooperation.

I would like to thank many CDF collaborators who have developed the detector and analysis environment. I wish to thank Yoshihiro Seiya for many fruitful discussions on physics. I would like to thank all members of the Tevatron accelerator group for their strong support on the experiments and their excellent accelerator operation. I would like to thank all members of High Energy Physics Group at Waseda University. I also want to thank Ichiro Ohba and Hiromichi Nakazato. They provided me with the opportunity to work for high energy experiment. I want to express my great appreciation to Carol Piccolo, Kyoko Kunori and Kazuko Kumashiro for their help through their secretary works.

Finally and most importantly I wish to thank my family for their constant support and encouragement.

This work was supported by the U.S. Department of Energy and National Science Foundation; the Italian Istituto Nazionale di Fisica Nucleare; the Ministry of Education, Culture, Sports, Science and Technology of Japan; the Natural Sciences and Engineering Research Coun-

cil of Canada; the National Science Council of the Republic of China; the Swiss National Science Foundation; the A.P. Sloan Foundation; the Bundesministerium fuer Bildung und Forschung, Germany; the Korean Science and Engineering Foundation and the Korean Research Foundation; the Particle Physics and Astronomy Research Council and the Royal Society, UK; the Russian Foundation for Basic Research; the Comision Interministerial de Ciencia y Tecnologia, Spain; work supported in part by the European Community's Human Potential Programme under contract HPRN-CT-20002, Probe for New Physics; and this work was supported by Research Fund of Istanbul University Project No. 1755/21122001.

Contents

List of Figures

List of Tables

Chapter 1

Introduction

1.1 The Standard Model

The Standard Model (SM) gives an excellent theoretical description of the strong and electroweak interactions. This theory, which is based on an $SU(3) \times SU(2) \times U(1)$ gauge group, has proven extraordinarily robust. We give a brief overview of the Standard Model. The Standard Model Lagrangian is

$$\begin{aligned} \mathcal{L} &= \bar{q} i \not{D} q + \bar{\ell} i \not{D} \ell - \frac{1}{4}(F^a_{\mu\nu})^2 \\ &\quad + (D^\mu \phi)^\dagger (D_\mu \phi) - V(\phi) \\ &\quad - (\lambda_u \bar{u}_R \phi Q_L + \lambda_d \bar{d}_R \phi^* Q_L + \lambda_\ell \bar{e}_R \phi^* L_L + \text{ h. c.}) \,. \end{aligned} \tag{1.1}$$

The first line contains only three parameters, three gauge couplings g_s, g, $g^{'}$ and it does correctly describe the couplings of all species of quarks and leptons to the strong, weak and electromagnetic gauge bosons. The second line is associated with the Higgs boson field ϕ. The Standard Model introduces one scalar field, a doublet of weak interaction $SU(2)$, so that its vacuum expectation value can give a mass to W and Z bosons. At this moment, there is no experimental evidence for the existence of the Higgs field. The third line gives an origin for masses of quarks and leptons. The Standard Model gauge symmetry allows three complex 3×3 matrices of couplings, the parameters λ. When ϕ acquires a vacuum expectation values, these matrices become the mass matrices of quarks and leptons. Figure 1.1 shows all terms of the standard electroweak model in a schematic way.

The $SU(3) \times SU(2) \times U(1)$ gauge theory gives an apparently complete description of elementary particles at those energies that we have probed experimentally. No clear evidence against the Standard Model from experimental data in high energy phenomena are found yet.

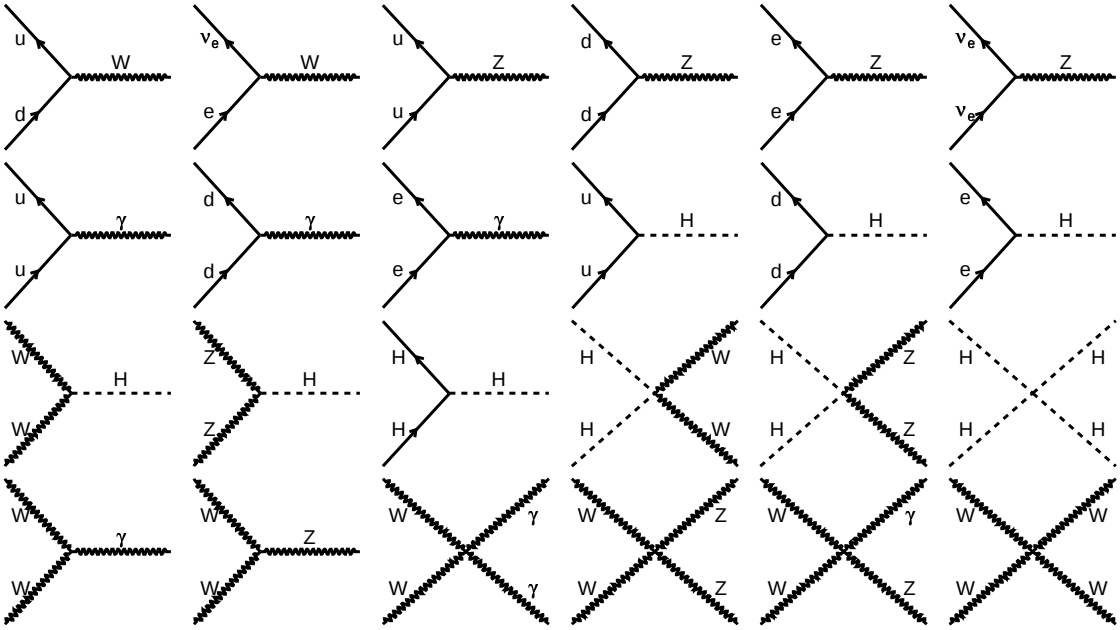

Figure 1.1: All terms of the standard electroweak interactions in a schematic way.

1.2 Grand Unification and New Gauge Bosons

The Standard Model leaves, however, unexplained why the gauge group of the strong and electroweak interactions is $SU(3) \times SU(2) \times U(1)$, with very different strengths and why the fermion quantum numbers have their particular values. The observed values of gauge coupling constants are larger for the larger components of the gauge group. If at some very large energy scale, these three couplings were equal, the values of $SU(3)$ and $SU(2)$ couplings would increase at smaller momentum scales due to the the asymptotic freedom, while the value of the $U(1)$ coupling would decrease, resulting in the observed pattern of couplings at low energies. The idea of Grand Unified Theories (GUT) is that $SU(3)$, $SU(2)$ and $U(1)$ are subgroups of a larger gauge symmetry group G and that quarks and leptons belong to the same multiplets of G. This higher symmetry is unbroken above some very large mass scale. Popular examples of a larger gauge group are the groups $SO(10)$ and E_6. The E_6 group is a subspace of the eight-dimensional root

space of E_8, which is the exceptional group of rank 8 and is spanned by eight unit vectors. The low energy gauge theories resulting from E_6 breaking can contain additional gauge bosons. The following breakdown of E_6 is one of the patterns of breakdown at the GUT scale to a subgroup with $U(1)$ factors :

$$\begin{aligned} E_6 &\rightarrow SO(10) \times U(1)_\psi \\ &\rightarrow SU(5) \times U(1)_\chi \times U(1)_\psi \\ &\rightarrow SU(3) \times SU(2) \times U(1) \times U(1)_\chi \times U(1)_\psi \end{aligned} \tag{1.2}$$

Thus there will be two additional neutral gauge bosons Z_ψ, Z_χ. The discovery of these new gauge bosons would be the cleanest signature for new physics beyond the Standard Model and would signal an extension of the gauge group by an additional factor such as $U(1)$. GUT is a natural way to extend the Standard Model, however, it has a crucial problem, so called the hierarchy problem.

1.3 The Hierarchy Problem

In the context of a GUT, there are two fundamental scales in nature, the electroweak scale ($M_{EW} \sim 10^3$ GeV) and the GUT scale ($M_{GUT} \sim 10^{16}$ GeV). One of the fundamental questions of physics is the large difference between the two scales. The hierarchy problem relates to the appearance of two very different mass scales, M_{EW} and M_{GUT}, in a GUT theory. This problem is related to the presence of fundamental scalar fields in the theory with quadratic mass divergences. Figure 1.2 shows one-loop radiative corrections contributing to the mass renormalization of a Higgs boson due to gauge boson, Higgs boson and top quark (fermions in general) loops. The mass of the Higgs particle receives self-energy corrections through quantum loop. Applied to the electroweak-breaking, Higgs mass becomes

$$M_H^2 = M_H^2(M_{GUT}) - Cg^2 M_{GUT}^2 \tag{1.3}$$

where g is a coupling and C is dimensionless constant. In order that the physical mass M_H be of order M_{EW}, there would have to be a cancellation between the terms on the right-hand side. This would require a fine-tuning of parameters to an accuracy of order 10^{-26} in each order of perturbation theory. These self-energy corrections to the Higgs mass can be made small only if parameters in the correction terms are fine tuned.

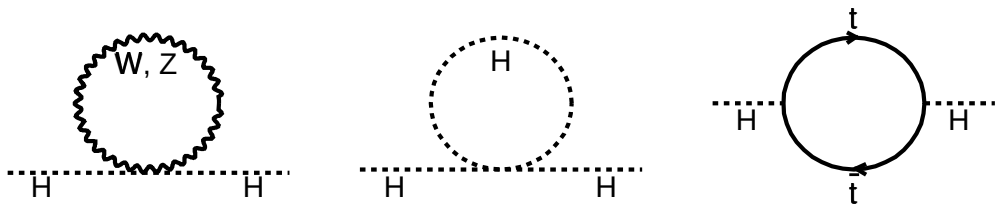

Figure 1.2: Radiative corrections to a Higgs boson mass from gauge bosons, scalar boson and fermion loops.

1.4 Solutions to the Hierarchy Problem

There have been many attempts to solve the hierarchy problem. Proposed classes of solutions for the hierarchy problem are as follows :

- Supersymmetry
- Technicolor
- Large extra dimensions
- Warped extra dimensions
- Little Higgs models

We give a brief overview of these new physics as a solution for the hierarchy problem in the following sections.

1.4.1 Supersymmetry

Supersymmetry (SUSY) is a new kind of symmetry which interrelates fermions and bosons. The MSSM, the minimal supersymmetric extension of the Standard Model, has a well defined multiplet structure with superpartners for all the Standard Model states and two Higgs doublet chiral superfields. Computing the radiative corrections to the gauge couplings coming from the virtual states of the MSSM one find that the $SU(3)$, $SU(2)$ and $U(1)$ couplings becomes very nearly equal at the scale 10^{16} GeV, a value consistent with the solution to the hierarchy problem.

If boson-fermion pairs have identical couplings, their contributions to the loop diagrams like Figure 1.2 are of opposite sign and cancel against each other.

1.4.2 Technicolor

The standard electroweak theory has many arbitrary parameters associated with the scalar Higgs field. Technicolor models represent an attempt to avoid this arbitrariness by replacing the Higgs scalar by composite ones. The composite scalars are meson bound states of a new strong interaction between new fermions. There are no fundamental scalar Higgs sector in Technicolor models, hence no quadratic divergences in the scalar potential. Technicolor is essentially a scaled up version of QCD. The pion decay constant F_π of the new strong interaction is required to be $F_\pi \sim 250$ GeV. This implies that the hadrons of new strong interactions would be at TeV energies, since in QCD the pion decay constant $f_\pi \sim 93$ MeV is of the order of Λ_{QCD}.

1.4.3 Large Extra Dimensions

In theories of large extra dimensions, the fundamental scale of gravity in $(4+n)$ dimensions could be quite different from the Planck scale [1][2][3]. A gravitational potential between two point masses within a distance $r \ll R$ in $(4+n)$ dimensions can be written as

$$V(r) \sim \frac{m_1 m_2}{M_s^{n+2}} \frac{1}{r^{n+1}} \tag{1.4}$$

where M_s is the effective Planck scale in $(4+n)$ dimensions. If the masses are placed at distances $r \gg R$, the usual $\frac{1}{r}$ potential is obtained,

$$V(r) \sim \frac{m_1 m_2}{M_s^{n+2} R^n} \frac{1}{r}. \tag{1.5}$$

This shows that the Planck scale of 4-dimensions (M_{Pl}) can expressed as

$$M_{Pl}^2 \sim M_s^{n+2} R^n. \tag{1.6}$$

The large size of the Planck scale may be due to the existence of new large dimensions. The hierarchy problem is resolved by taking M_s to be near TeV scale, which yields $R \sim 10^{30/n-19}$ meters.

1.4.4 Warped Extra Dimensions

An alternative higher dimensional scenario has been proposed by Randall and Sundrum [4][5], where the hierarchy is generated by an exponential function of the compactification radius. A 5-dimensional non-factorizable geometry is assumed. A Kaluza-Klein mode of graviton is created

with a scale $\Lambda_\pi = \bar{M}_{Pl} e^{-kr_c\pi}$, where $\bar{M}_{Pl}$ is the reduced effective 4 dimensional Planck scale, r_c is the compactification radius of the extra dimension and k is a scale of order the Planck scale. The geometrical exponential factor (called the warp factor) generates TeV scales from fundamental Planck scale and hence offers a solution to the hierarchy problem. The masses of the graviton resonances are given by $M_n = kx_n e^{-kr_c\pi} = x_n \left(k/\bar{M}_{Pl}\right) \Lambda_\pi$ where x_n are the roots of the Bessel function of order 1. The coupling of the massive resonances are given by $1/\Lambda_\pi$.

1.4.5 Little Higgs Models

Little Higgs models make the Higgs particle a pseudo-Nambu-Goldstone boson of a global symmetry[6][7][8][9]. The new ingredient of little Higgs models is that at least two interactions are needed to explicitly break all of the global symmetry. This forbids quadratic divergences in the Higgs mass at one-loop. Higgs mass is then smaller than the cutoff scale by two loop factors, making the cutoff scale $\sim$ 19 TeV natural ans solving the hierarchy problem.

1.5 Collider Phenomenology of New Physics

In this paper, we report results of an experimental search for new physics beyond the Standard Model with electron pairs. In $\bar{p}p$ collisions, these new physics can be detected via lepton pairs. Historically, studies of lepton-antilepton pair production have been important discovery channel for new physics. The J/ψ, Υ and Z resonances were all found in lepton pairs. The lepton-antilepton signature is a preferred channel for new physics searches in $\bar{p}p$ collisions, because of the relatively low backgrounds compared to hadronic decay channels. Especially, electrons permit a relatively straightforward trigger and their momentum can be measured precisely in high energies. We describe a short review of phenomenology of new physics in $\bar{p}p$ collisions below.

New Neutral Gauge Bosons Z'

As described in Section 1.2, additional $U(1)_\psi$ and $U(1)_\chi$ group lead to new gauge bosons, Z_ψ and Z_χ in E_6 models. Physically observable states of the new bosons can be expressed as a linear combination of Z_ψ and Z_χ with a mixing angle θ :

$$\begin{pmatrix} Z \\ Z' \end{pmatrix} = \begin{pmatrix} \cos\theta & -\sin\theta \\ \sin\theta & \cos\theta \end{pmatrix} \begin{pmatrix} Z_\psi \\ Z_\chi \end{pmatrix} \tag{1.7}$$

Certain values of the angle θ give rise to theoretically interesting cases. In E_6 models, 4 models are commonly considered, Z_ψ, Z_χ, Z_η and Z_I corresponding to θ of 0, $-\frac{\pi}{2}$, $\sin^{-1}\sqrt{\frac{3}{8}}$ and $\sin^{-1}\sqrt{\frac{5}{8}}$, respectively [10]. The neutral-current Lagrangian for $Z^{'}$ in the E_6 models at low energy can be written as :

$$\mathcal{L} = g\bar{f}\gamma^{\mu}\left(v_f^{'} - a_f^{'}\gamma_5\right) f Z_{\mu}^{'} \tag{1.8}$$

where the coupling factors, $v_f^{'}$ and $a_f^{'}$, can be calculated once the charge for the extra $U(1)$ is specified. Neglecting QCD radiative corrections, the width to a fermion pair is given by

$$\Gamma\left(Z^{'} \to \bar{f}f\right) = N_c\frac{g^2 M_{Z^{'}}}{12\pi}\left(1 - \frac{4m_f^2}{M_{Z^{'}}^2}\right)^{\frac{1}{2}}\left[v_f^{'2}\left(1 + \frac{2m_f^2}{M_{Z^{'}}^2}\right) + a_f^{'2}\left(1 - \frac{4m_f^2}{M_{Z^{'}}^2}\right)\right] \tag{1.9}$$

where N_c is a color factor ($N_c = 3$ for quarks and $= 1$ for leptons). With an assumption of $m_f/M_{Z^{'}} \ll 1$, the width can be written as

$$\Gamma\left(Z^{'} \to \bar{f}f\right) = N_c\frac{g^2 M_{Z^{'}}}{12\pi}\left(v_f^{'2} + a_f^{'2}\right) \tag{1.10}$$

Figure 1.3 shows Feynman diagram for $Z^{'}$ production and decay into lepton pair. The current best direct experimental $Z^{'}$ mass limits at 95% confidence level in $ee + \mu\mu$ modes are obtained from CDF Run I experiment (Table 1.1).

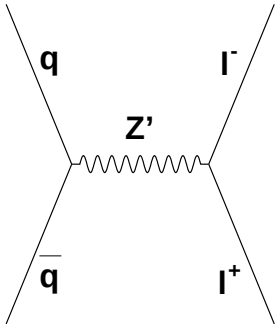

Figure 1.3: Feynman diagram for $Z^{'}$ production and decay into lepton pair.

Supersymmetry

Within the context of the MSSM, it is assumed that the discrete quantum number

$$R = (-1)^{2S+3B-L} \tag{1.11}$$

	ee (GeV)	$\mu\mu$ (GeV)	$ee + \mu\mu$ (GeV)
SM	655	590	690
χ	530	500	595
ψ	520	495	590
η	550	520	620
I	505	480	565

Table 1.1: The 95% C.L. lower mass limit for different $Z^{'}$ models from CDF Run I experiment.

is conserved, where L is the lepton number, B is the quark number and S is the spin. This quantity is called R-parity and it is constructed precisely so that $R = +1$ for the Standard Model particles while $R = -1$ for their supersymmetry partners. If R-parity is exactly conserved, supersymmetric particles can only be produced in pairs and the lightest supersymmetric partner must be absolutely stable. R-parity can be violated by adding terms which violate quark or lepton number. The possible R-parity violating (RPV) terms can be parametrized as

$$W = \lambda_{ijk} L_i L_j E^c_k + \lambda^{'}_{ijk} L_i Q_j D^c_k \tag{1.12}$$

where L_i and Q_i are the $SU(2)$ doublet lepton and quark superfields and E^c_i and D^c_i the singlet superfields. The coupling $\lambda^{'} LQD^c$ could give rise to sneutrino production in $\bar{p}p$ collisions and the coupling λLLE^c could give rise to sneutrino decay into lepton pairs. If both interaction terms are present in the superpotential, sneutrinos may decay into lepton pairs, $\bar{p}p \to \tilde{\nu} \to \ell^+\ell^-$ [11][12][13][14]. The cross section of stauneutrino exchange contributing $\bar{d}d$ annihilation is given by

$$\sigma = \frac{\pi\alpha^2 s}{12} \frac{(\lambda_{131}\lambda^{'}_{311}/e^2)^2}{(s - M^2_{\tilde{\nu}})^2 + \Gamma^2_{\tilde{\nu}} M^2_{\tilde{\nu}}} \tag{1.13}$$

Figure 1.5 shows the results of 95% C.L. upper limits on $\sigma \cdot Br(\tilde{\nu} \to e\mu)$, $\sigma \cdot Br(\tilde{\nu} \to e\tau)$ and $\sigma \cdot Br(\tilde{\nu} \to \mu\tau)$ as a function of sneutrino mass obtained from CDF Run I experiment[15]. Figure 1.4 shows Feynman diagram for sneutrino production and decay into lepton pairs.

Technicolor

One of Technicolor models, Technicolor Straw Man Model (TCSM), describes the phenomenology of color-singlet vector and pseudo-scalar technimesons and their interactions with the Standard Model particles[16][17]. These technimesons are expected to be the lowest bound states

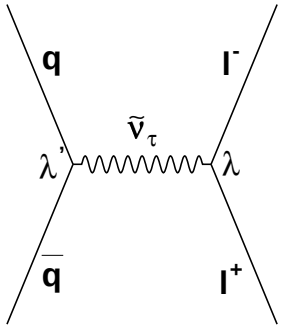

Figure 1.4: Feynman diagram for graviton production and decay into lepton pair.

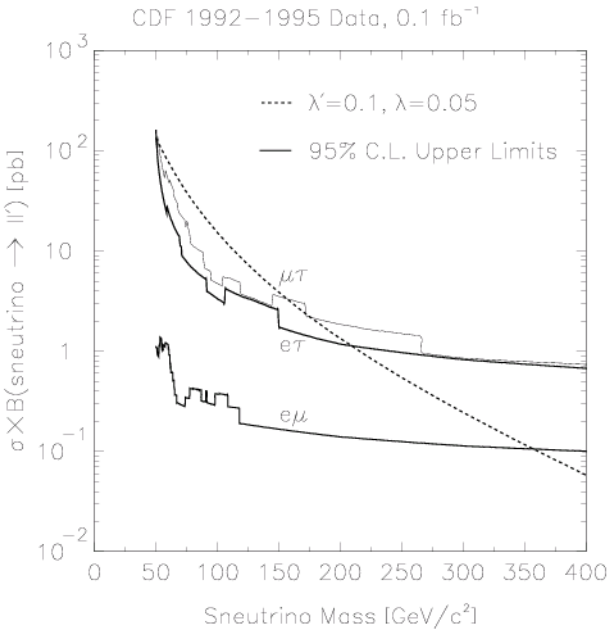

Figure 1.5: 95% C.L. upper limits on $\sigma \cdot Br(\tilde{\nu} \to e\mu)$, $\sigma \cdot Br(\tilde{\nu} \to e\tau)$ and $\sigma \cdot Br(\tilde{\nu} \to \mu\tau)$ as a function of sneutrino mass obtained from CDF Run I.

of the lightest technifermion doublet, T_U and T_D with components that transform under technicolor, but are QCD singlets. They have electric charges Q_U and $Q_D = Q_U - 1$. The vector technimesons form a spin-1 iso-triplet $\rho_T^{\pm,0}$ and an iso-singlet ω_T. Since techni-isospin is likely to be a good approximate symmetry, vector mesons ρ_T and ω_T are approximately mass degenerate. technifermions decay to lepton pairs may be an accessible signature in $\bar{p}p$ collisions : $\bar{p}p \to \rho_T, \omega_T \to \ell^+\ell^-$.

Large Extra Dimensions

In large extra dimensions theory, the effect of gravity is enhanced at high energies due to the accessibility of numerous excited states of the graviton (referred to as Kaluza-Klein modes of graviton). The graviton propagator is proportional to $\frac{1}{M_{Pl}^2}\sum\frac{1}{s-M_m^2}$ where M_m is mass of mth Kaluza-Klein mode. When summing over the m states, the total becomes an effective coupling of $1/M_s^2$:

$$\frac{1}{M_{Pl}^2}\sum\frac{1}{s-M_m^2} \to \frac{1}{M_s^4} \tag{1.14}$$

In $\bar{p}p$ collisions, graviton can be detected by the processes, $gg \to G \to e^+e^-$ and $\bar{q}q \to G \to e^+e^-$[18][19]. The effective cross section of virtual graviton exchange is given by

$$\sigma = \sigma_{SM} + \eta\sigma_{Int} + \eta^2\sigma_{KK} \tag{1.15}$$

where σ_{SM} is due to the Standard Model Drell-Yan diagram, σ_{Int} is the term of interference between the SM Drell-Yan and graviton exchange and σ_{KK} is purely the graviton exchange. The effect of large extra dimensions are parametrized via a single variable $\eta = \lambda/M_S^4$ where λ is a dimensionless parameter of order of ± 1 (this is called Hewett convention λ_{Hewett}). Two other convention of λ exist, Han-Lykken-Zhang (HLZ) [20] and Giudice-Rattazzi-Wells (GRW) [21] conventions. The relationship between the different conventions is the following :

$$\frac{2}{\pi}\lambda_{Hewett} = F_{GRW} = F_{HLZ} \tag{1.16}$$

where $F_{GRW} = 1$ and $F_{HLZ} = \frac{2}{n-2}$ for $n > 2$. Table 1.2 shows the 95% confidence level lower limits on effective Planck scale obtained from CDF Run I experiment dielectron decay mode.

Warped Extra Dimensions

The Randal-Sundrum model predicts a series of narrow heavy graviton resonances, while a continuous spectrum of Kaluza-Klein states is predicted in the concept of large extra dimensions

CDF Preliminary (110 pb^{-1})									
η_{95} (10^{-12}GeV^{-4})		Hewett (GeV)		HLZ (GeV)					GRW (GeV)
$\lambda<0$	$\lambda>0$	$\lambda<0$	$\lambda>0$	$n=3$	$n=4$	$n=5$	$n=6$	$n=7$	
1.74	2.3	826	808	1100	925	836	778	735	925

Table 1.2: The 95% C.L. lower mass limit on effective Planck scale from CDF Run I experiment.

due to the relation of 1.14. The processes $gg \to G \to e^+e^-$ and $\bar{q}q \to G \to e^+e^-$ are of interest in $\bar{p}p$ collisions[22][23]. One parameter, $k/\bar{M}_{Pl}$, appears in this scenario. $k/\bar{M}_{Pl}$ is a dimensionless coupling which enters quadratically in all partial width of the graviton resonance. the width to a fermion pair is given by

$$\Gamma(G \to \bar{f}f) = N_c \frac{2x_1^2 M_G}{320\pi} \left(\frac{k}{\bar{M}_{Pl}}\right)^2 \left(1 - 4\frac{m_f^2}{M_G^2}\right)^{\frac{3}{2}} \left(1 + \frac{8}{3}\frac{m_f^2}{M_G^2}\right) \tag{1.17}$$

where N_c is a color factor. With an assumption of $m_f/M_G \ll 1$, the width can be written as

$$\Gamma(G \to \bar{f}f) = N_c \frac{2x_1^2 M_G}{320\pi} \left(\frac{k}{\bar{M}_{Pl}}\right)^2 \tag{1.18}$$

where x_1 is the first zero of the Bessel function $J_1(x)$ of order 1. Figure 1.6 shows Feynman diagram for Randall-Sundrum graviton production and decay into lepton pairs. We consider only the production of the lightest massive graviton excitation. The Randall-Sundrum model is related to the large extra dimensions with

$$\frac{\lambda}{M_s^4} \to \frac{i^2}{8\Lambda_\pi^2} \sum_{m=1}^{\infty} \frac{1}{s - M_m}. \tag{1.19}$$

The production cross section of a 700 GeV first KK state at the Tevatron is shown in Figure 1.7 for various values of $k/\bar{M}_{Pl}$. No experimental limit on Randall-Sundrum graviton has been obtained yet.

Little Higgs Models

Little Higgs model consists of a nonlinear sigma model with a $SU(5)$ symmetry which is broken down to $SO(5)$ by a vacuum condensate. The gauged subgroup $[SU(2) \times U(1)]^2$ is broken at the same time to its diagonal subgroup $SU(2) \times U(1)$, identified as the SM electroweak gauge group. The breaking of the global symmetry leads to 14 Goldstone bosons, four of which are

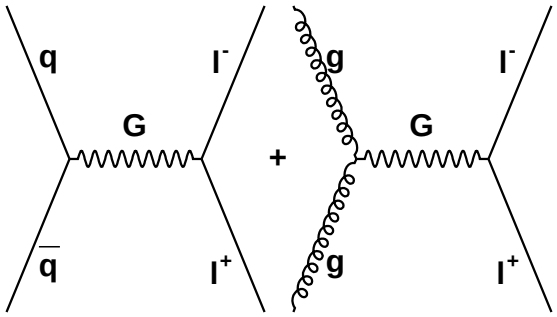

Figure 1.6: Feynman diagram for $\tilde{\nu}$ production and decay into lepton pair.

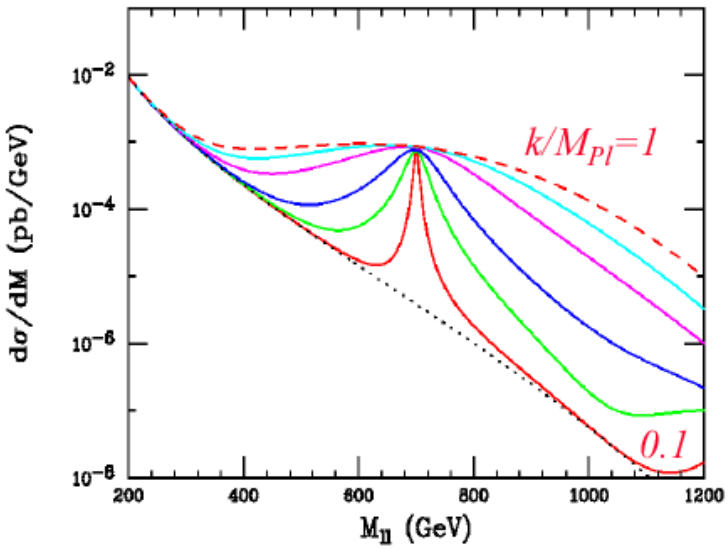

Figure 1.7: Production of a 700 GeV/c^2 first KK graviton for various values of $k/\bar{M}_{Pl}$ = 1, 0.7, 0.5, 0.3, 0.2 and 0.1 from top to bottom.

eaten by the broken gauge generators, leading to four massive vector bosons : an $SU(2)$ triplet Z_H, $W_H^{\pm}$ and a $U(1)$ gauge boson A_H[24]. The spontaneous gauge symmetry breaking gives masses for the gauge bosons, where the mass eigenstates are given by

$$\begin{aligned} W &= sW_1 + cW_2, \quad W' = -cW_1 + sW_2 \\ B &= s'B_1 + c'B_2, \quad B' = -c'B_1 + s'B_2 \end{aligned} \tag{1.20}$$

and the mixing angles are defined as

$$s = \frac{g_2}{\sqrt{g_1^2 + g_2^2}}, \qquad s' = \frac{g_2'}{\sqrt{g_1'^2 + g_2'^2}} \tag{1.21}$$

where g_i' and g_i are the couplings of the $[SU(2) \times U(1)]_i$ groups $(i = 1, 2)$. The W and B are the massless SM gauge bosons, with couplings given by

$$g = g_1 s = g_2 c, \qquad g' = g_1' s' = g_2' c'. \tag{1.22}$$

The new gauge bosons have the following couplings to the SM fermions :

$$\text{for } Z_H : g_V = -g_A = \frac{g}{2}\cot\theta\ T_3; \qquad \text{for } W_H : g_V = -g_A = \frac{g}{2\sqrt{2}}\cot\theta \tag{1.23}$$

where g_V and g_A are the vector and axial couplings and T_3 is the third component of the weak isospin. The heavy gauge boson Z_H can be produced via electron pairs. The cross section is proportional to $\cot^2\theta$ because the Z_H couplings to fermion pairs are proportional to $\cot\theta = \frac{g_2}{g_1}$. No experimental limit on little Higgs model Z_H has been obtained yet.

When we analyze the differential distribution of dielectron events of new particles in terms of their invariant mass, it is better to categorize these new particles. We can categorize these particles in terms of whether it has a resonant mass spectrum or continuous mass spectrum.

- Resonant mass spectrum :
  RPV sneutrino, Z', Z_H, ρ_T, ω_T and Randall-Sundrum graviton
- Continuous mass spectrum :
  Graviton of large extra dimensions

The resonant particles are classified into three groups in terms of spin.

- spin-0 : RPV sneutrino
- spin-1 : $Z^{'}$, Z_H, ρ_T and ω_T
- spin-2 : Randall-Sundrum graviton

We measure the cross section as a function of mass for resonant particles. The geometrical acceptance of these new resonant particles would be different because of the difference of their spin. We consider the measurement of the cross section for spin-0, spin-1 and spin-2 separately. For the large extra dimensions, we consider the measurement of the effective Planck scale.

Chapter 2

Tevatron and CDF Upgrades

This experiment was performed at the Fermi National Accelerator Laboratory (Fermilab) in Batavia, Illinois, U.S.A. The data used in this analysis were recorded by the Collider Detector at the Fermilab (CDF) during the 2002-2003 at $\sqrt{s}$ =1.96 TeV $\bar{p}p$ collisions. Protons and anti-protons are accelerated and collided by the Tevatron collider accelerator. The Tevatron accelerator and the CDF detector are described in this chapter.

2.1 A short history of CDF

The CDF experiment [25] aims at studying collisions between protons and anti-protons at the Tevatron accelerator, at center-of-mass energies up to $\sqrt{s} = 1.96$ TeV.

The first events were detected in 1985; during the subsequent eleven years, the increasing luminosity of the accelerator (Figure 2.1) and several improvements in the detector led to the accumulation of larger and more sensitive data samples:

—	1987	25 nb^{-1}
Run 0	1988-1989	4.5 pb^{-1}
Run 1a	1992-1993	19 pb^{-1}
Run 1b	1994-1996	90 pb^{-1}

Analyses of experimental data resulted in the publication of more than 170 papers, ranging over the entire spectrum of hadron collider physics. To cite but a few results, CDF provided the first experimental evidence for the top quark [26][27][28] and accurate measurements [29] of its mass, $m_t = 176.1 \pm 6.6\,\text{GeV}/c^2$; precision electroweak measurements, such as [30] $m_W = 80.433 \pm 0.079\,\text{GeV}/c^2$.

Since the shutdown in 1996, the Tevatron and its detectors – CDF and D0 – have undergone major upgrades. The rest of this chapter describes the various upgrades, and their impact on the physics program.

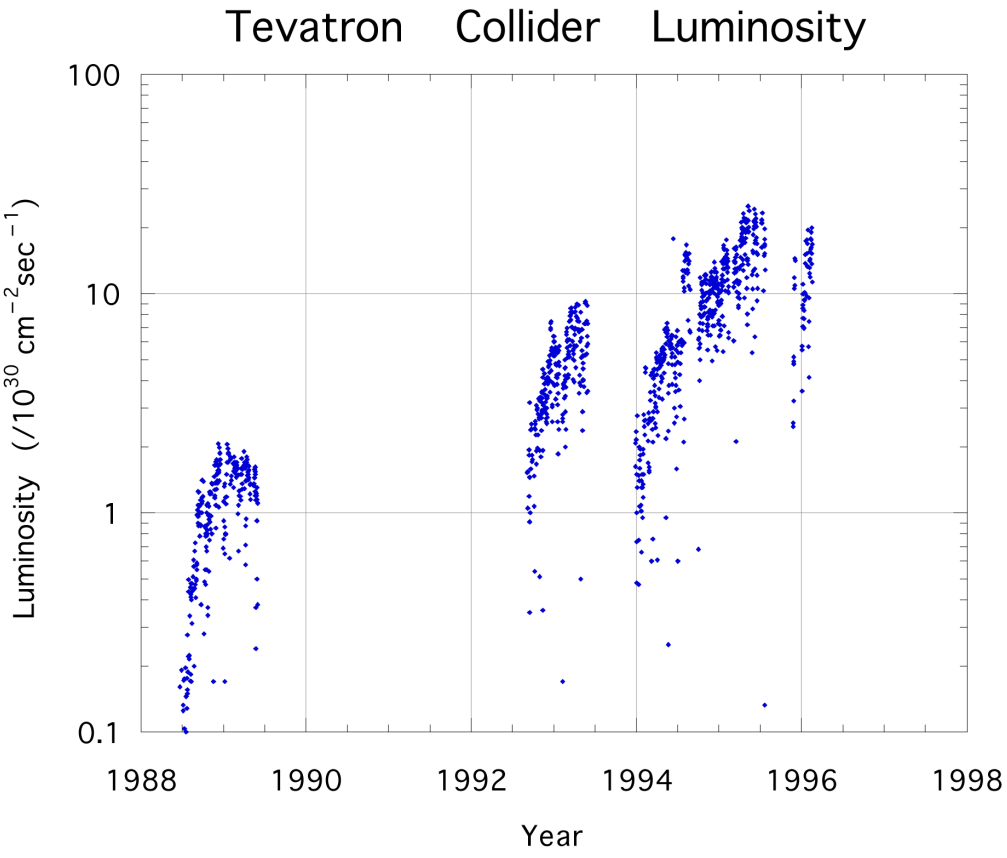

Figure 2.1: Tevatron's initial instantaneous luminosity in Run I.

2.2 The Accelerator Complex

In the next decade, CDF plans to carry out precise analyses of several rare physical processes whose cross section is several orders of magnitude smaller than the inelastic $p\bar{p}$ cross section. In order to obtain sufficiently large samples, several steps have been taken:

- Increase the center-of-mass energy
- Increase the luminosity

- Increase the detector's acceptance

The first two steps, and the partial reconstruction of the Tevatron which they implied, are the topic of this section.

As was stated above, the Run II proton-antiproton center of mass energy has increased to 1.96 TeV from the Run I value of 1.8 TeV. This change provides a major increase in the reconstructed sample size; for example, the cross section for associated $t\bar{t}$ production grows by 40% with respect to Run I.

Another way to obtain a larger sample is to increase the accelerator's luminosity. In the ideal case, where the proton and antiproton beams collide head-on without a crossing angle and with optimal alignment, the Tevatron's luminosity is given by the formula

$$\mathcal{L} = \frac{f B N_p N_{\bar{p}}}{2\pi(\sigma_p^2 + \sigma_{\bar{p}}^2)} F\left(\frac{\sigma_l}{\beta^*}\right) \tag{2.1}$$

where f is the revolution frequency, B the number of bunches in each beam, N_p and $N_{\bar{p}}$ the number of protons and anti-protons per bunch, σ_p and $\sigma_{\bar{p}}$ the transverse beam sizes (RMS) at the interaction point, and F a form factor that depends on the ratio between the bunch longitudinal RMS size, σ_l, and the beta function[1] at the interaction point, β^*.

As shown in Table 2.1 and Table 2.2, the most significant improvements in luminosity are obtained by increasing the number of bunches per beam from 6 to 36, and then to 108, while keeping the number of particles per bunch similar to or higher than the Run I figure.

A limiting factor in the choice of accelerator parameters is the superposition of multiple elementary proton-antiproton interactions within the same bunch crossing. At high luminosities, this superposition increases the complexity of the event, making its reconstruction more difficult.

Production and acceleration of protons and anti-protons at Fermilab requires a chain of accelerators, each boosting particles to higher energies. Each step will be described in the following pages.

2.2.1 Proton production and boosting

The process begins with a **Cockcroft-Walton** accelerator, which feeds negative hydrogen ions to a 150 m linear accelerator. The Linac itself was upgraded in 1993, increasing its energy from 200 MeV to 400 MeV; this made it possible, during Run Ib, to double the number of protons per bunch, and to increase by about 50% the production rate of antiprotons.

[1] Supposing the profile of the beam in the phase space (x, x') is an ellipse of semi-axes σ and σ', the *amplitude function* β is defined as the ratio σ/σ', while the beam *emittance* is the phase volume $\epsilon = \pi\sigma\sigma'$.

Run	1989	IA (1992-93)	IB (1993-95)
p/bunch	7.00E+10	1.20E+11	2.32E+11
$\bar{p}$/bunch	2.90E+10	3.10E+10	5.50E+10
p emittance (mm mrad)	25	20	23
$\bar{p}$ emittance (mm mrad)	18	12	13
Beta @@ IP (m)	0.55	0.35	0.35
Energy (GeV/particle)	900	900	900
Bunches	6	6	6
Bunch length (rms, m)	0.65	0.55	0.6
Form Factor	0.71	0.62	0.59
Typical $\mathcal{L}$ ($\mathrm{cm}^{-2}\mathrm{s}^{-1}$)	1.60E+30	5.42E+30	1.58E+31
Best $\mathcal{L}$ ($\mathrm{cm}^{-2}\mathrm{s}^{-1}$)	2.05E+30	9.22E+30	2.50E+31
$\int \mathcal{L}dt$ (pb^{-1}/week)	0.32	1.09	3.18
Bunch Spacing (nsec)	3500	3500	3500
Interactions/crossing	0.25	0.85	2.48
What's New?		Separators	Linac Upgrade
		$\bar{p}$ improvements	

Table 2.1: Evolution of Tevatron parameters. "Typical" luminosity is quoted at the beginning of a store.

Run	II (2001-)
p/bunch	3.30E+11
$\bar{p}$/bunch	3.60E+10
p emittance (mm mrad)	30
$\bar{p}$ emittance (mm mrad)	20
Beta @@ IP (m)	0.35
Energy (GeV/particle)	980
Bunches	36
Bunch length (rms, m)	0.43
Form factor	0.70
Typical $\mathcal{L}$ ($\mathrm{cm}^{-2}\mathrm{s}^{-1}$)	4E+31
$\int \mathcal{L}dt$ (pb^{-1}/week)	8
Bunch Spacing (nsec)	396
Interactions/crossing	2.17
What's New?	Main Injector
	$\bar{p}$ improvements

Table 2.2: Evolution of Tevatron parameters. "Typical" luminosity is quoted at the beginning of a store.

After being stripped of electrons, the protons enter the **Booster**, a synchrotron whose diameter is about 150 m, where they reach a kinetic energy of 8 GeV. Together, Linac and Booster are able to provide pulses of $5 \cdot 10^{12}$ protons for antiproton production every 1.5 s, or $6 \cdot 10^{10}$ protons per bunch in series of 5 to 7 bunches, repeated 36 times every four seconds.

After leaving the Booster, protons are transferred to the Main Injector, a newly built circular accelerator that replaced the older Main Ring.

2.2.2 Main Injector

The Main Ring was originally built to provide 400 GeV protons to Fermilab's fixed target experiments; later on, it was converted to act as an injector to the Tevatron. The new operational requirements for the Main Ring did not match its original design; therefore, during Run I, the Main Ring was a performance bottleneck. To quote an example, the Main Ring was never able to make full use of the Booster's capabilities: the Main Ring's aperture $(12\pi$ mm mrad$)^2$ is only 60% of the Booster's aperture (20π mm mrad). The situation would be even worse in Run II, with the Booster's aperture at injection increasing to 30π mm-mrad.

The **Main Injector** was designed to solve this problem, while providing further benefits. It is a 3-km circular accelerator, which brings protons and anti-protons from a kinetic energy of 8 GeV to a total energy of up to 150 GeV. Its transverse admittance is larger than 40π mm mrad, more than enough to accommodate particle bunches from the Booster; its emittance is about 12π mm mrad. The maximum beam size is $3 \cdot 10^{13}$ particles, divided into up to 504 bunches of $6 \cdot 10^{10}$ (anti)protons.

Being more flexible than the Main Ring, the Main Injector can be used in several operation modes:

- Antiproton production;
- Proton and antiproton boosting, before injection into the Tevatron in collider mode;
- Antiproton deceleration, in order to recover unused anti-protons after a Tevatron collision run;
- Proton and antiproton acceleration for fixed target experiments, either directly or as a booster for the Tevatron.

[2] All emittances are normalized at 95% of the beam.

2.2.3 Antiproton production

In order to produce anti-protons, a pulse of $5 \cdot 10^{12}$ protons at 120 GeV is extracted from the Main Injector and focused on a nickel target. A lithium lens collects the anti-protons produced by the collision, with a wide acceptance around the forward direction, at energies close to 8 GeV. The antiproton bunches are then moved to a **Debuncher Ring**, where they are transformed into a continuous beam and stochastically cooled, and then to the **Accumulator**, where they are further cooled. The antiproton stacking rate during Run I was about $7 \cdot 10^{10}$ $\bar{p}$/hour; Run II upgrades, ranging from antiproton cooling to improving the lithium lens, increases this rate by a factor of three to four.

When a sufficient number of anti-protons (up to 10^{12}) is available, stacking is suspended; the anti-protons are further cooled, and then transferred, with an aperture of 10π mm mrad and a $\Delta p/p < 10^{-3}$, to the antiproton Recycler Ring.

2.2.4 Recycler Ring

The **Recycler Ring** lies in the same enclosure as the Main Injector; contrarily to the other rings at Fermilab, it is built with permanent magnets. During Run I, the antiproton accumulation ring was found to suffer some kind of failure approximately once a week; this led to the loss of the entire store. Permanent magnets, not being prone to the most common causes of failure (such as power loss and lightning) provide a very stable repository for up to $3 \cdot 10^{12}$ anti-protons at a time.

During Run II, bunches of $2 \cdot 10^{11}$ recently produced anti-protons are transferred from the Accumulator to the Recycler Ring every about half an hour, thus keeping the total beam current in the Accumulator small (below 10 mA, compared to the 200 mA antiproton current in Run I).

Antiproton production is one of the limiting factors in the efficiency of Fermilab's colliders. At the end of a store, 75% of the antiprotons are expected to be still circulating in the Tevatron; by recycling 2/3 of these anti-protons, the average luminosity can be increased by a factor of two.

2.2.5 Tevatron

The Tevatron is about 6-km circular accelerator, where protons and anti-protons, rotating in opposite directions inside the same beam pipe, are accelerated from 150 GeV to 1 TeV. Making use of the upgrades in the rest of the accelerator chain, the Tevatron can provide an initial

luminosity of $5 \cdot 10^{31} \mathrm{cm}^2\,\mathrm{s}^{-1}$.

During a collider store, instant luminosity slowly decreases. In the early stages of the store, the most important cause for this decrease is intrabeam scattering; some hours later, the depletion of anti-protons during collisions becomes more relevant. Luminosity is expected to decrease to 50% in about seven hours, and to $1/e$ in twelve hours. After a typical store duration of eight hours, 75% of the antiprotons are still available; they are decelerated in the Tevatron and in the Main Injector, and then stored in the Recycler Ring and re-cooled Recycler is not used for the current $\bar{p}p$ collisions.

The Tevatron can also be used in fixed-target mode: it can accelerate up to $3 \cdot 10^{13}$ protons at a time to an energy of 800 GeV, and deliver single bunches to be used in proton, meson and neutrino experiments.

Other operational parameters of the Tevatron are listed in Table 2.1 and Table 2.2.

2.2.6 Beam monitors

Operation of colliders at the Tevatron requires a constant monitoring of the beam position and luminosity. From a conceptual point of view, this is done in Run II as it was done in Run I.

The luminosity monitor consists in two arrays of scintillators, placed on both sides of the interaction region. A coincidence of particles moving away from the interaction point, both in the p and $\bar{p}$ direction, is interpreted as a contribution to luminosity; bunches of particles moving in a single direction, without a coincident bunch in the opposite direction, are flagged as beam losses.

The beam position, on the other hand, is measured by the collider detectors themselves. During Run I, the detector was able to locate the beam within 5 μm in about five minutes; other beam parameters, such as slope and transverse profile, were calculated over longer time intervals (about two hours). In Run II, the same operations are performed more quickly.

2.3 CDF II : Overview

As stated above, one of the aims of Run II is to reconstruct and store a large sample of rare events. To achieve this result, the number of bunches in each beam increased first by a factor of six with respect to Run I. An immediate consequence is that the time between two successive interactions decreased by the same factor. Several parts of the detectors have been rebuilt from scratch in order to accommodate the higher collision rate.

While the detector was redesigned, efforts were also made to extend its acceptance. The geometrical coverage was increased, by adding new detector elements or enlarging the previously existing ones; the trigger system became able to detect some interesting event features at an earlier stage than in Run I, thus improving the signal to background ratio.

As shown in figure 2.2, the tracking system of CDF II is placed inside a superconducting solenoid, while calorimeter and muon systems are outside the magnet. The rest of this chapter will provide a short description of the detector subsystems, with an emphasis on the upgrades since Run I.

In the standard CDF geometry, the $\hat{z}$ axis is oriented along the axis of the solenoid, the $\hat{x}$ axis points away from the center of the Tevatron, and the $\hat{y}$ axis points up. The origin is at the interaction point. The polar angle θ is measured starting from the positive $\hat{z}$ axis; the rapidity y is defined by

$$y = \frac{1}{2} \ln \left(\frac{E + p_z}{E - p_z} \right) \tag{2.2}$$

For the high energy particles, $E \sim p$ and $p_z = p \cos\theta$, hence the pseudorapidity is defined as

$$\eta = -\ln \left(\tan \frac{\theta}{2} \right) \tag{2.3}$$

In hadron-hadron collisions, a rapidity y (or pseudorapidity η), a transverse momentum p_T and an azimuth angle ϕ are usually used. The invariant cross section is written as

$$E \frac{d^3\sigma}{d^3p} = \frac{d^3\sigma}{d\phi dy \; p_T dp_T} \rightarrow \frac{d^3\sigma}{\pi dy \; dp_T^2} \tag{2.4}$$

The second form is obtained using the identity $dy/p_z = 1/E$, and the third form represents the average over ϕ. The total multiplicity of particles in collisions is given by $d\sigma/dy$ and this means that the multiplicity is flat in η.

2.4 Tracking system

The innermost parts of the CDF II detector are devoted to tracking charged particles.

2.4.1 Silicon Vertex Detector

CDF II makes use of three concentric silicon detectors: "Layer 00" (**L00**), the Silicon Vertex Detector (**SVX II**, or **SVX** in short), and the Intermediate Silicon Layers (**ISL**).

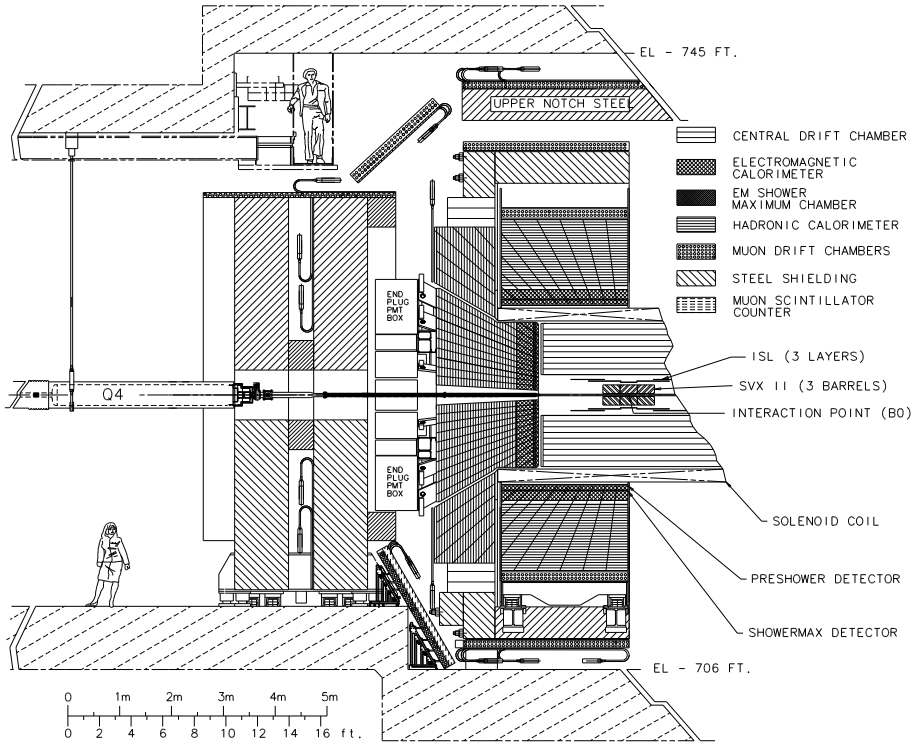

Figure 2.2: Elevation view of one half of the CDF II detector

SVX II is the Run II baseline detector. It consists of five layers of double-sided silicon wafers. One side of each wafer provides measurements in the transverse plane (axial strips); the other side's strips deliver 3D information. SVX II extends radially from 2.5 to 10 cm, and along z up to 45 cm on either side of the interaction point.

The ISL consists of a double-sided silicon layer, similar to those in SVX II, placed at $r =$ 22 cm in the central η region, and of two forward layers ($1 < |\eta| < 2$) respectively at 20 and 29 cm from the beam line. Together with SVX II, the ISL makes it possible to reconstruct tracks in the forward region, which lies beyond the acceptance region of the outer tracker.

Layer 00 is the most recent addition to the CDF II tracker. It is a single sided, radiation–hard silicon layer, placed immediately outside the beam pipe, at $r \simeq 1.5$ cm. Being so close to the interaction point, Layer 00 improves noticeably the impact parameter resolution. In case the innermost SVX II layer suffers from radiation damage during Run II, Layer 00 also acts as a backup.

Compared to the shorter, 4-layer, single-sided vertex detector of Run I, the new silicon tracker provides a much wider acceptance, better resolution, three-dimensional reconstruction, and can be used in stand-alone mode, without input from the Central Outer Tracker (described hereafter).

2.4.2 Central Outer Tracker

Outside the silicon detector, at a distance between 40 and 138 cm from the beam, lies the Central Outer Tracker. It is a new open-cell drift chamber, able to reconstruct tracks in the $|\eta| < 1$ region. The COT replaces an older drift chamber, the CTC [32], that would have been unable to cope with the expected occupancy and event rate of Run II.

Each of the eight superlayers of cells consists of twelve layers of sense wires, alternating with field-shaping wires. Axial superlayers alternate with stereo superlayers, thus providing 48 axial and 48 stereo measurements for each track.

In the COT, the cell size is roughly four times smaller than in the CTC. Usage of a faster gas (Ar – Ethane – CF_4 instead of Ar – Ethane) reduces the maximum drift time by a further factor of two, down to 100 ns. This makes the COT immune from event pile-up, even at the highest collision rate of 1/(132 ns).

2.4.3 Time of flight

A recent addition to CDF II, the time-of-flight detector is an array of scintillator bars, placed at the outer edge of the COT, at a radial coordinate of 140 cm. An accurate measurement of a particle's time of flight in the CDF tracking volume can be used quite effectively in particle identification.

Scintillator bars are about three meters long, matching the COT active volume; their thickness (4 cm) is limited by the space which remained available between the previously designed COT and magnet. Their width was determined by occupancy[3] and resolution considerations; the best choice turned out to be also of the order of 4 cm. The bars have a trapezoidal cross section, in order to minimize cracks in the geometry; the scintillating material is Bicron 408, which has a short rise time and a long (380 cm) attenuation length.

Photomultiplier tubes, attached to both ends of each bar, provide time and pulse height measurements. By comparing the two pairs of results, the detector determines the instant in which a particle crossed the scintillator with an accuracy of about 100 ps, and the z coordinate of the intersection. The latter measurement is compared to the results of 3D track reconstruction in the inner tracking volume, to associate a time of flight to each track.

2.4.4 Magnet

The CDF tracking systems are enclosed in a superconducting solenoid, which provides a uniform magnetic field of up to 1.5 T along the detector axis, over a cylindrical fiducial volume 3.5 m long and 2.8 m in diameter.

The solenoid is built of an Al-stabilized NbTi superconductor, able to withstand currents up to 5000 A, and operating at liquid helium temperature. During most of Run I, the magnet operated at 4650 A, corresponding to a current density of 1115 A/m and a central field of 1.41 T.

Although the design lifetime of the solenoid was only ten years, it is possible to reuse the magnet during Run II. The cool-down procedures that were used during Run I limited mechanical stress to the coil, avoiding fatigue damage.

[3]Detector occupancy depends on the average number of superimposed interactions, which increases with luminosity. TOF occupancy is estimated to be 0.1 with 2 superimposed events, and 0.4 with 10 events.

2.5 Calorimetry

2.5.1 Overview

CDF uses scintillator sampling calorimeters, divided into separate electromagnetic and hadronic sections, and providing coverage for $|\eta| \leq 3.64$. The calorimeter was an essential tool in selection and reconstruction of events in Run I; in Run II it continues to measure the energy of photons, electrons, jets, and the missing transverse energy [4] associated to neutrinos and possibly to neutral exotic particles.

Calorimeter calibration can be performed by matching the tracks found in the tracking system to the corresponding calorimetry towers; during Run I, this provided a 2.5% accuracy on jet energy measurements.

$\|\eta\|$ range	$\Delta\phi$	$\Delta\eta$
0 — 1.1 (1.2 had)	15°	0.1
1.1 (1.2 had) — 1.8	7.5°	0.1
1.8 — 2.1	7.5°	0.16
2.1 — 3.64	15°	0.2 — 0.6

Table 2.3: Calorimeter segmentation

The entire calorimeter is segmented into projective towers, whose geometry is summarized in table 2.3. Each tower consists of alternating layers of passive material (lead for the e.m. section, iron for the hadronic compartment) and scintillator tiles. The signal is read via wavelength shifters (WLS) embedded in the scintillator; light from the WLS is then carried to photo-multiplier tubes. Table 2.4 shows the most important characteristics of each calorimeter sector. The central and end-wall calorimeters ($|\eta| < 1.1$) [33] [34] were recycled from Run I; the plug ones ($1.1 < |\eta| < 3.64$) were built anew, to replace an older gas calorimeter that would not be able to function at the increased event rate of Run II.

2.5.2 Central calorimeter

Apart from the electronics, the central calorimeter in CDF Run II is the same used during Run I. The energy measurement response time is already fast enough to accommodate a 132 ns bunch spacing.

[4] Contrarily to e^+e^- colliders, in $p\bar{p}$ colliders the longitudinal momentum of the initial state is unknown.

	Central and End–wall	Plug
Electromagnetic:		
Thickness	19 X_0, 1 λ	21 X_0, 1 λ
– per sample (Pb)	0.6 X_0	0.8 X_0
– per sample (scint.)	5 mm	4.5 mm
Light yield	160 p.e./GeV	300 p.e./GeV
Sampling resolution	11.6% / $\sqrt{E}$	14% / $\sqrt{E}$
Stochastic resolution	14% / $\sqrt{E}$	16% / $\sqrt{E}$
Hadronic:		
Thickness	4.5 λ	7 λ
– per sample (Fe)	1 in (central)	2 in
	2 in (end–wall)	
– per sample (scint.)	6 mm	6 mm
Light yield	40 p.e./GeV	39 p.e./GeV
Resolution	$75\%/\sqrt{E} \oplus 3\%$	$80\%/\sqrt{E} \oplus 5\%$

Table 2.4: Characteristics of the CDF II calorimeter

Central electromagnetic calorimeter

The central electromagnetic calorimeter consists of projective towers of alternating lead and scintillator. The signal is read via a PMMA[5] wavelength shifter, and carried via clear fiber to photomultiplier tubes. None of these is expected to suffer much from radiation damage. The light yield loss is expected to be around 1% per year; 60% of this loss is explained by the gradual shortening of the attenuation length in the scintillator.

A two-dimensional wire chamber is embedded in the calorimeter, as a shower maximum detector (CES). Its usage in the Run I trigger decreased the fake electron trigger rate by a factor of two [35].

Another wire chamber is placed immediately in front of the calorimeter, to act as a pre-shower detector (CPR) which uses the tracker and the solenoid coil as radiators. The CPR has proven to be extremely useful in rejection of electron background; it also reduced systematic uncertainties for direct photon measurements by a factor of three [36].

Central hadronic calorimeter

The central and end-wall hadronic calorimeters use 23 iron layers as radiator. The scintillator should not suffer radiation damage from measured events.

The hadronic compartment geometry matches the projective towers of the electromagnetic calorimeter.

2.5.3 Plug calorimeter upgrade

The CDF II plug calorimeter, shown in figure 2.3, covers the η region between 1.1 and 3.64, corresponding to polar angles between 37° and 3°. It replaces an older gas calorimeter, whose response speed was too slow for usage at the CDF II 132 ns interbunch. Being based on the same principles as the central calorimeter, the new plug calorimeter also makes experimental data more homogeneous.

The calorimeter is divided in 12 concentric η regions, which are further segmented in 24 (for $|\eta| < 2.11$) or 12 (for $|\eta| > 2.11$) projective towers.

[5]PMMA = polymethylmethacrylate

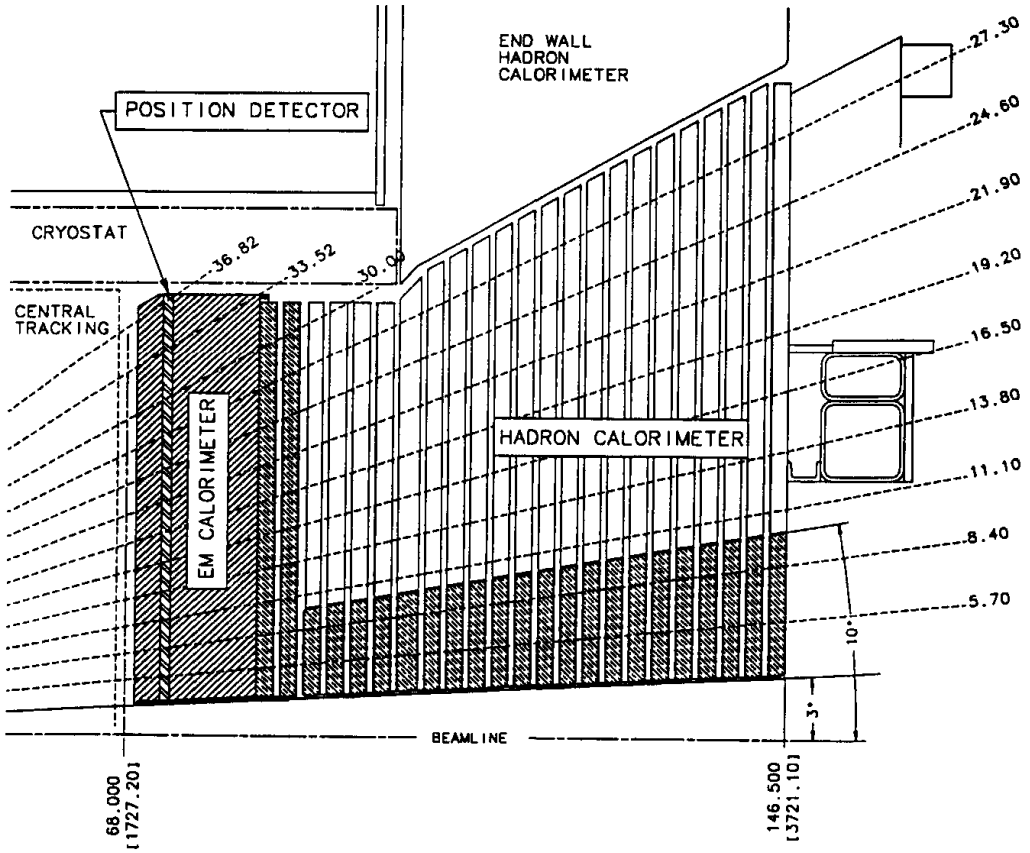

Figure 2.3: Cross section of half CDF II plug calorimeter

Plug electromagnetic calorimeter

The EM section of the plug calorimeter consists of 23 absorber-scintillator layers. A calcium-tin-lead alloy, enclosed between steel plates, is used as absorber.

The first layer of the EM section is used as a preshower detector. In order to distinguish γ from π^0 reliably, the light yield needs to be higher than on other layers. Therefore, the first scintillator layer is thicker (10 mm instead of 6 mm) and made of a brighter material; it is read out separately from the rest of the calorimeter, via multi-anode photomultiplier tubes (MAPMT).

As in the central calorimeter, a shower maximum detector (PES) is also embedded in the plug EM calorimeter, at a depth of about six radiation lengths. The PES consists of eight 45° sectors, each covering six (or three) calorimetric towers in ϕ; each sector is further segmented in two η regions, in order to reduce occupancy. Within each region, scintillating strips are arranged on two layers, in directions parallel to either edge of the sector; this provides a two-dimensional measurement of the shower. The strips are 5 mm wide and 6 mm thick; they are read out via WLS fibers and MAPMT.

The PES is used to measure the position of electromagnetic showers with an accuracy reaching 1 mm for high-energy electrons, and to discriminate pions from photons and electrons.

Plug hadronic calorimeter

The hadron plug calorimeter was designed to optimize detector performance on b, electroweak and jet physics, and to help in muon detection by analyzing their rate of energy loss. It achieves an energy resolution of about $80\%/\sqrt{E} \oplus 5\%$, which is dominated by the sampling fluctuations from the steel absorber plates. The most strict requirement is that the light yield within each tile should be uniform to 4% or better; disuniformity between different tiles is not as important, as the hadron shower usually affects ten or more layers.

2.6 Muon chambers

The outermost component of CDF II is a set of scintillators, drift tubes and steel absorbers, used for the detection of muons.

During Run I, detection of muons has proven to be an important requirement, both for the analysis of several physics channels and for calibration. For example, a clean sample of W bosons is obtained by reconstructing their muon decay mode; $J/\psi \to \mu^+\mu^-$ decays are an important

part of the heavy quark physics program, as well as a tool to measure systematic effects in the detector.

The tracking improvements from Run I to Run II have a deep impact on muon detection. Before the upgrades, muons in the central region were identified by their penetrating power, and their momentum was measured in the central tracking chamber. On the contrary, the momentum of forward muons had to be measured in the muon chambers themselves, by resorting to a toroidal magnet, as the central tracker only covered the $|\eta| < 1$ region.

With the SVX II upgrade, this distinction falls: measurement of muon momentum can be performed in the central tracker, where the multiple scattering effects are smaller, and the toroidal magnets are not required any longer. Central tracks are measured in the drift chamber; forward tracks ($|\eta| > 1$) are tracked in the silicon only.

Run I central muon chambers (**CMU**) are reused without major changes; some upgrades which started under Run I (**CMP** and **CSP**, the Central Muon/Scintillator Upgrades; **CMX** and **CSX**, the Central Muon/Scintillator Extension) are completed; and a new set of chambers, the Intermediate Muon Detector **IMU**, replaces the previous Forward Muon Detectors (**FMU**)[37].

Due to their size, muon systems are unable to take data within the Run II interbunch interval of 400 or 132 ns; this is not a problem, since the low occupancy of the muon chambers allows integration over multiple events. Scintillators are used to associate muon stubs to the appropriate event.

Table 2.5 summarizes the information on the muon subsystems; the following sections will describe their characteristics in deeper detail.

2.6.1 Central muon detectors

The first muon system built at CDF, the **Central Muon Detector** (CMU) [38], is a set of 144 modules, each containing four layers of four rectangular cells. It is placed just outside the central hadronic calorimeter, whose 5.5 interaction lengths absorb more than 99% of the outgoing charged hadrons.

A second set of muon chambers, the **Central Muon Upgrade** (CMP), forms a square box around the CMU, and is shielded by an additional layer of 60 cm of steel. Due to the detector geometry, the η coverage varies with azimuth as shown in figure 2.4. The CMP consists of four layers of single-wire drift tubes, staggered by half cell per layer, and operated in proportional mode. On the outer surface of the CMP lies the **Central Scintillator Upgrade** (CSP), a layer

	CMU	CMP/CSP	CMX/CSX	IMU
η coverage	0 — 0.6	0 — 0.6	0.6 — 1.0	1.0 — 1.5
Drift tubes:				
thickness	2.68 cm	2.5 cm	2.5 cm	2.5 cm
width	6.35 cm	15 cm	15 cm	8.4 cm
length	226 cm	640 cm	180 cm	363 cm
max drift time	0.8 μs	1.4 μs	1.4 μs	0.8 μs
# tubes (Run Ib)	2304	864	1536	—
# tubes (Run II)	2304	1076	2208	1728
Scintillators:				
thickness	N/A	2.5 cm	1.5 cm	2.5 cm
width	N/A	30 cm	30 - 40 cm	17 cm
length	N/A	320 cm	180 cm	180 cm
# counters (Run Ib)	N/A	128	256	—
# counters (Run II)	N/A	269	324	864
π^0 int. lengths	5.5	7.8	6.2	6.2 — 20
Min P_t (GeV/c)	1.4	2.2	1.4	1.4 — 2.0
MS resol. (cm GeV)	12	15	13	13 — 25

Table 2.5: Parameters of muon detection at CDF. Pion interaction length and the limit on resolution due to multiple scattering are computed at $\theta = 90^\circ$ in the central detectors CMU, CMP and CSP; at $\theta = 55^\circ$ in CMX and CSX; and on the entire θ coverage for the IMU.

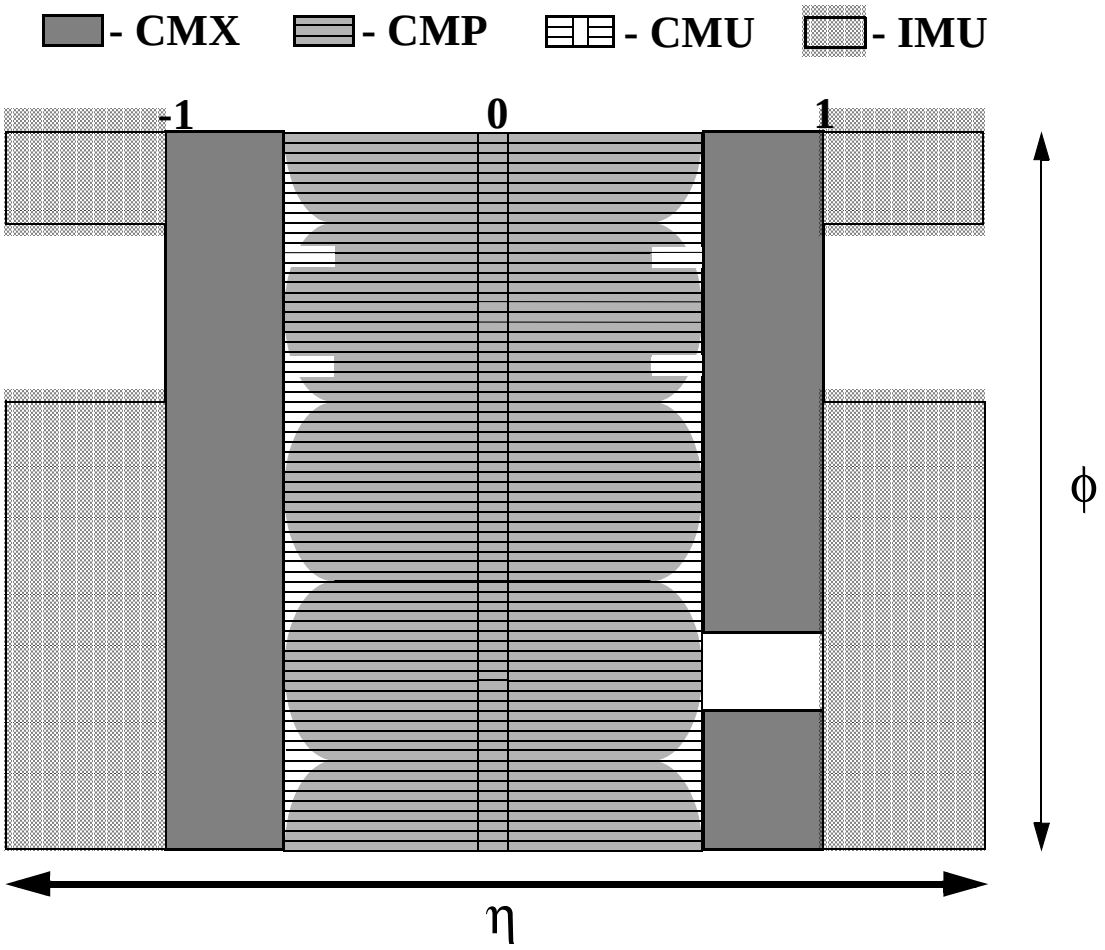

Figure 2.4: η and ϕ coverage of the Run II muon systems

of rectangular scintillator tiles.

Another upgrade which was begun in Run I is the **Central Muon Extension** (CMX) with the associated **Central Scintillator Extension** (CSX). It is a conical array of drift tubes, with scintillators on both sides; it extends the CMU/CMP θ coverage from 55° to 42°, except in a 30° ϕ gap which is used by the solenoid cryogenic system.

2.6.2 Intermediate muon detectors

Detection of muons in the forward region is accomplished by the **Intermediate Muon Detectors** (IMU). This detector recycles the older Forward Muon toroidal magnets, which is moved closer to the interaction point (just outside the plug calorimeter PMT arrays). The steel toroids, together with a new pair of steel rings, act as shielding for a new array of drift tubes and scintillator counters, placed on the outer radius of the toroids.

Like the CMX/CSX, the IMU has four staggered layers of drift tubes, and two layers of scintillator. Contrarily to the CSX, one of the scintillator layers is separated from the drift tubes by a thick layer of steel; this geometry strongly suppresses fake triggers due to hadrons.

2.7 Data Acquisition and Trigger

Due to the increase in collision frequency, the DAQ and trigger systems of CDF had to be almost completely replaced. The new three-level architecture, schematized in figure 2.5, is fully capable of withstanding a 132 ns bunch separation, while keeping dead time as short as possible.

2.7.1 Level 1 trigger

The front-end electronics of all detectors is fitted with a synchronous pipeline, 42 events deep, where the entire data regarding each event is stored for 5544 ns. Meanwhile, part of the data is examined in a first layer of dedicated, synchronous, highly parallel hardware processors:

- **XFT**, the eXtremely Fast Tracker, which reconstructs tracks on the transverse plane of the COT to propagate these tracks to the calorimeters and muon chambers;
- the Calorimeter Trigger, which detects electron and photon candidates, jets, total transverse energy, and missing transverse energy;
- the Muon Trigger, which matches XTRP tracks to stubs in the muon chambers.

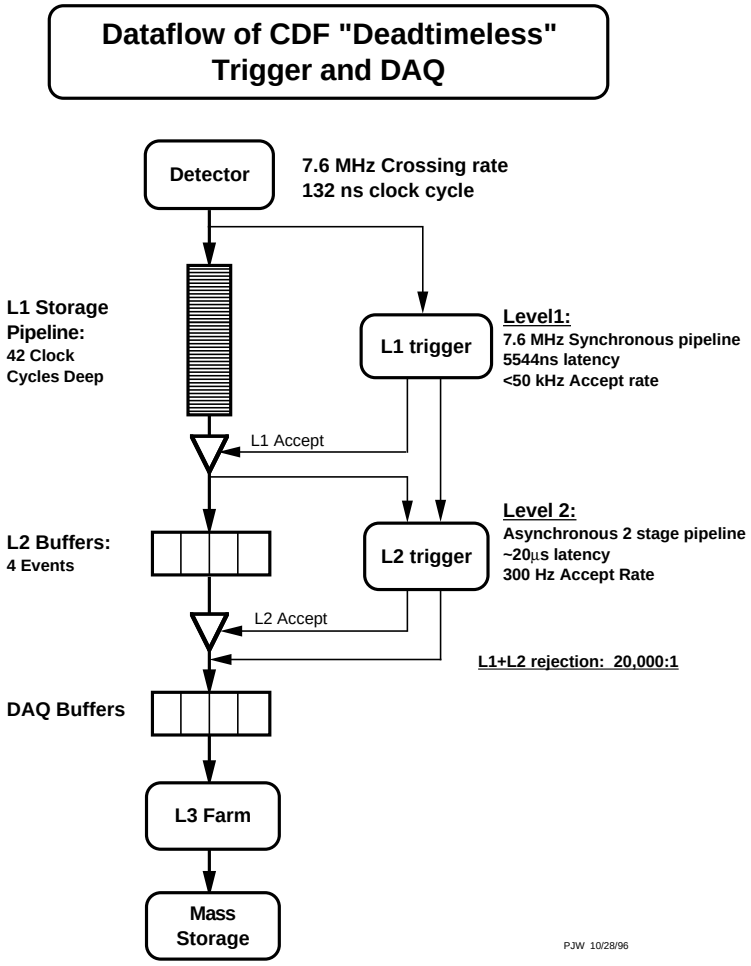

Figure 2.5: Block diagram of the CDF II Trigger

"Objects" from the level one trigger subsystems are combined in a flexible decision module, which takes a decision by requiring the presence of a certain number of features in the event: for example, two muon candidates with P_t above 3 GeV. Up to 64 different sets of requirements can be checked at the same time; each of these triggers can be prescaled independently of the others.

The level 1 trigger takes a decision within 4 μs, while the event's data is still in the pipeline. This makes the first trigger level truly deadtimeless. The rejection factor is about 150 and the event rate is about 50 kHz.

2.7.2 Level 2 trigger

Events matching the requirements of level 1 are downloaded into one of four asynchronous event buffers, and further analyzed by a second set of hardware processors. Trigger level 2 is asynchronous: events remain in the buffer until they are accepted or rejected. This can cause dead time, when all four buffers are full. In order to keep dead time at 10%, with a level 1 rate of 50 kHz, level 2 has been split in two pipelined steps of 10 μs each.

- Jets usually affect more than a single calorimetric tower. Calorimeter clustering (**L2CAL**) sums the energies collected by single towers and provides a measurement of the total jet energy.
- The calorimeter shower maximum (**XCES**) is used to reduce the rate of fake electrons and photons. It also makes it easier to match XFT tracks to their calorimetric clusters.
- The Silicon Vertex Tracker (**SVT**) reconstructs tracks in the vertex detector, measuring their impact parameter d. Triggering on d proves extremely helpful in b-quark physics.
- Data is also collected from the level 1 track and muon triggers.

During the second pipelined step, the results of the first phase are fed to a set of Alpha processors; each processor examines the event for a different set of characteristics.

The level 2 accept rate is around 300 Hz, with a rejection of about 150.

2.7.3 Level 3 trigger

After being accepted by the level 2 trigger, the entire event data is read out and loaded into a Linux PC farm, where the event is fully reconstructed in software. The level 3 reconstruction program is almost fully written in C++, using object–oriented techniques.

After an event is reconstructed, it is sent to an event counter, where its characteristics are histogrammed; if the event passes the level 3 cuts, it is also permanently stored to tape.

Assuming a level 3 input rate of 300 Hz, a level 3 rejection of 10, and an average event size of 250 kB.

2.7.4 Online Monitoring

The CDF detector consists of many detector subsystems and runs in a high rate large bandwidth data transfer environment. To take data with high efficiency and high quality, it is necessary to quickly spot problems with one of these subdetectors in real time. Multiple event monitor programs are attached to the DAQ system [39][40][41]. The online monitoring programs are called Consumers, where a consumer is defined as a process which receives events from Consumer Server Logger (CSL) in real time. CSL sends the data to the computer center where they are written to tape and forwards copies of a subset of the data to the online monitoring programs. Figure 2.6 shows a schematic view of the CDF online monitoring system (Consumer Framework). The task of Consumers is to analyze and monitor the event data and to make histograms and tables. These results could be viewed by the display browser via a server in real time. Results of the monitor are also stored as data files periodically during a run, and also archived systematically. The display browser provides a GUI to view the online monitored results, while also providing some basic utilities to do comparisons with previously stored results. By separating the two tasks of monitoring and displaying, we remove CPU bound associated with displaying graphics from the machine which runs the consumers. During the data taking, multiple consumer processes run in parallel, receiving event data with the desired trigger types from the CSL. Communication between a consumer and run control which control overall CDF DAQ system is handled by the Error Receiver. Severe errors detected by a consumer monitor program are forwarded to run control to take necessary actions. The state manager watches the state of consumers.

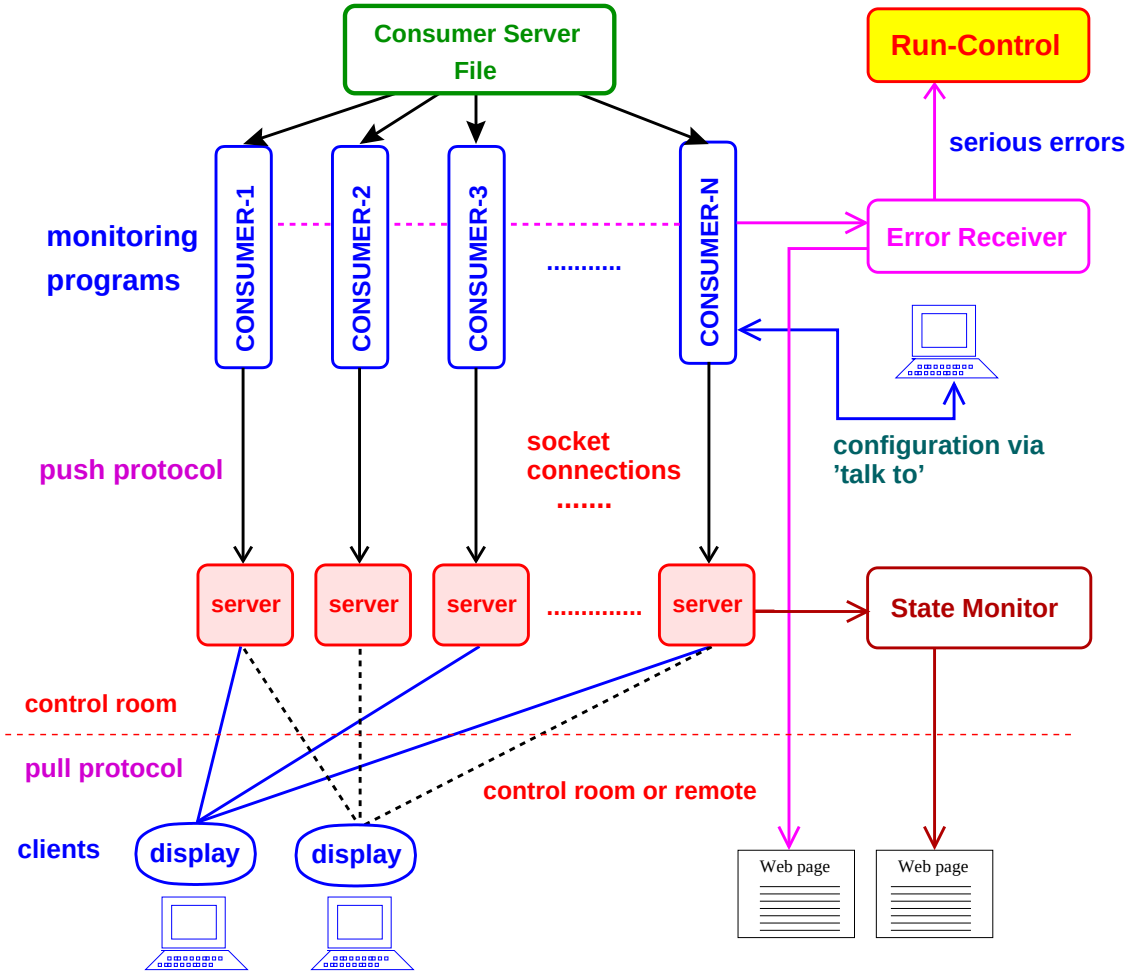

Figure 2.6: Design of the CDF online consumer framework.

Chapter 3

Event selection

The data used for this analysis were collected with the upgraded Collider Detector at Fermilab (CDF II) at the Tevatron $\bar{p}p$ collider, and correspond to an integrated luminosity of approximately 200 pb^{-1} at $\sqrt{s} = 1.96$ TeV , taken during the period March 2002 - September 2003. All data used in this analysis were stripped from a data stream for immediate processing after event reconstructions. In section 3.1, trigger requirement for this analysis is described. Section 3.2 describes electron identification. Section 3.3 describes selection criteria for this analysis and the result of the selection.

3.1 Trigger requirement

We select an initial inclusive data set from a data stream triggered by Electron_Central_18 trigger and Electron_70 trigger. All data used in this analysis were reconstructed with the offline after passing these two triggers. The trigger paths for these two triggers are as following :

- Electron_Central_18 trigger

    1. Level 1 : L1_CEM8_PT8
       CEM tower with $E_T > 8$ GeV and XFT pointing to the tower with $P_T > 8$ GeV are required.
    2. Level 2 : L2_CEM16_PT8
       CEM cluster from the high-E_T clustering with $E_T > 16$ GeV and XFT pointing to the cluster with $P_T > 8$ GeV are required. A E_{had}/E_{em} cut of 0.125 is required.

3. Level 3 : L3_Electron_Central_18

   Offline calorimeter cluster with $E_T > 18$ GeV and COT track pointing to the cluster with $P_T > 9$ GeV are required.

- Electron_70 trigger

1. Level 1 : L1_JET10

   EM+HAD tower with $E_T > 10$ GeV is required.

2. Level 2 : L2_JET90

   Jet cluster with $E_T > 90$ GeV is required.

3. Level 3 : L3_Electron70_Central

   Central electron candidate with $E_T > 70$ GeV and COT track pointing to the cluster with $P_T > 15$ GeV are required.

In Electron_Central_18 trigger, there is a requirement on a ratio of hadronic energy to the electromagnetic energy of the cluster (E_{had}/E_{em}). We have studied the effect of E_{Had}/E_{Em} cut of Electron_Central_18 trigger on an electron under the Run II conditions.

We generated 10000 events of single electron Monte Carlo data sample with $50 < E_T < 450$ GeV (flat distribution) and $-1 < \eta < 1$ (flat distribution). Figure 3.1 shows the generated electron E_T and η distributions.

Figure 3.2(a) shows the Level 2 cluster EM E_T distribution while Figure 3.3(a) shows offline reconstructed EM E_T of generated electrons. The shapes of the generated and offline reconstructed E_T distributions are similar as we expect, however, the level 2 cluster E_T distribution is dramatically different. This is caused by the saturation of level 2 read-out electronics at around 128 GeV in an EM tower. Figure 3.2(b) shows the level 2 HAD E_T distributions for the same event set.

Figure 3.2(c) shows the Level 2 E_{Had}/E_{Em} distribution (ratio of Figure 3.2(a) and Figure 3.2(b)) and Figure 3.2(d) shows the Level 2 E_{Had}/E_{Em} distribution plotted against offline reconstructed E_T. Figure 3.3(b) shows the offline reconstructed E_T distribution of those electrons which passed the Level 2 E_{Had}/E_{Em} cut (<12.5%). Figure 3.3(c) shows the efficiency of this Level 2 E_{Had}/E_{Em} (12.5%) cut (ratio of Figure 3.3(b) and Figure 3.3(a)). This figure shows that the 12.5% Level 2 E_{Had}/E_{Em} stays efficient up to electron E_T around 150 GeV, however the cut contributes to the significantly lower efficiency for very high E_T electrons.

If we require only Electron_Central_18 trigger, then we suffer substantial inefficiency for high mass dielectron search. However, by requiring Electron_70 trigger which has no E_{Had}/E_{Em}

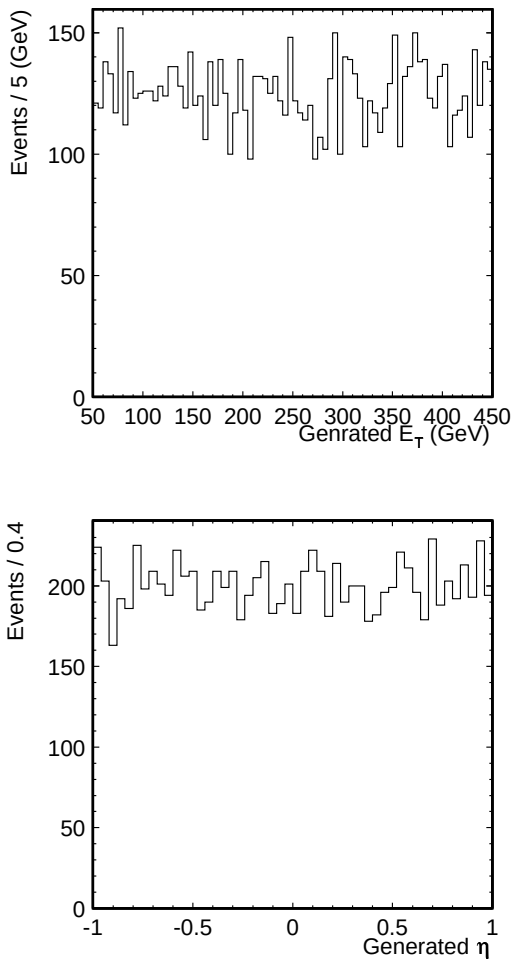

Figure 3.1: Generated electron E_T (a) and η (b) distributions.

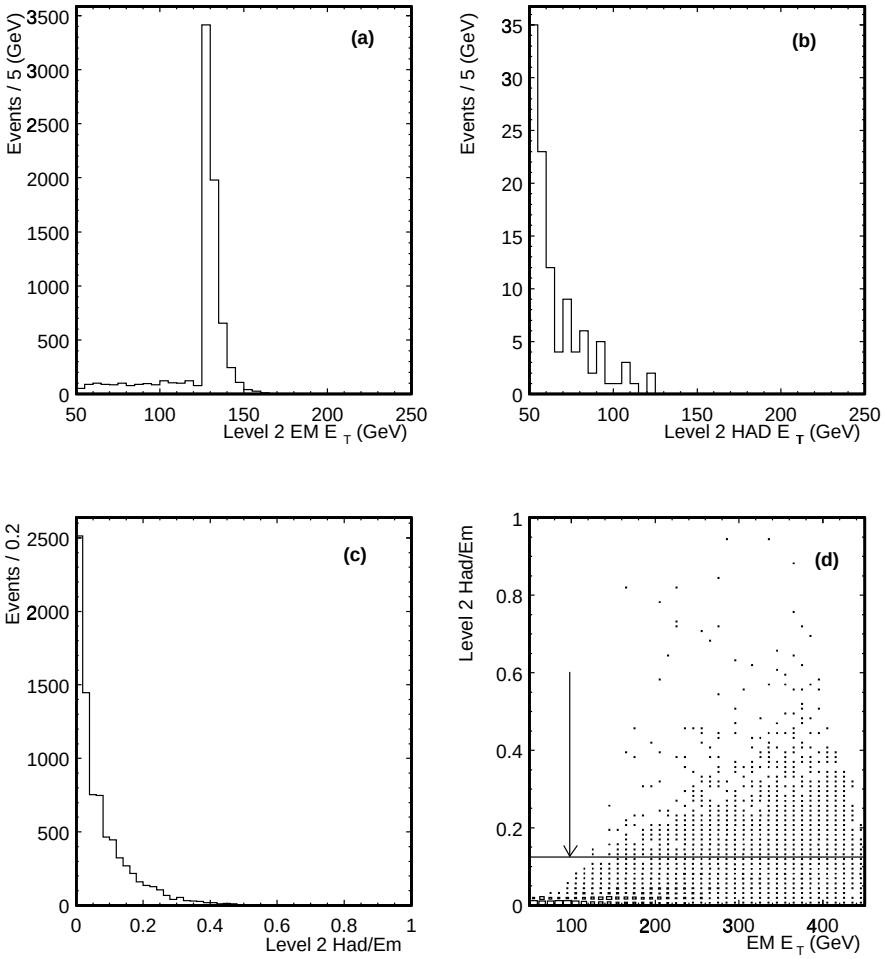

Figure 3.2: (a) Level 2 trigger cluster EM E_T distribution, (b) Level 2 trigger cluster Hadron E_T distribution (c) Level 2 trigger E_{Had}/E_{Em} distribution, (d) Level 2 E_{Had}/E_{Em} vs. reconstructed electron E_T.

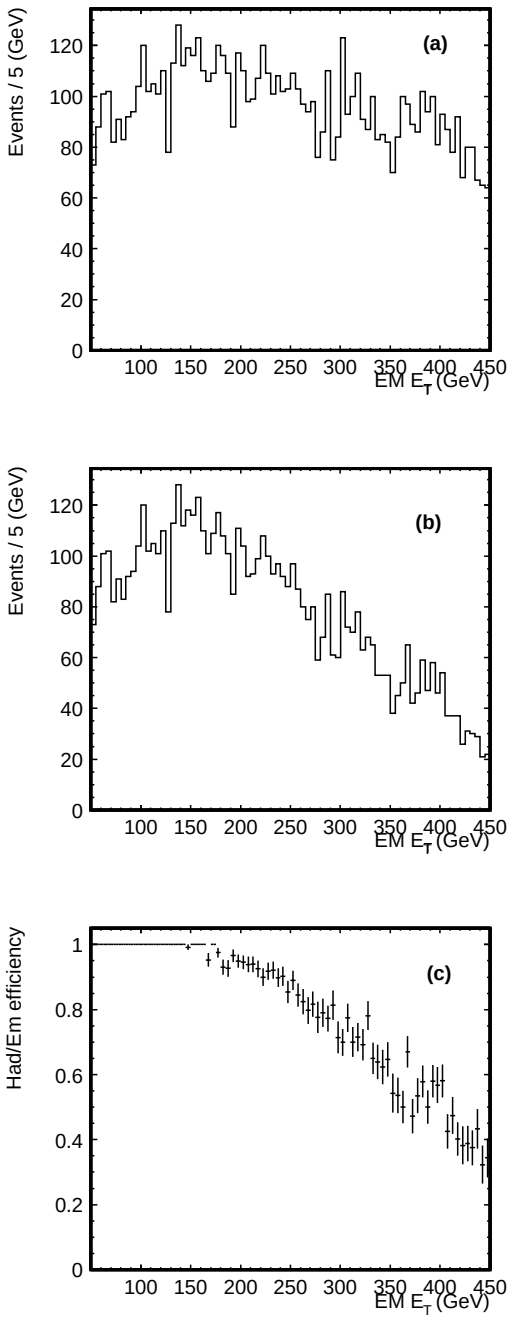

Figure 3.3: (a) reconstructed electron E_T distribution, (b) reconstructed electron E_T of events passing the cut $E_{Had}/E_{Em} < 0.125$ and (c) Level 2 E_{Had}/E_{Em} efficiency as a function of electron E_T.

requirement, electron detection becomes efficient for high E_T. Front-end electronics of calorimeter has a full scale input charge of 1300 pC, this corresponds to $\sim$ 800 GeV. For the offline reconstruction, there is no saturation until about 800 GeV.

We have studied efficiencies of the Electron_Central_18 trigger and Electron_70 trigger for high E_T electrons by selecting $W \rightarrow e\nu$ with electron E_T above 70 GeV. To estimate Electron_Central_18 trigger efficiency, we start $W \rightarrow e\nu$ sample with Electron_70 trigger and to estimate Electron_70 trigger efficiency, we start $W \rightarrow e\nu$ sample with Electron_Central_18 trigger. Figure 3.4 shows electron E_T distributions of $W \rightarrow e\nu$ samples with electron E_T above 70 GeV from Electron_Central_18 trigger and Electron_70 trigger and E_T dependence of trigger efficiencies of Electron_Central_18 and Electron_70 triggers. This figure shows that Electron_Central_18 trigger efficiency stays efficient up to E_T around 150 GeV, however efficiency decreases for very high E_T in agreement with Monte Carlo study.

3.2 Electron Identification

An electron will shower in the electromagnetic calorimeter. The shower is narrow and has well-defined shape both longitudinally and transversely. A track has to point to the shower; the momentum of the track (p) has to match the energy of the shower (E), $E/p \sim 1$. A ratio of the hadronic energy (E_{had}) to the electromagnetic energy (E_{em}) is small, $E_{had}/E_{em} \ll 1$. Figure 3.5 shows the behavior of particles in CDF detector.

3.2.1 Central Electron Parameters

- E_T : Electron Transverse Energy
  The electron E_T is defined as $E \times \sin\theta$ where E is the energy of the electromagnetic cluster. θ is calculated for the beam constrained track. The cluster energy is the sum of the electromagnetic energies of a CEM seed tower and a number of shoulder EM towers.

- P_T : Beam Constrained Track Momentum
  The highest P_T COT track which extrapolates to the cluster is considered to be associated with the cluster. The track is adjusted according to a beam constraint, which improves the track resolution by including the beam spot as additional information.

- ΔX and ΔZ : Track-shower matching variables
  The COT track pointing to an electron cluster is extrapolated to the CES. The variable

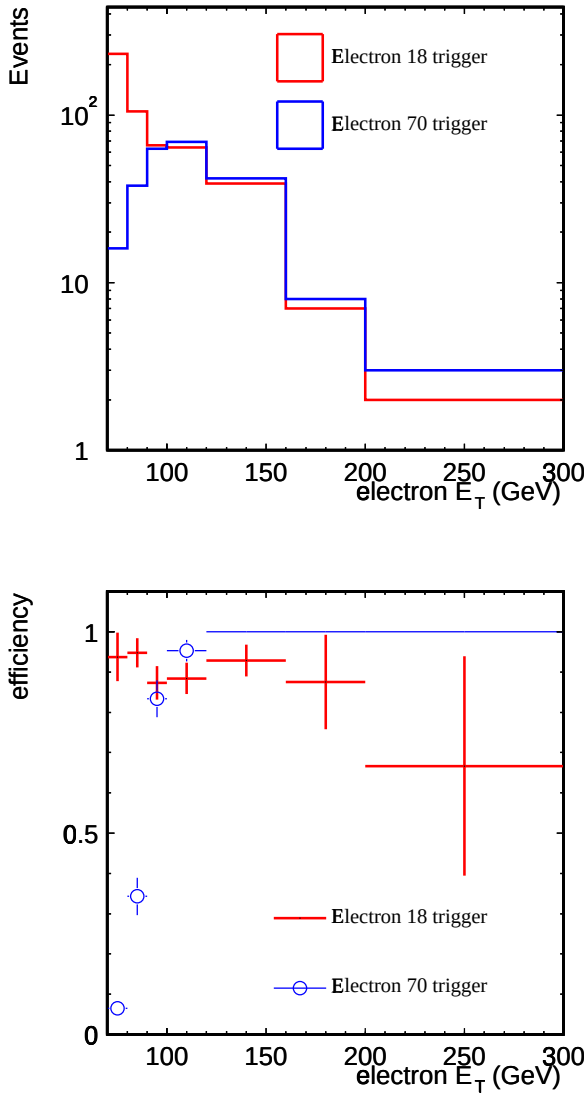

Figure 3.4: Electron E_T distributions of $W \to e\nu$ samples with electron E_T above 70 GeV from Electron_Central_18 trigger and Electron_70 trigger (top). E_T dependence of trigger efficiencies (bottom).

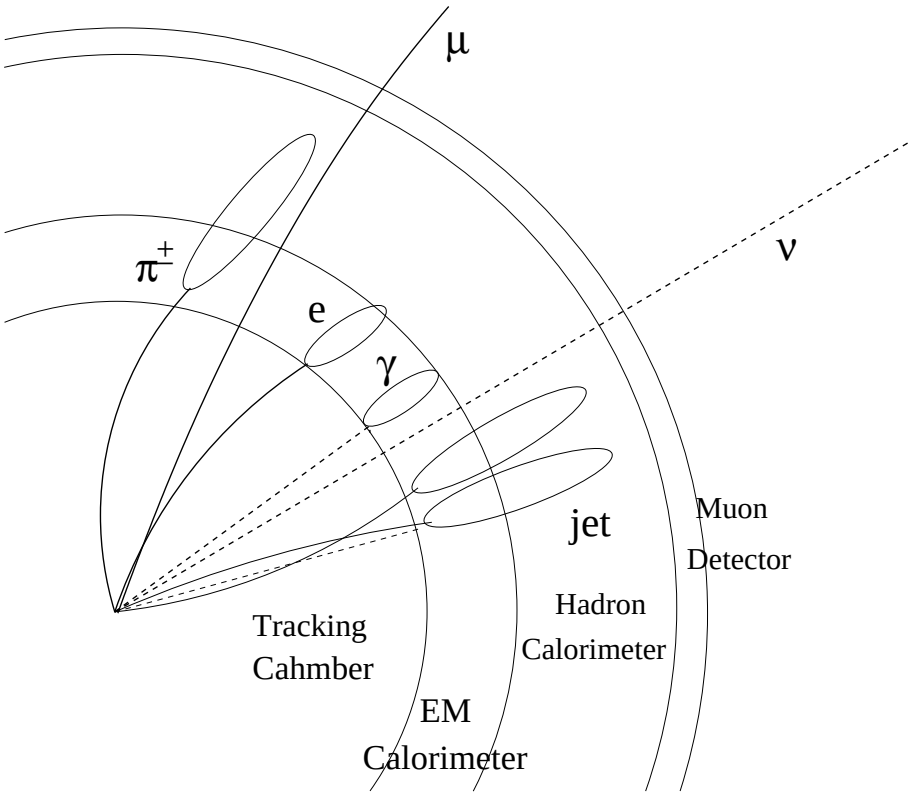

Figure 3.5: Particles identification and CDF detector.

ΔX is the separation in the $r-\phi$ view between the extrapolated track position and the CES strip cluster position. The variable ΔZ is the corresponding separation in the z view. ΔX and ΔZ are defined as

$$\Delta X = X_{track} - X_{CES}, \tag{3.1}$$

$$\Delta Z = Z_{track} - Z_{CES}. \tag{3.2}$$

- *Isolation* : Electron isolation variable in the calorimeter
  The electron isolation in the calorimeter is defined as

$$Isolation = \frac{E_T^{cone} - E_T^{cluster}}{E_T^{cluster}} \tag{3.3}$$

  where E_T^{cone} is the sum of the electromagnetic and hadronic transverse energies measured in all of the towers in a radius of $R = \sqrt{\Delta\phi^2 + \Delta\eta^2} = 0.4$ around the electron. $E_T^{cluster}$ is the transverse electromagnetic energy of the electron.

- E_{had}/E_{em}
  The ratio of the hadronic energy to the electromagnetic energy in all towers included in the cluster.

- E/P
  The ratio of the electron energy to the momentum of the highest P_T COT track pointing to the cluster.

- L_{shr}
  Transverse profile of an electron that allows a comparison of the lateral sharing of energy in the calorimeter towers of an electron cluster to electron shower shapes from the test beam data. L_{shr} is defined as

$$L_{shr} = 0.14 \sum_i \frac{E_i^{adj} - E_i^{prob}}{\sqrt{0.14^2 E + (\Delta E_i^{prob})^2}} \tag{3.4}$$

  where E_i^{adj} is the measured energy in a tower adjacent to the seed tower, E_i^{prob} is the expected energy in the adjacent tower, $0.14^2 E$ is the error on the energy measurement, and ΔE_i^{prob} is the error on the energy estimate. E_i^{prob} is calculated using a parameterization from test beam data.

- Fiducial volume

  A fiducial region is defined so as to avoid inactive detector region. The determination of fiducial region is made in the CES local coordinate by requiring

$$-21 \text{ cm} \leq X_{CES} \leq 21 \text{ cm}, \tag{3.5}$$

$$9 \text{ cm} \leq Z_{CES} \leq 230 \text{ cm}. \tag{3.6}$$

3.2.2 Plug Electron Parameters

Since the COT track does not cover the entire plug region, track requirements (E/P, ΔX and ΔZ) are not imposed for the plug electron candidates. $Isolation$ and E_{had}/E_{em} are imposed for the plug electron candidates.

- $Isolation$

  The electron isolation in the calorimeter is defined as

$$Isolation = \frac{E_T^{cone} - E_T^{cluster}}{E_T^{cluster}} \tag{3.7}$$

  Definitions of E_T^{cone} and $E_T^{cluster}$ are same as for central electron.

- E_{had}/E_{em}

  The ratio of the hadronic energy to the electromagnetic energy in all towers included in the cluster.

- $\chi^2_{3\times3}$

  A χ^2 obtained by comparing observed lateral shower shape with the predicted shape from test beam electrons. The shape comparison is performed in the 3 towers in η by the 3 towers in ϕ around the electron cluster's center.

- Fiducial volume

  The determination of fiducial region in the plug calorimeter is made in the PES detector η.

3.3 Selection Criteria for the Analysis

The requirements on the central electrons are shown in Table 3.1. The loose cuts is the same set of the tight cuts except for the isolation cuts. The requirements on the plug electrons are shown

in Table 3.2. Figure 3.6 shows the distributions of central electron variables and plug electron variables for electrons and QCD fake events.

To eliminate background from $W+$ jets events, a missing E_T significance (S) is required less than 2.5. S is defined as

$$S = \frac{\not\!\!E_T}{\sqrt{\sum E_T^i}} \tag{3.8}$$

where $\sum E_T^i$ is a scalar sum of the transverse energy of the over all calorimeter towers. The missing E_T ($\not\!\!E_T$) is defined as

$$\not\!\!E_T = \left|(-1) \times \sum \vec{E}_T\right| \tag{3.9}$$

where $\vec{E}_T$ is a two-dimensional vector whose magnitude is the transverse energy in a calorimeter tower and whose direction points in the transverse plane from the event vertex to the center of the calorimeter tower. Figure 3.7 shows the S distributions of the W + jet events. Figure 3.8 shows the S distributions of the Z events with the requirements of the dielectron invariant mass between 70 GeV/c^2 and 110 GeV/c^2.

We also require the event vertex z_0 of each event to be within 60 cm of the center of the detector. z_0 is the z coordinate of the COT track associate with the electron.

We classify event types into two categories. Figure 3.9 shows one event type. In this category, two electrons are detected by the central electromagnetic calorimeter and we call this type of events as "Central-Central" events. Figure 3.10 shows the other type of events. In this category, one electron is detected by the central electromagnetic calorimeter and the other electron is detected by the Plug electromagnetic calorimeter. We call this type of events as "Central-Plug" events.

The dielectron invariant mass distributions for events passing these selection criteria are shown in Figure 3.11 for the Central-Central combination and in Figure 3.12 for the Central-Plug combination. Electron energy scale is determined so that the dielectron invariant mass peaks at $\sim$ 91 GeV (scaling up CEM energy by 1% and scaling up PEM energy by 5%). The sample contains 12439 events. There are 4852 Central-Central events and 7587 Central-Plug events. Figure 3.13 shows event pictures of a typical high mass event.

Variable	**Tight Cuts**	**Loose Cuts**
Iso	< 0.1	< 0.2
E_T	> 25 GeV	
P_T	> 15 GeV	
E_{had}/E_{em}	$< 0.055 + 0.00045 \times E$	
E/P	< 4 (for $E_T < 100$ GeV)	
$\|\Delta X\|$	< 3 cm	
$\|\Delta Z\|$	< 5 cm	
L_{shr}	< 0.2	
Fiducial cut	FIDELE $= 1$	

Table 3.1: Central electron selection requirements.

Variable	**Cuts**
E_T	> 25 GeV
Iso	< 0.1
E_{had}/E_{em}	$< 0.055 + 0.00045 \times E$
$\chi^2_{3\times3}$	< 10
Fiducial cut	$1 < \|\eta\| < 3$

Table 3.2: Plug electron selection requirements.

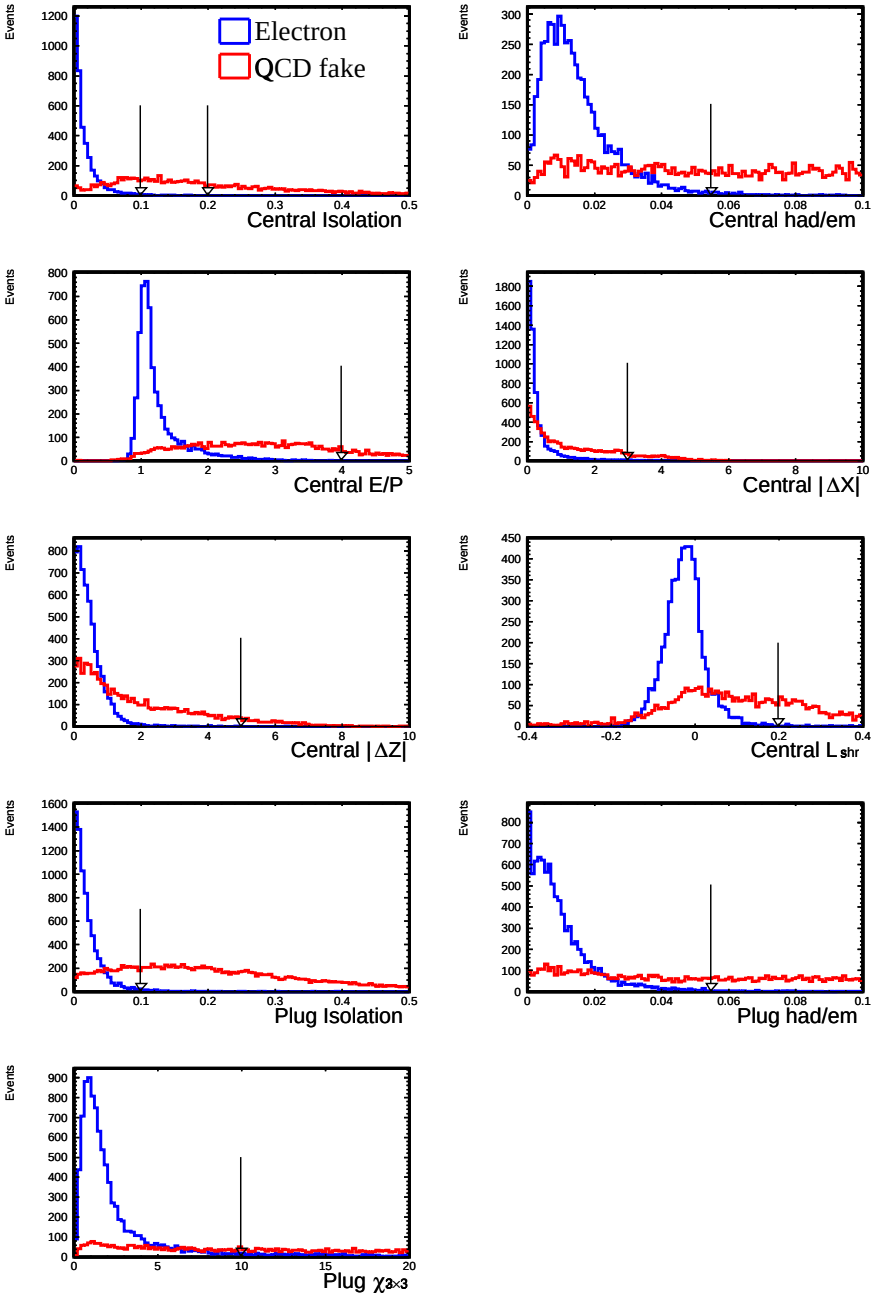

Figure 3.6: Distributions of central electron variables and plug electron variables. The arrows indicate the cut thresholds (for the E_{had}/E_{em}, minimum cut threshold).

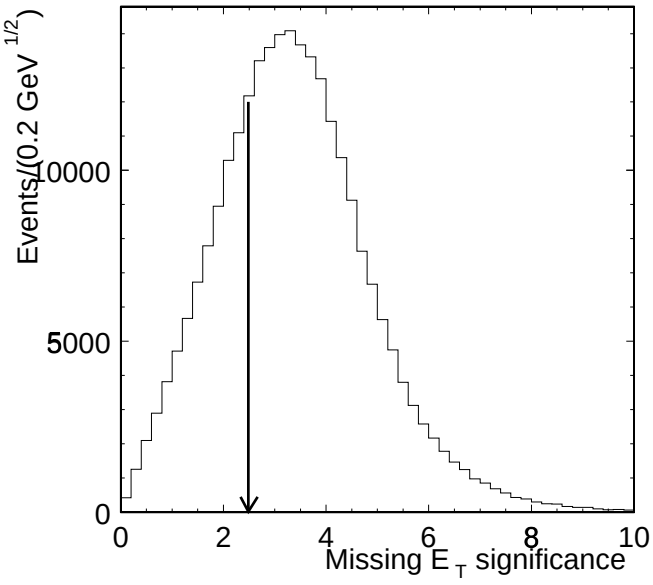

Figure 3.7: The $\not\!\!E_T$ significance distribution of W + jet sample. The Arrow indicates cut value we apply.

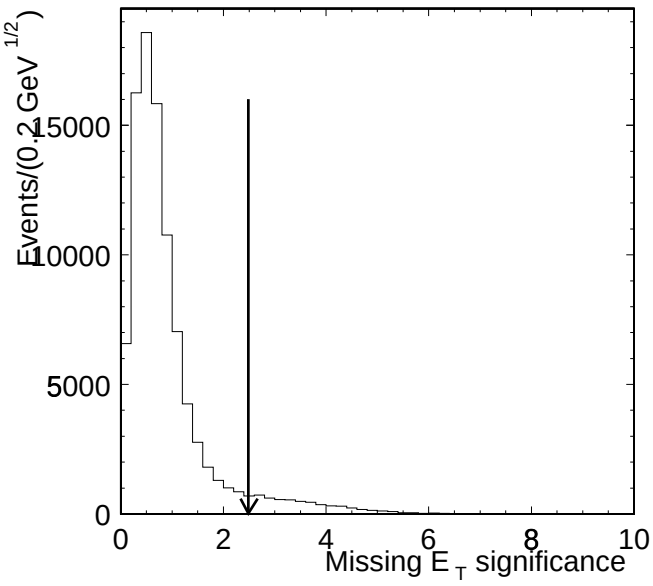

Figure 3.8: The $\not\!\!E_T$ significance distribution of $Z \to e^+e^-$ sample. The Arrow indicates cut value we apply.

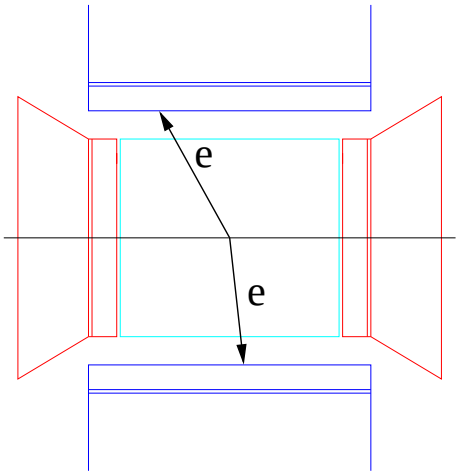

Figure 3.9: Two electrons are detected by the central electromagnetic calorimeter. We call this type of events as "Central-Central" events.

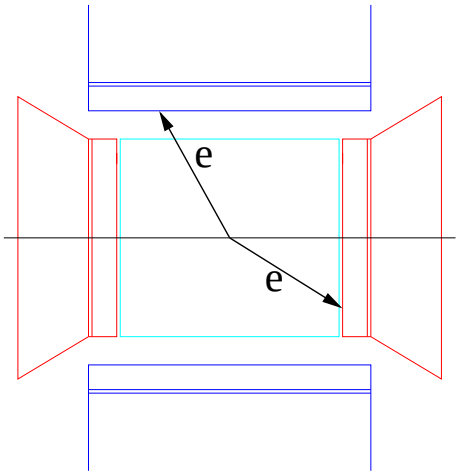

Figure 3.10: One electron is detected by the central electromagnetic calorimeter and the other electron is detected by the Plug electromagnetic calorimeter. We call this type of events as "Central-Plug" events.

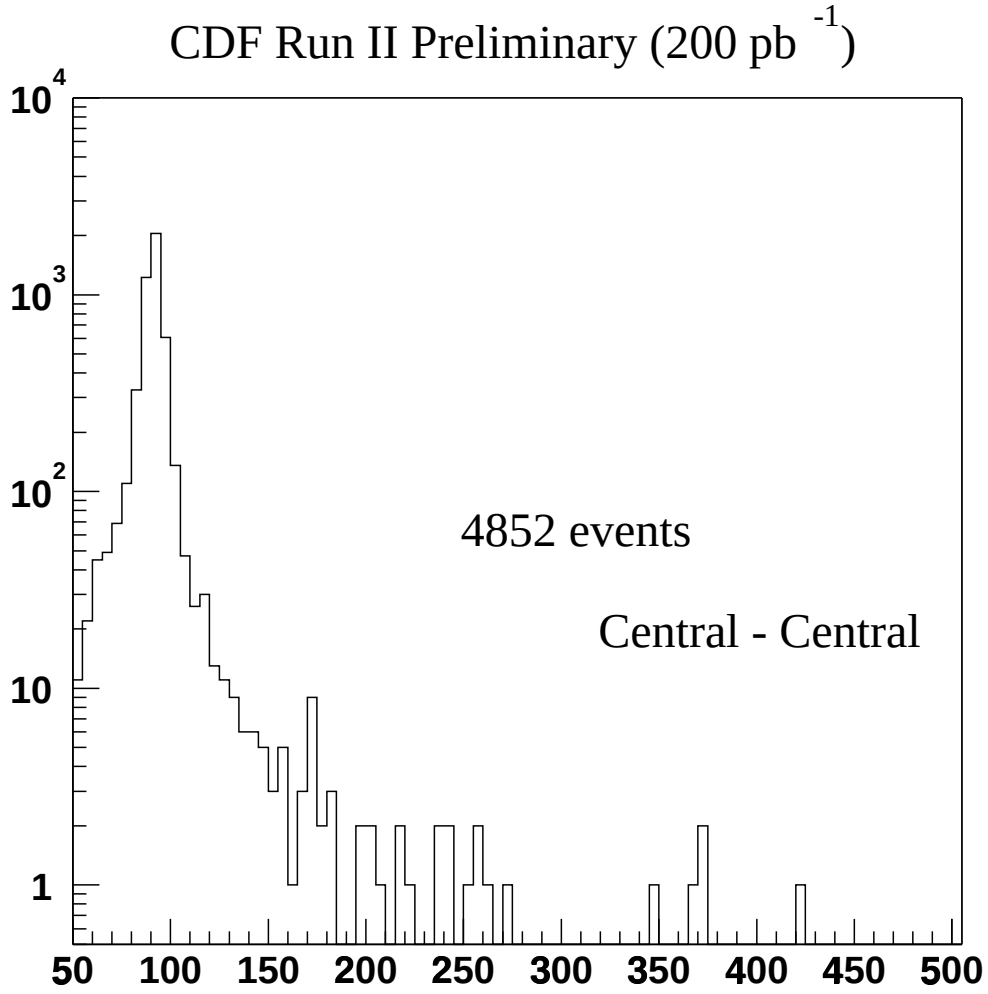

Figure 3.11: Invariant mass distributions for the Central-Central category of the dielectron sample. The plot is shown with a log scale.

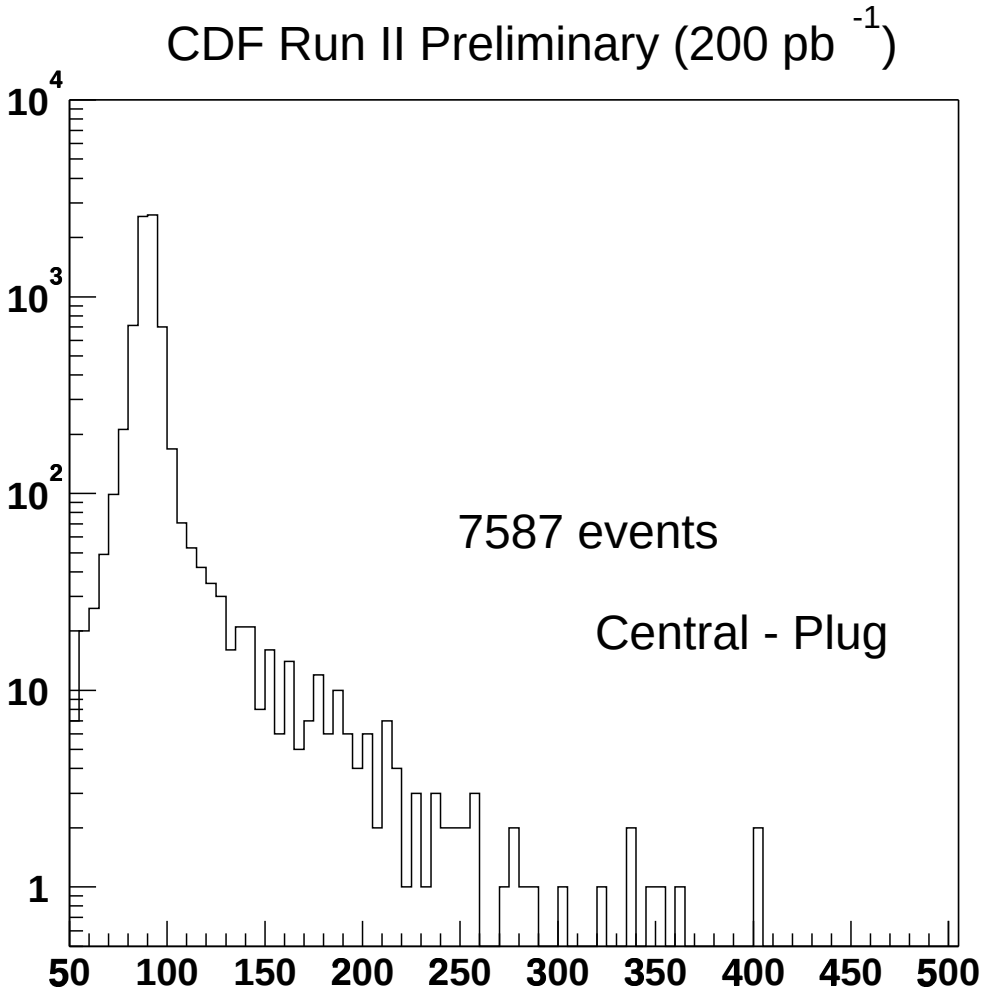

Figure 3.12: Invariant mass distributions for the Central-Plug category of the dielectron sample. The plot is shown a log scale.

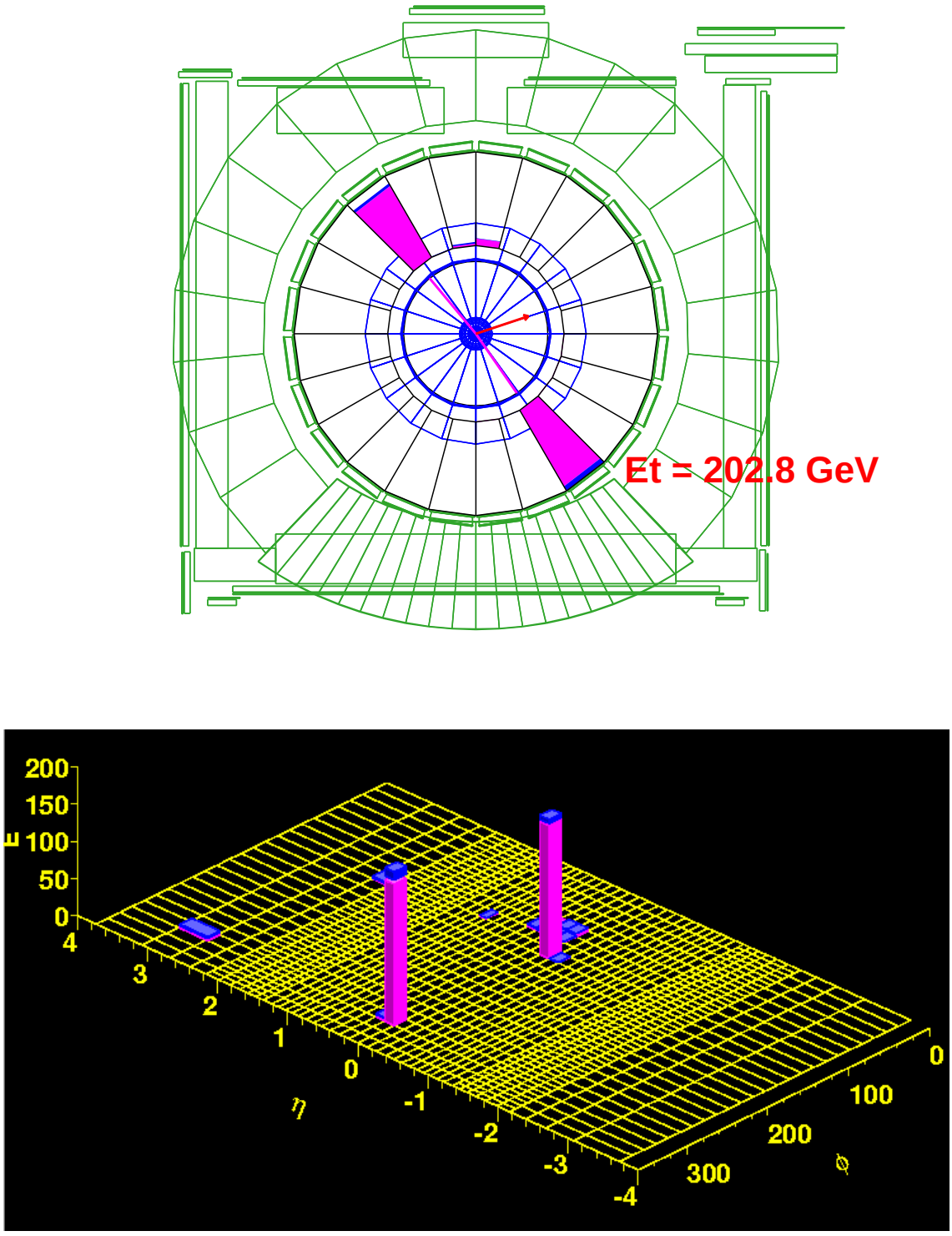

Figure 3.13: Event pictures of a typical high mass event.

Chapter 4

Background estimation

The background sources of new physics signal in high mass can be classified into three categories.

- Drell-Yan events
- QCD fake events
- Electroweak dielectron events other than Drell-Yan
    1. $Z \to \tau^+\tau^-$
    2. WW, WZ
    3. $t\bar{t}$

The major background in the high mass region where we are looking for new physics is expected to be the Drell-Yan events. The major source of backgrounds other than Drell-Yan production are QCD dijet events with misidentified electrons.

4.1 Drell-Yan Background

The expected numbers of dielectron events from the Drell-Yan production are estimated with the Monte Carlo simulation. $402,000$ events of $\gamma^*/Z \to e^+e^-$ Monte Carlo sample are generated with PYTHIA 6.203 with CTEQ5L parton distribution function. The generated events are simulated and reconstructed with the offline.

	σ (pb)	Events generated	Expected # of events	
			C - C	C - P
$Z \to \tau\tau$	250 (NNLO)	492K	2.9	4.8
WW	13.25 [45]	10K	0.6	0.8
WZ	1.98 [45]	10K	0.7	0.8
$t\bar{t}$	6.7 (NLO) [46]	390K	0.7	0.6

Table 4.1: The number of events expected for 200pb^{-1} in each category.

4.2 Dielectron Background other than Drell-Yan

Electroweak dielectron events, $Z \to \tau^+\tau^-$, WW, WZ and $t\bar{t}$, are estimated with the Monte Carlo simulation. 492,000 events of $Z \to \tau^+\tau^-$, 10,000 events of WW and 10,000 events of WZ are generated with PYTHIA 6.203 with CTEQ5L. 390,000 events of $t\bar{t}$ are generated with HERWIG 6.4 with CTEQ5L. The generated events are simulated and reconstructed with the offline.

Expected number of electroweak dielectron events other than Drell-Yan events are estimated by cross sections, branching ratios and acceptances for each category. Table 4.1 shows expected number of events for 200pb^{-1}. Figure 4.1 shows invariant mass distributions for dielectron events from $Z \to \tau^+\tau^-$, WW, WZ and $t\bar{t}$. Figure 4.2 shows total Electroweak background mass distributions for Central-Central and Central-Plug after normalization to expected number of events.

4.3 Fake electron events

In order to keep high efficiency for high mass dielectron events, our electron selection criteria is loose. More events with QCD fake are expected. Since a jet event will be expected to be produced in association with other particles, the isolation of the jet event is higher than ones of the high mass Drell-Yan events. Electrons from high mass Drell-Yan production are expected to be isolated. Hence, we assume that most events which have high isolation are jet events.

The isolation cut is used to estimate the number of QCD dijet events. Figure 4.3 shows first electron *Isolation* vs. second electron *Isolation* for our dielectron sample with only the isolation cut released. We refer to the signal region as region A. In this study, there are two assumptions listed below :

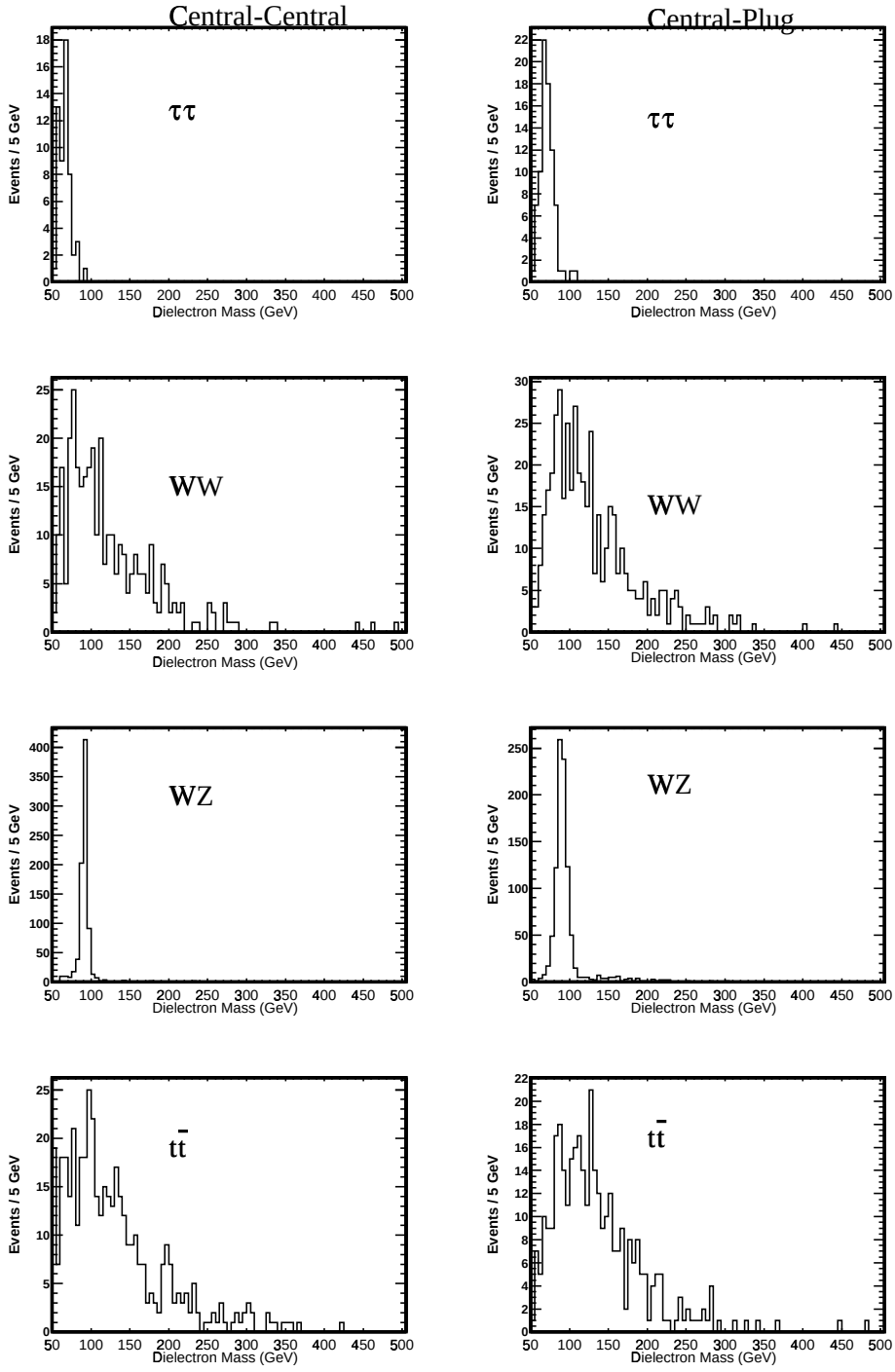

Figure 4.1: Invariant mass distributions for dielectron events from $Z \to \tau^+\tau^-$, WW, WZ and $t\bar{t}$.

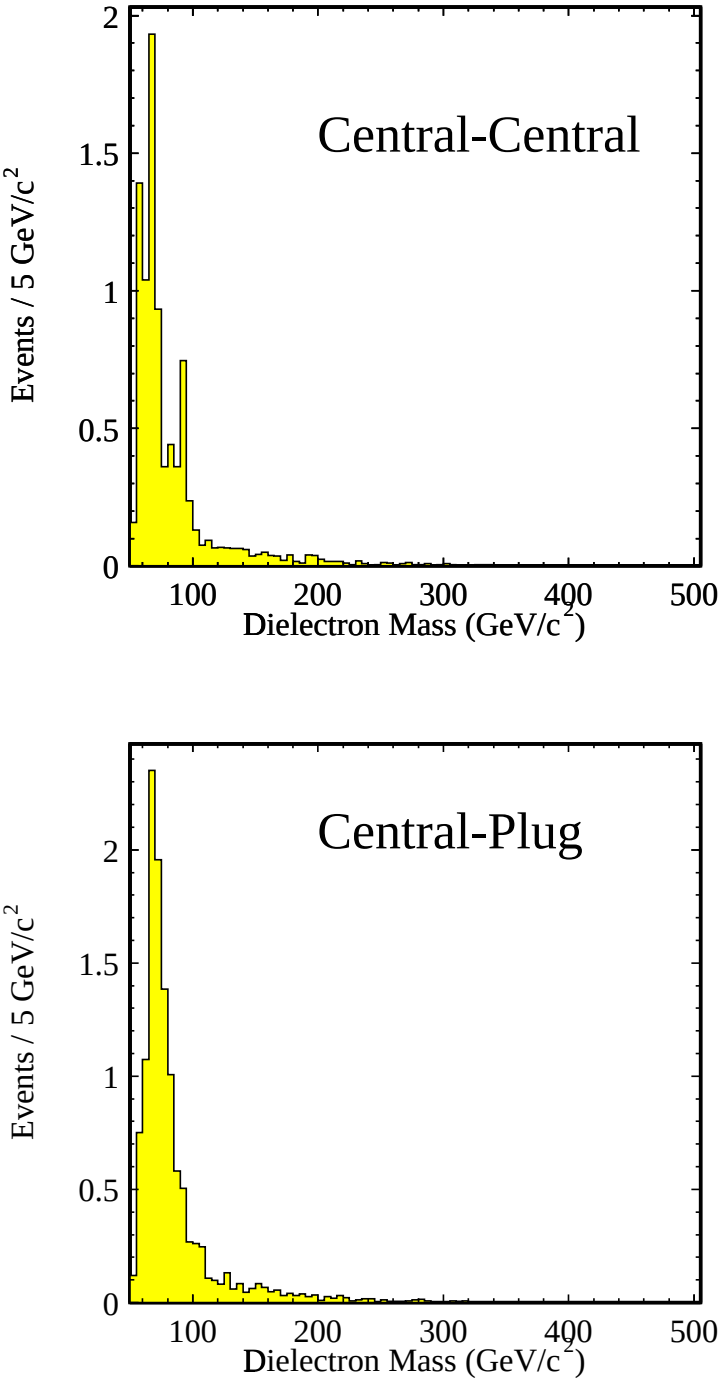

Figure 4.2: Total invariant mass distributions for dielectron events from $Z \to \tau^+\tau^-$, WW, WZ and $t\bar{t}$.

- There is no correlation between two $Isolation$s.
- Signal events are only in region A and all events in other regions are background events.

Only QCD events fall in Region B, C and D. If we assume that the ratio of A to B equals to the ratio of C to D for QCD events, we can determine how many QCD events are region A. The number of events in each region of Central-Central and Central-Plug categories are shown in Table 4.2 for Central-Central events and Table 4.3 for Central-Plug events. From this estimation, we get $195 \pm 132.2(stat.) \pm 82.5(sys.)$ QCD background events in the Central-Central and $402.5 \pm 141.1(stat.) \pm 212.2(sys.)$ events in the Central-Plug categories. The systematic errors are estimated by changing the box on the Figure 4.3.

As a cross check, we also estimate the number of QCD background events with the same-sign events. A charge of the particle is determined with the highest P_T COT track pointing to the calorimeter cluster. The charges of most plug electron candidates cannot be determined by the COT since the COT does not cover most of the plug region. We estimate the number of QCD background events with the same-sign events only for Central-Central category. We assume that the probability of negative charge found in the highest P_T track in a jet is roughly the same one of positive charge. We find 77 same-sign events in the Central-Central events. The number of QCD events are estimated to be 154 ± 24.8 events in the Central-Central sample. The number of estimated background events are consistent with the estimation from the isolation method.

In the high mass region, the number of background events is too small to estimate as a function of dielectron invariant mass. To estimate the number of background events as a function of dielectron invariant mass, we use the QCD dominant invariant mass distributions. The following cuts are required for the events of the QCD dominant sample.

- $Isolation > 0.1$
- $E_{had}/E_{em} > 0.05$

Figure 4.4 shows the QCD background mass distributions for Central-Central and Central-Plug.

4.4 Comparison of Data with Background

Figure 4.5 and Figure 4.6 show the dielectron invariant mass distributions with expected ones from Drell-Yan Monte Carlo events, the QCD background events and the Electroweak background events other than Drell-Yan for Central-Central category and for Central-Plug category,

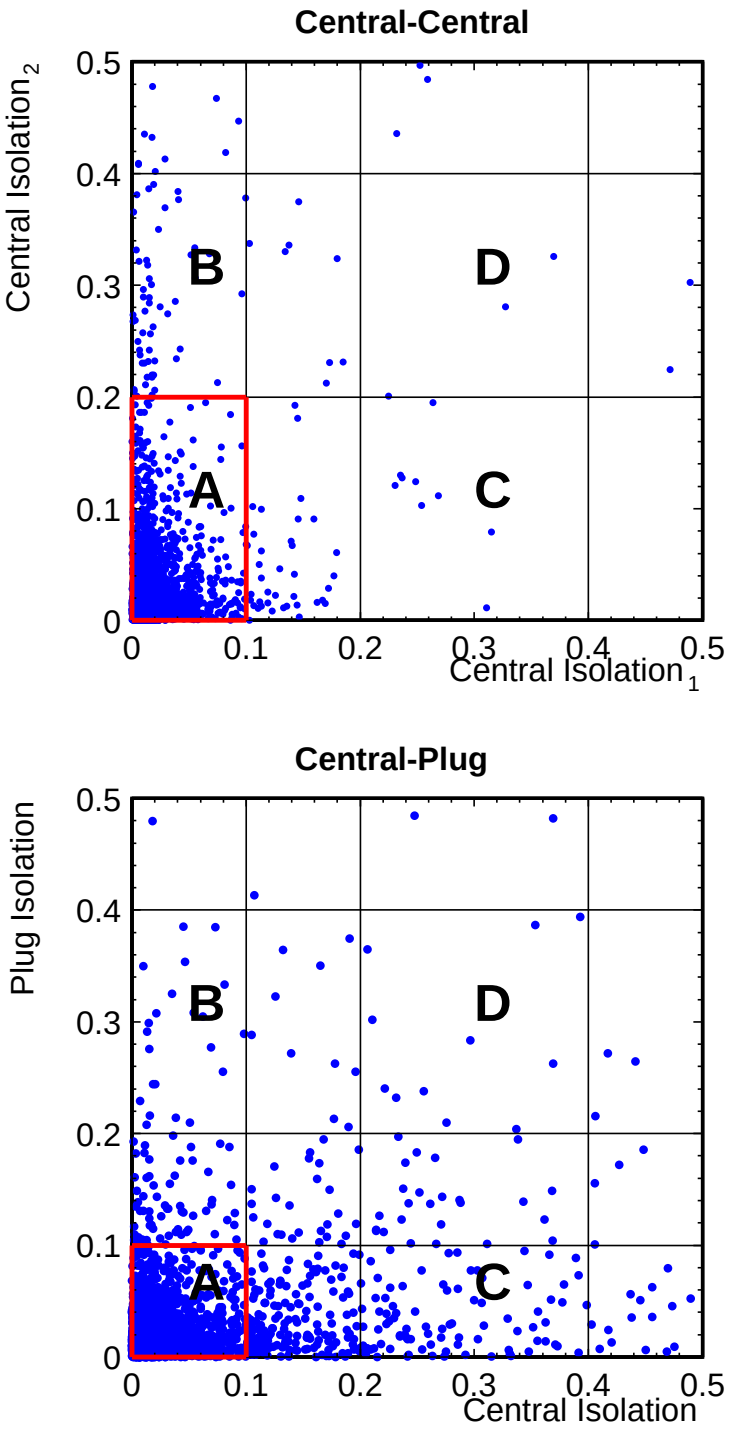

Figure 4.3: Scatter plot of isolation of the first electron (central) and isolation of the second electron (Central-Central for left plot and Central-Plug for right plot).

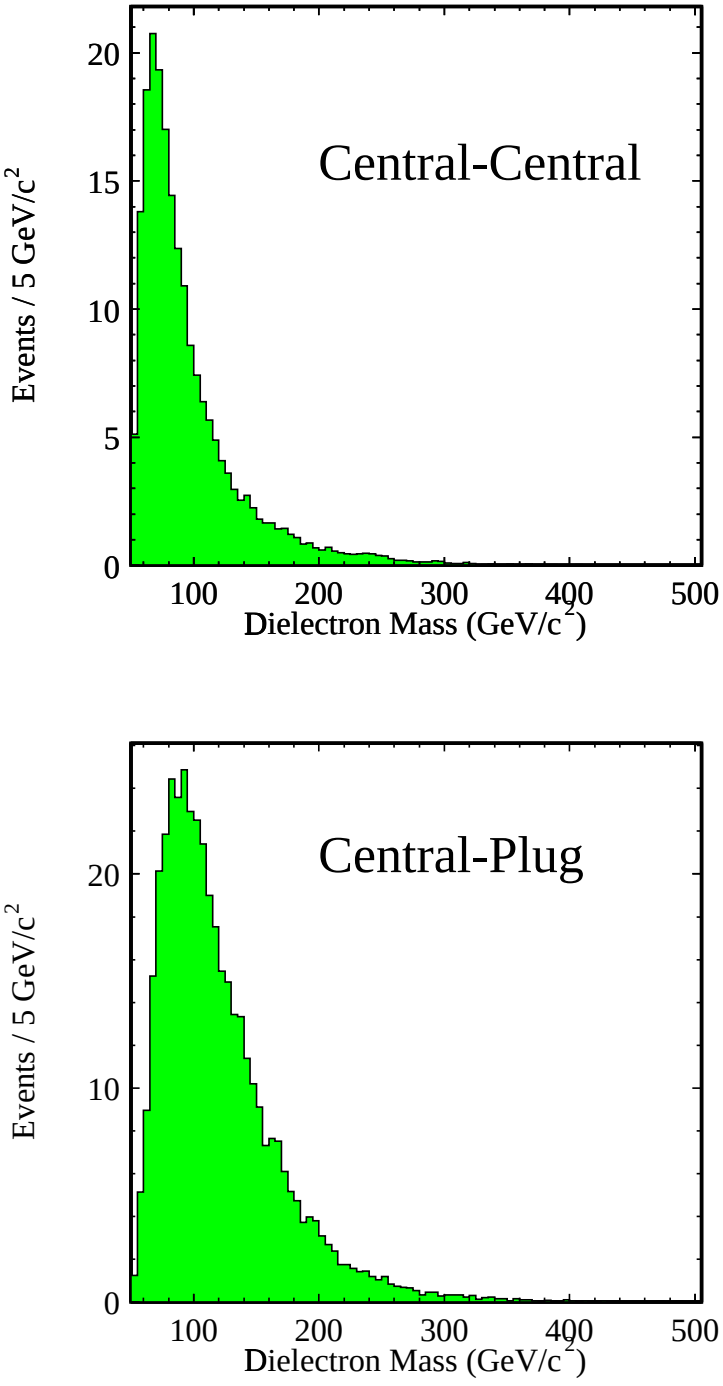

Figure 4.4: QCD background mass distributions for Central-Central and Central-Plug.

	$Iso_1^{central} < 0.1$		$0.2 < Iso_1^{central} < 0.4$	
$Iso_2^{central} < 0.2$	(A)	4813	(C)	9
$0.2 < Iso_2^{central} < 0.4$	(B)	65	(D)	3

Table 4.2: The number of events in each category in the Central-Central events.

	$Iso^{central} < 0.1$		$0.2 < Iso^{central} < 0.4$	
$Iso^{plug} < 0.1$	(A)	7549	(C)	161
$0.2 < Iso^{plug} < 0.4$	(B)	30	(D)	11

Table 4.3: The number of events in each category in the Central-Plug events.

respectively. Figure 4.7 shows the total dielectron invariant mass distributions. QCD background mass distributions in the figures are normalized to the number of events estimated by the isolation method. Electroweak background mass distributions in the figures are normalized to the expected number of events for 200 pb^{-1} described in Table 4.1. The energy corrections for Monte Carlo events are applied by adding extra energy smearing in order to match the resolution seen in data (3% extra smearing for CEM and 1.5% extra smearing for PEM).

The Drell-Yan Monte Carlo histogram is constrained to the number of entries in $70 < M < 110$ GeV/c^2. The normalization factor ($f_{relative}$) is defined as

$$f_{relative} = \frac{Z_{data} - Z_{QCD} - Z_{EWK}}{Z_{DY}} \tag{4.1}$$

where Z_{data} is number of Z events of data, Z_{QCD} is number of QCD background events in Z mass window, Z_{EWK} is number of Electroweak background events in Z mass window and Z_{DY} is number of Drell-Yan Monte Carlo events in Z mass window.

Table 4.4 shows the number of observed events, the expected number from Drell-Yan production, the expected number from QCD background, the expected number from Electroweak background and the sum of Drell-Yan, QCD and EWK background estimation for various mass ranges. Figure 4.8 shows data cumulative distribution function and background cumulative distribution for Central-Central and Central-Plug. Data are in reasonable agreement with background estimations.

Figure 4.9 shows comparison of background estimation with data in $|\cos\theta^*|$ for Central-Central and Central-Plug and Figure 4.10 shows $|\cos\theta^*|$ for total. We define the polar angle θ^* of electrons in the Collins-Soper frame [47]. The polar angle is defined by the following

CDF Run II Preliminary (200 pb^{-1})

Mass (GeV/c^2)	DY		QCD		EWK		DY+QCD+EWK		Data	
	C-C	C-P	C-C	C-P	C-C	C-P	C-C	C-P	C-C	C-P
$M > 200$	13.3	19.1	8.2	29.4	0.2	0.3	21.7	48.8	20	51
$M > 250$	6.5	7.3	2.9	9.8	0.1	0.1	9.5	17.2	10	20
$M > 300$	3.4	3.1	1.0	3.5	0.1	0.0	4.4	6.7	5	9
$M > 350$	1.8	1.4	0.4	1.1	0.0	0.0	2.2	2.4	4	4
$M > 400$	1.0	0.6	0.1	0.3	0.0	0.0	1.1	0.9	1	1
$M > 450$	0.6	0.3	0.0	0.1	0.0	0.0	0.6	0.3	0	0

Table 4.4: Data compared with the expected number of events from the Drell-Yan Monte Carlo + QCD + EWK background events.

expression :

$$\cos\theta = \frac{2}{M\sqrt{M^2 + P_T^2}} \left(\ell_1^+ \ell_2^- - \ell_1^- \ell_2^+\right) \tag{4.2}$$

where M is the mass of dilepton pair, P_T is the dilepton transverse momentum, ℓ_1 is the lepton momentum, ℓ_2 is the anti-lepton momentum and $\ell^\pm = \frac{1}{\sqrt{2}}(\ell^0 \pm \ell^3)$. This formalism minimizes correction terms to the cross section introduced from the parton transverse momentum in comparison to those if the production angle were taken as the angle between the lepton momentum and proton beam.

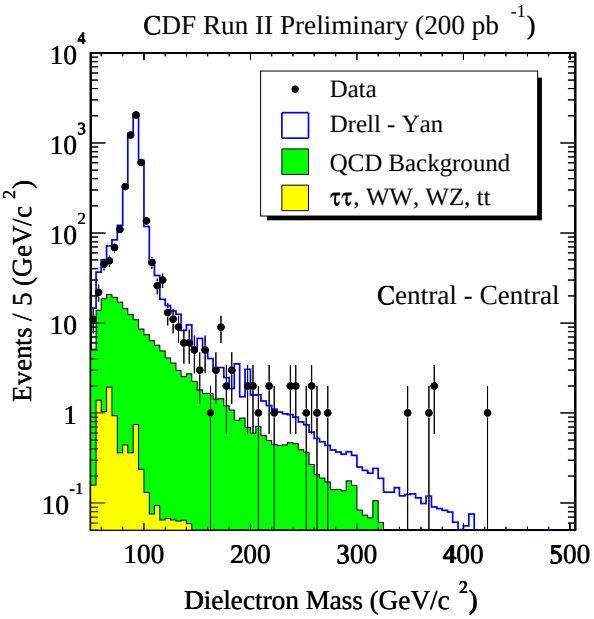

Figure 4.5: Comparison of dielectron mass distribution with the estimated Drell-Yan + QCD + EWK background events for the Central-Central.

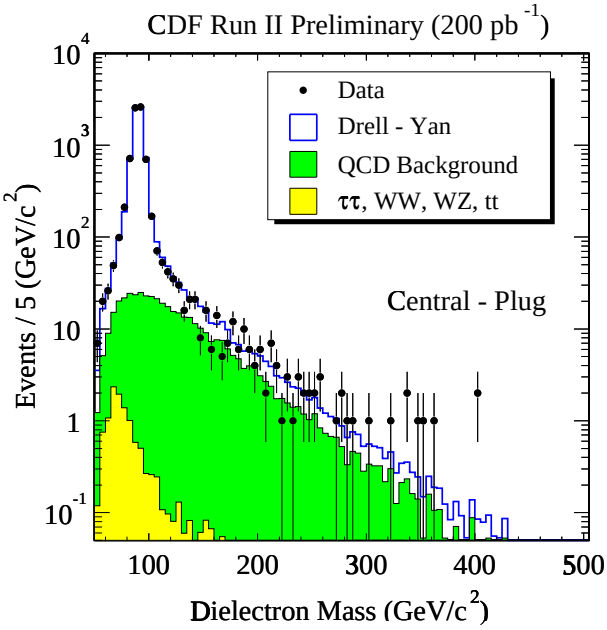

Figure 4.6: Comparison of dielectron mass distribution with the estimated Drell-Yan + QCD + EWK background events for the Central-Plug.

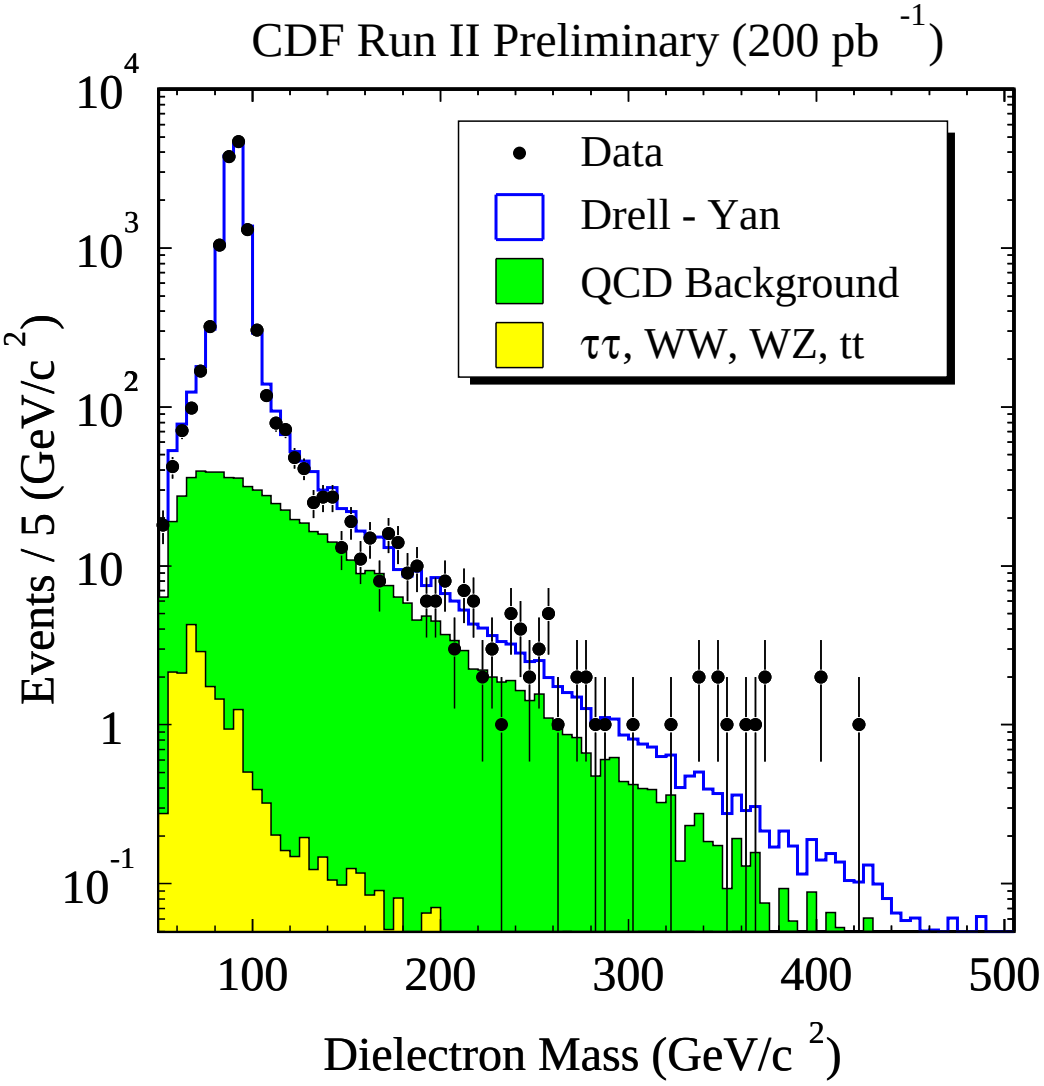

Figure 4.7: Comparison of dielectron mass distribution with the estimated Drell-Yan + QCD + EWK background events for Central-Central and Central-Plug together.

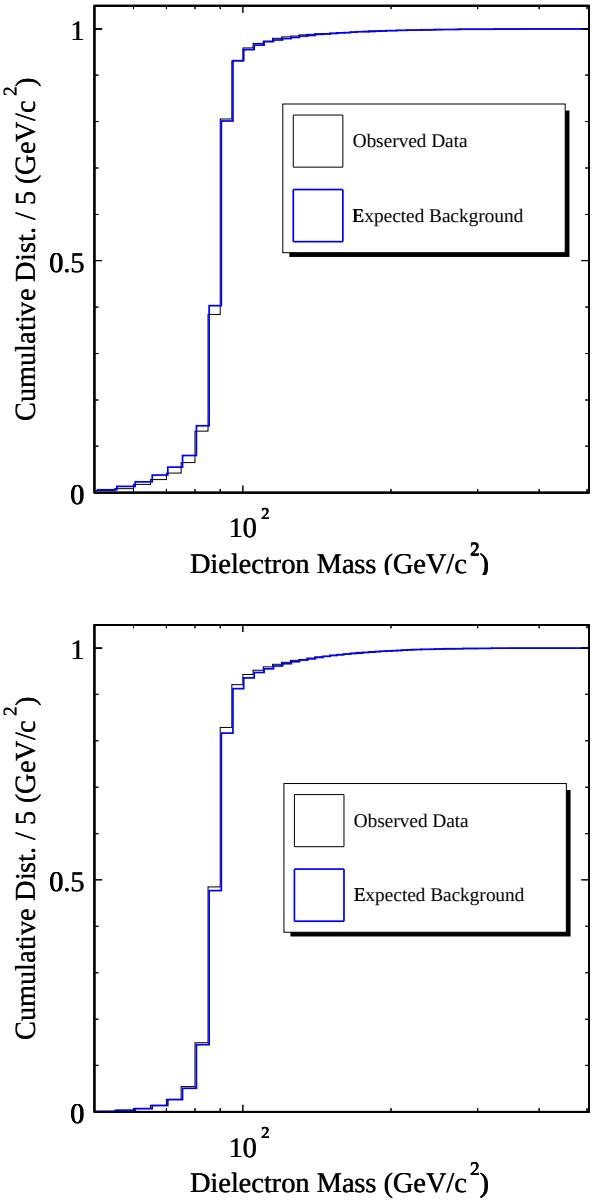

Figure 4.8: Data cumulative distribution function and background cumulative distribution for Central-Central (left) and Central-Plug (right).

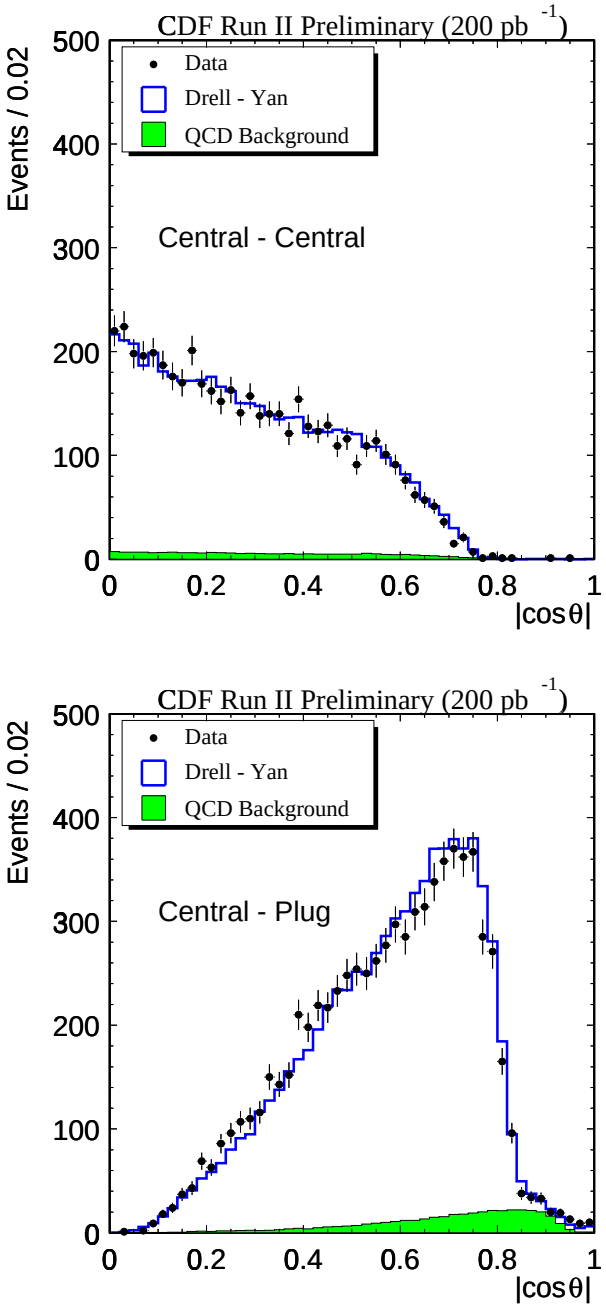

Figure 4.9: Comparison of $\cos\theta$ distribution with the estimated Drell-Yan + QCD background events.

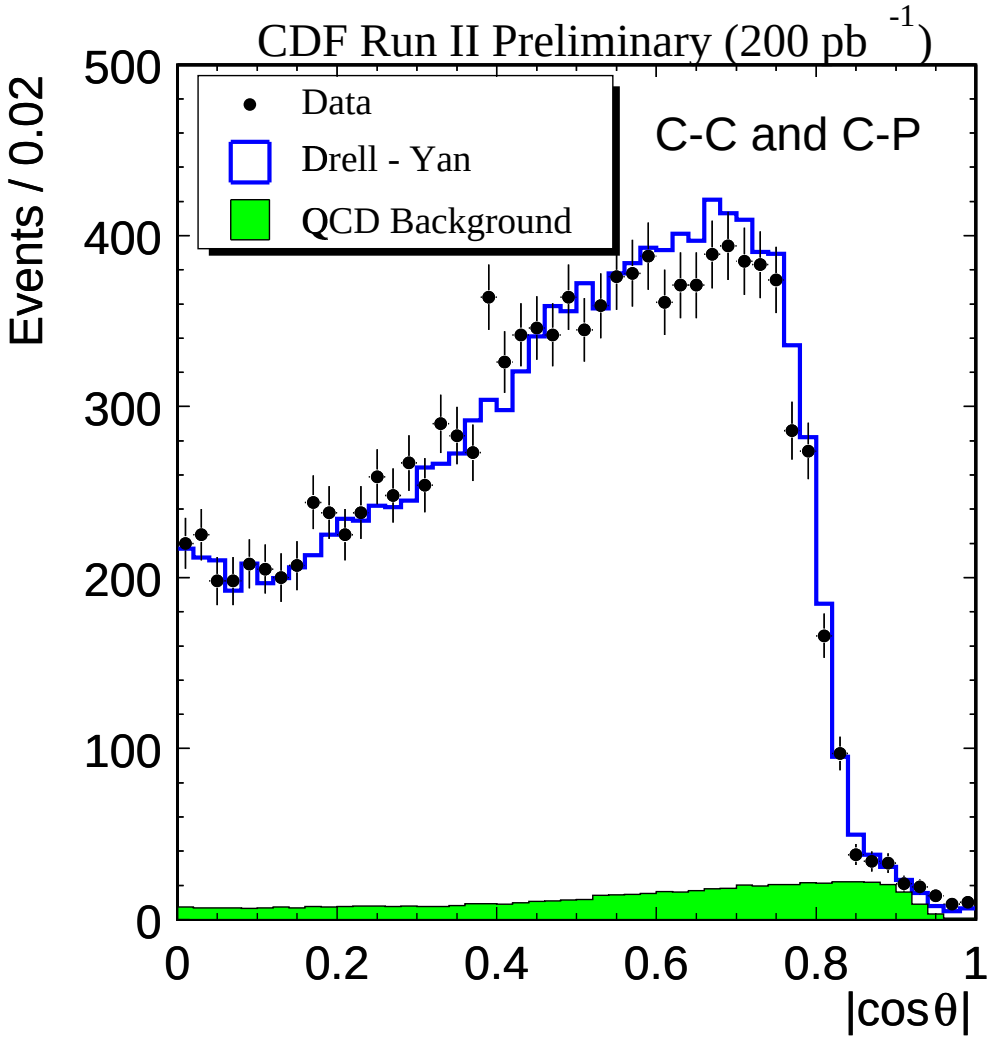

Figure 4.10: Comparison of $\cos\theta$ distribution with the estimated Drell-Yan + QCD background events.

Chapter 5

Efficiency and Acceptance

To set the cross section upper limits and determine the lower mass limits for new resonant particles and set limits on effective Planck scale, we need to estimate efficiencies. We describe the estimation of the efficiencies of the selection cuts and acceptance in this chapter.

5.1 Efficiencies of the Electron Selection Cuts

Efficiency of electron pair identification cuts, ε_{CC} for Central-Central events and ε_{CP} for Central-Plug events, can be written as

$$\varepsilon_{CC} = 2\varepsilon_T \cdot \varepsilon_L - \varepsilon_T^2 \quad (5.1)$$

$$\varepsilon_{CP} = \varepsilon_T \cdot \varepsilon_P \quad (5.2)$$

where ε_T, ε_L and ε_P are total efficiencies for the tight central electron cuts, for the loose electron cuts and for the plug electron cuts, respectively.

We use $Z \to e^+e^-$ sample to estimate electron selection efficiencies. To estimate the electron selection efficiencies, we use Central-Central $Z \to e^+e^-$ with $\Delta M = 40$ (70 GeV/c^2 < $M_{e^+e^-}$ < 110 GeV/c^2) for central electron, and Central-Plug $Z \to e^+e^-$ with $\Delta M = 10$ (85 GeV/c^2 < $M_{e^+e^-}$ < 95 GeV/c^2) for plug electron.

The efficiencies of the electron selection cuts are determined from a sample of $Z \to e^+e^-$, in which no selection biases are applied to one of the legs. To ensure a clean Z sample the events are required to have a central electron satisfying stringent identification requirement and a certain dielectron invariant mass. The stringent electron cuts include the tight central electron

selection cuts and also a requirement that there be a track pointing to the central EM cluster of that electron. The second leg can be in the central or plug calorimeter with none of the analysis cuts applied.

The individual efficiencies for the central region, ε_C^i, are calculated as :

$$\varepsilon_C^i = \frac{N_i + N_{TT}}{N_{CC} + N_{TT}}, \tag{5.3}$$

where N_i is the number of the 2nd leg electrons passing the individual cut subtracting background events and N_{CC} and N_{TT} are defined below. The individual efficiencies for the plug region, ε_P^i, are calculated as :

$$\varepsilon_P^i = \frac{N_i}{N_{CP}}, \tag{5.4}$$

where N_{CP} is defined below.

The total efficiency for the tight central electron cut (ε_T), loose central electron cuts (ε_L) and plug electron cut (ε_P) can be expressed as

$$\varepsilon_T = \frac{N_{TT} + N_{TT}}{N_{CC} + N_{TT}}, \tag{5.5}$$

$$\varepsilon_L = \frac{N_{TL} + N_{TT}}{N_{CC} + N_{TT}}, \tag{5.6}$$

$$\varepsilon_P = \frac{N_{TP}}{N_{CP}}, \tag{5.7}$$

where N_{CC}, N_{CP}, N_{TT}, N_{TL} and N_{TP} are defined by

$$N_{CC} \equiv N_{CC}^{obs} - 2 \times N_{CC}^{same}, \tag{5.8}$$

$$N_{TT} \equiv N_{TT}^{obs} - 2 \times N_{TT}^{same}, \tag{5.9}$$

$$N_{TL} \equiv N_{TL}^{obs} - 2 \times N_{TL}^{same}, \tag{5.10}$$

$$N_{CP} \equiv \text{number of central - plug } Z \text{ events}, \tag{5.11}$$

$$N_{TP} \equiv \text{number of central (tight) - plug (loose) events}, \tag{5.12}$$

with

$$N_{CC}^{obs} \equiv \text{number of central - central } Z \text{ events}, \tag{5.13}$$

$$N_{TT}^{obs} \equiv \text{number of central (tight) - central (tight) } Z \text{ events}, \tag{5.14}$$

$$N_{TL}^{obs} \equiv \text{number of central (tight) - central (loose) } Z \text{ events}, \tag{5.15}$$

and

$$N_{CC}^{same} \equiv \text{number of central - central same-sign events}, \tag{5.16}$$

CDF Run II Preliminary (200 pb^{-1})

Cut	Number of candidate events	Number of background	Efficiency (%)
$Iso < 0.1$	4686	146	97.2± 0.2
$Iso < 0.2$	4912	204	99.0± 0.1
$E_{had}/E_{em} < 0.055 + 0.00045 \times E$	4962	252	99.0± 0.1
$E/P < 4.0$(for $E_T < 100$)	5357	562	99.9± 0.0
$\|\Delta X\| < 3.0$	5210	508	98.9± 0.1
$\|\Delta Z\| < 5.0$	5299	532	99.7± 0.1
$L_{shr} < 0.2$	4988	304	98.7± 0.1
Tight central overall(ε_T)	4406	108	94.5± 0.2
Tight central overall(ε_L)	4569	120	96.2± 0.2
$\varepsilon_{CC}(= 2 \cdot \varepsilon_T \cdot \varepsilon_L - \varepsilon_T^2)$			92.4± 0.4

Table 5.1: Efficiency of the analysis cuts for central electron.

$$N_{TT}^{same} \equiv \text{number of central (tight) - central (tight) same-sign events,} \quad (5.17)$$

$$N_{TL}^{same} \equiv \text{number of central (tight) - central (loose) same-sign events.} \quad (5.18)$$

Table 5.1 and Table 5.2 show the electron selection efficiencies for central electron and for plug electron, respectively. ε_T, ε_L and ε_P are $94.5 \pm 0.2\%$, $96.2 \pm 0.2\%$ and $83.8 \pm 0.5\%$, respectively. Hence, we calculate ε_{CC} and ε_{CP} to be $92.4 \pm 0.4\%$ and $79.2 \pm 0.5\%$,respectively.

CDF Run II Preliminary (200 pb^{-1})

Cut	candidate events	Efficiency (%)
$Iso < 0.1$	5621	92.8± 0.3
$E_{had}/E_{em} < 0.055 + 0.00045 \times E$	5837	96.4± 0.2
$\chi^2_{3\times3}$	5161	85.2± 0.5
Plug overall (ε_P)	5075	83.8± 0.5
ε_{CP} $(= \varepsilon_T \cdot \varepsilon_P)$		79.2± 0.5

Table 5.2: Efficiency of the analysis cuts for plug electron.

5.2 Other Efficiencies

To establish efficiencies of the S cut, we use a sample of Z events , with invariant mass of the electron pairs between 70 GeV/c^2 and 110 GeV/c^2. In addition, we require that the electron pairs have opposite charge. After requiring $S < 2.5$ on the Z sample, we get 99.8 ± 0.1 of efficiency. The efficiency of the vertex cut $|z_0| < 60$ cm is estimated to be 95.1 ± 0.5. Electron_Central_18 trigger efficiency is $96.8 \pm 0.1\%$.

5.3 Geometrical and Kinematical Acceptance

Monte Carlo simulation is used for determination of the geometrical and kinematical acceptance. The Monte Carlo events are generated by using the leading order diagrams for Z', Randall-Sundrum graviton and Higgs productions. Higgs production is used for the estimation of the acceptance of spin-0 particles production. The CTEQ5L parton distribution function is used. The generated events are simulated and reconstructed with the offline version 4.9.1. We generate 5,000 events for various mass of Z', Randall-Sundrum graviton and Higgs particles. Figure 5.1 shows dielectron invariant mass distributions for various mass of Monte Carlo Z' samples. We assume that the coupling strengths of Z' to quarks and leptons were the same as those for the standard model Z. The Z' width is set to the Z width scaled by a factor $M_{Z'}/M_Z$. For the production of Randall-Sundrum graviton, we set k/M_{Pl} to be 0.1. k/M_{Pl} is a dimensionless coupling which determines graviton width. For the production of Higgs particles, we set the mass width to be 0. We apply extra energy smearing for Monte Carlo events as described in 4.1. The same fiducial region of calorimeter is considered and a kinematical requirement, $E_T > 25$ GeV, is required. Figure 5.2 shows the geometrical and kinematical acceptance as a function of M for Central-Central, Central-Plug and both events. For comparison, the acceptance of $Z \to e^+e^-$ is shown at $M = 91\text{GeV/c}^2$. We note that in the high invariant mass of dielectron region, the Central-Central events in the fiducial region are dominant.

The difference of the geometrical and kinematical acceptance of Higgs, Z' and Randall-Sundrum graviton comes from the difference of the spin. A spin-0 resonance has a flat angular distribution, spin-1 corresponds to a parabolic shape, and spin-2 yields a quartic distribution (Figure 5.5).

For the generation of the large extra dimension processes, we modify PYTHIA and include

these processes [19, 18] into PYTHIA. The matrix element we use is :

$$\begin{aligned}
\sigma(q\overline{q} \to \ell^+\ell^-) &= -\frac{\lambda}{M_s^4}\frac{\pi\alpha Q_q}{12s^2}\left(\frac{t-u}{s}\right)\left[s^2 - 2(t^2+u^2) - (t-u)^2\right] \\
&\quad -\frac{\lambda}{M_s^4}\frac{\alpha}{48\pi s^2}\left(\frac{\pi}{2\sin\theta_{\rm W}\cos\theta_{\rm W}}\right)^2 \frac{s-M_Z^2}{(s-M_Z^2)^2+M_Z^2\Gamma_Z^2} \\
&\qquad \times\left[(L_\ell L_q + R_\ell R_q)\, t^2(t-3u) - (L_\ell R_q + R_\ell L_q)\, u^2(u-3t)\right] \\
&\quad +\left(\frac{\lambda}{M_s^4}\right)^2 \frac{1}{192s^2}\left[s^4 - 4s^2(t-u)^2 + (t-u)^2(5t^2-6tu+5u^2)\right] \quad (5.19) \\
\sigma(gg \to \ell^+\ell^-) &= \left(\frac{\lambda}{M_s^4}\right)^2 \frac{\pi}{64s^2}\left[s^4 + 2tu(t-u)^2\right] \quad (5.20)
\end{aligned}$$

where $L_\ell = \sin^2\theta_{\rm W} - 2$, $R_\ell = 4\sin^2\theta_{\rm W}$, $L_q = 4\,(T_{3q} - Q_q\sin^2\theta_{\rm W})$ and $R_q = -4Q_q\sin^2\theta_{\rm W}$. The interference term is proportional to $\frac{\lambda}{M_s^4}$ and the direct production term is proportional to $(\frac{\lambda}{M_s^4})^2$. We generate $10,000$ events for the interference term and $10,000$ events for the direct production term of LED process. The generated events are simulated and reconstructed with the offline version 4.9.1. Geometrical and kinematical acceptance for the interference term are $27.5\pm0.4\%$ for Central-Central and $17.9\pm0.4\%$ for Central-Plug. For the direct production term, acceptance are $32.6 \pm 0.4\%$ for Central-Central and $12.2 \pm 0.3\%$ for Central-Plug. Figure 5.6 shows dielectron invariant mass distributions for direct production and interference term of the large extra dimension processes. Figure 5.7 shows the dielectron invariant mass distributions of the large extra dimension processes with comparison of observed events and expected SM background for Central-Central and Central-Plug for $M_s = 850$ GeV.

5.4 Total Efficiency

The total detection efficiency ε_{tot} can be written as

$$\varepsilon_{tot} = \varepsilon_{Acc} \times \varepsilon_{ID} \times \varepsilon_{z_0} \times \varepsilon_{trig} \times \varepsilon_S \quad (5.21)$$

where ε_{Acc} is a geometrical and kinematical acceptance. For the resonant particles (Z', Randall-Sundrum graviton and sneutrino), ε_{Acc} is a function of mass as described in 5.3. ε_{ID} is an efficiency of electron identification cuts, ε_{z_0} is an efficiency of the event vertex cut, ε_{trig} is the trigger efficiency, and ε_S is the missing E_T significance cut efficiency. We assume 100% for the trigger efficiency in the total efficiency for setting limits.

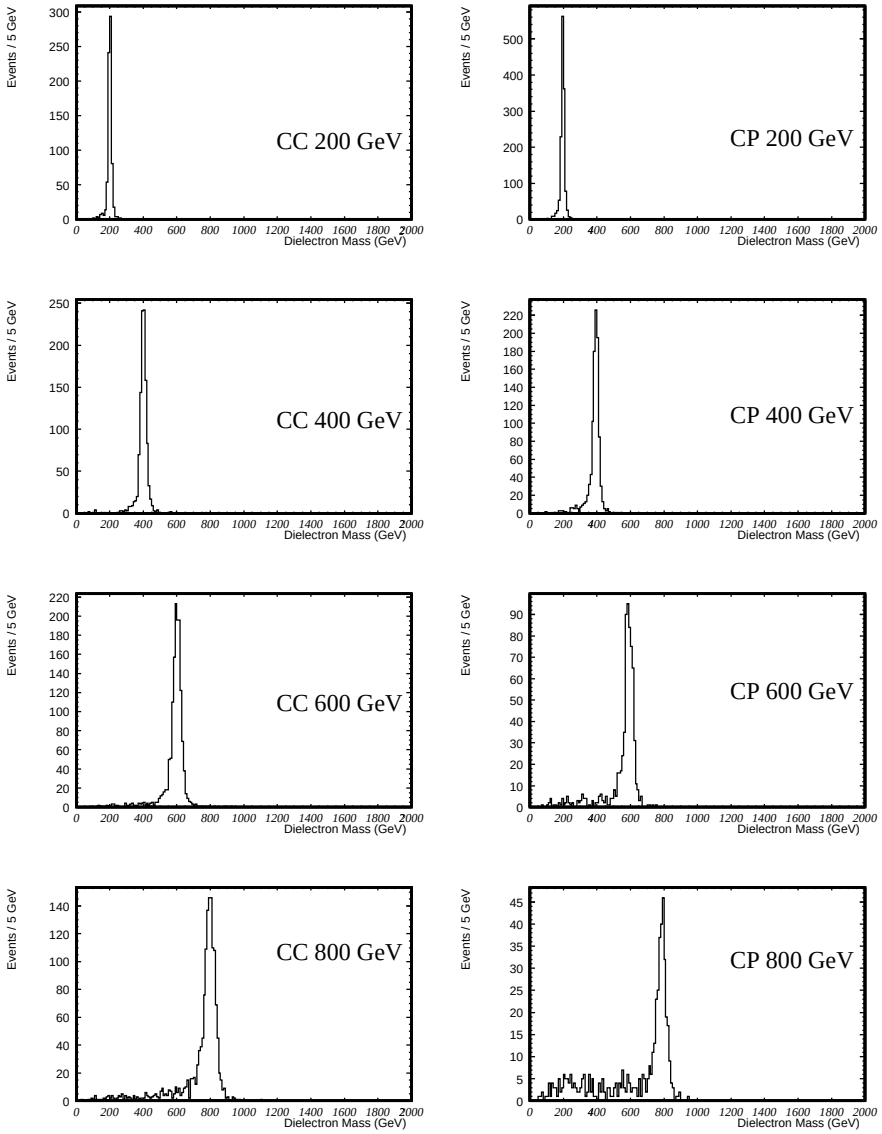

Figure 5.1: Dielectron invariant mass distributions for various mass of Monte Carlo Z' samples.

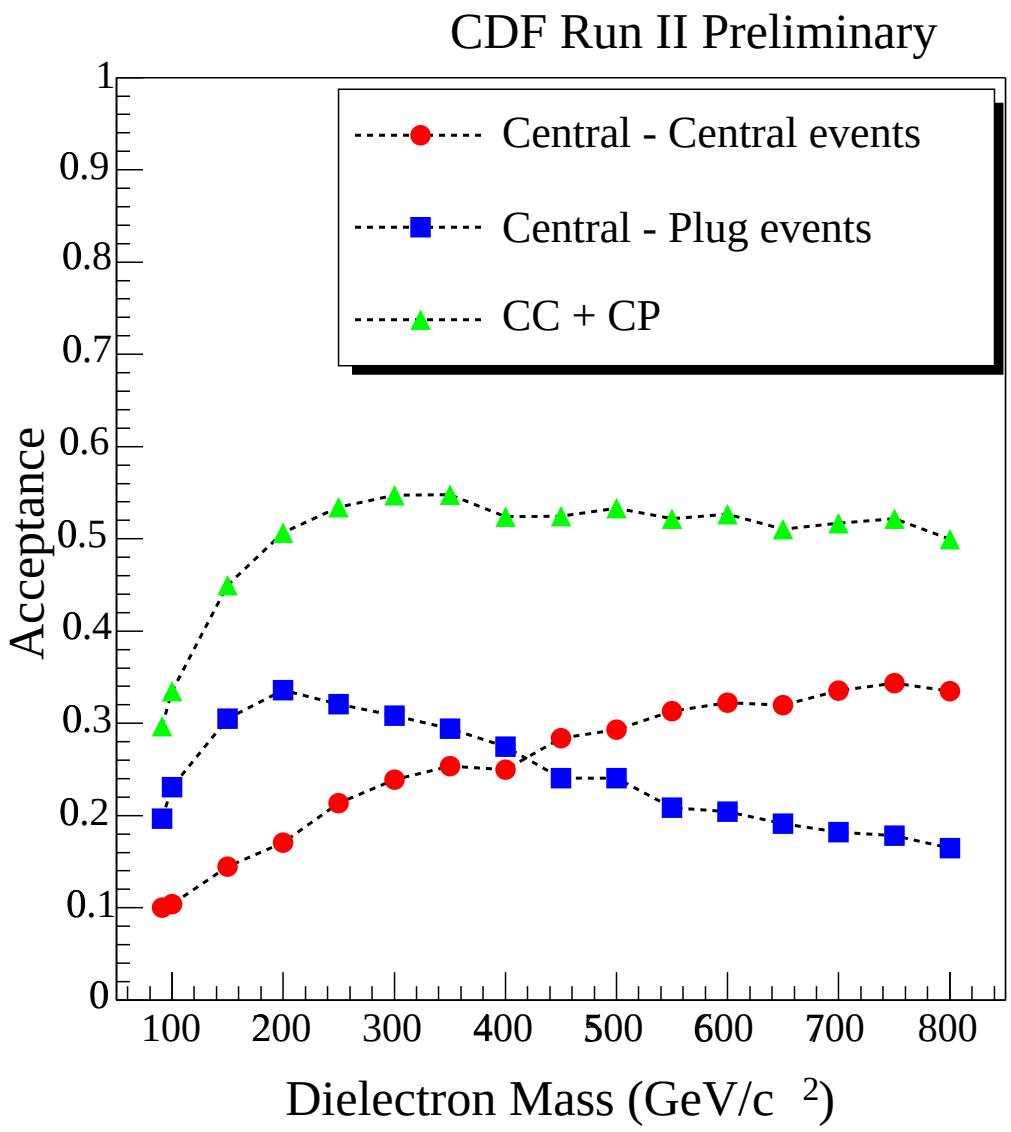

Figure 5.2: Dielectron mass dependency of geometrical and kinematical acceptance of Z'.

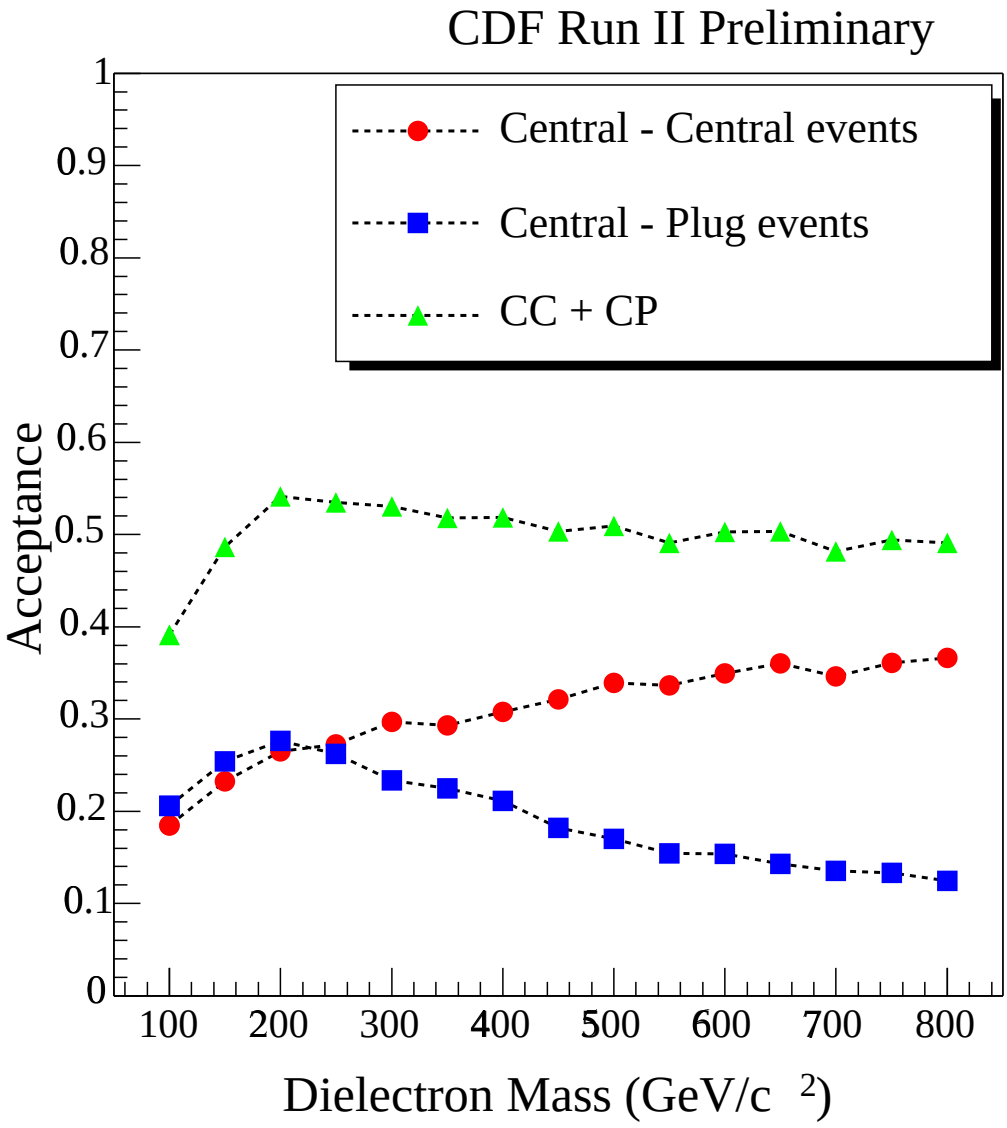

Figure 5.3: Dielectron mass dependency of geometrical and kinematical acceptance of Randall-Sundrum graviton.

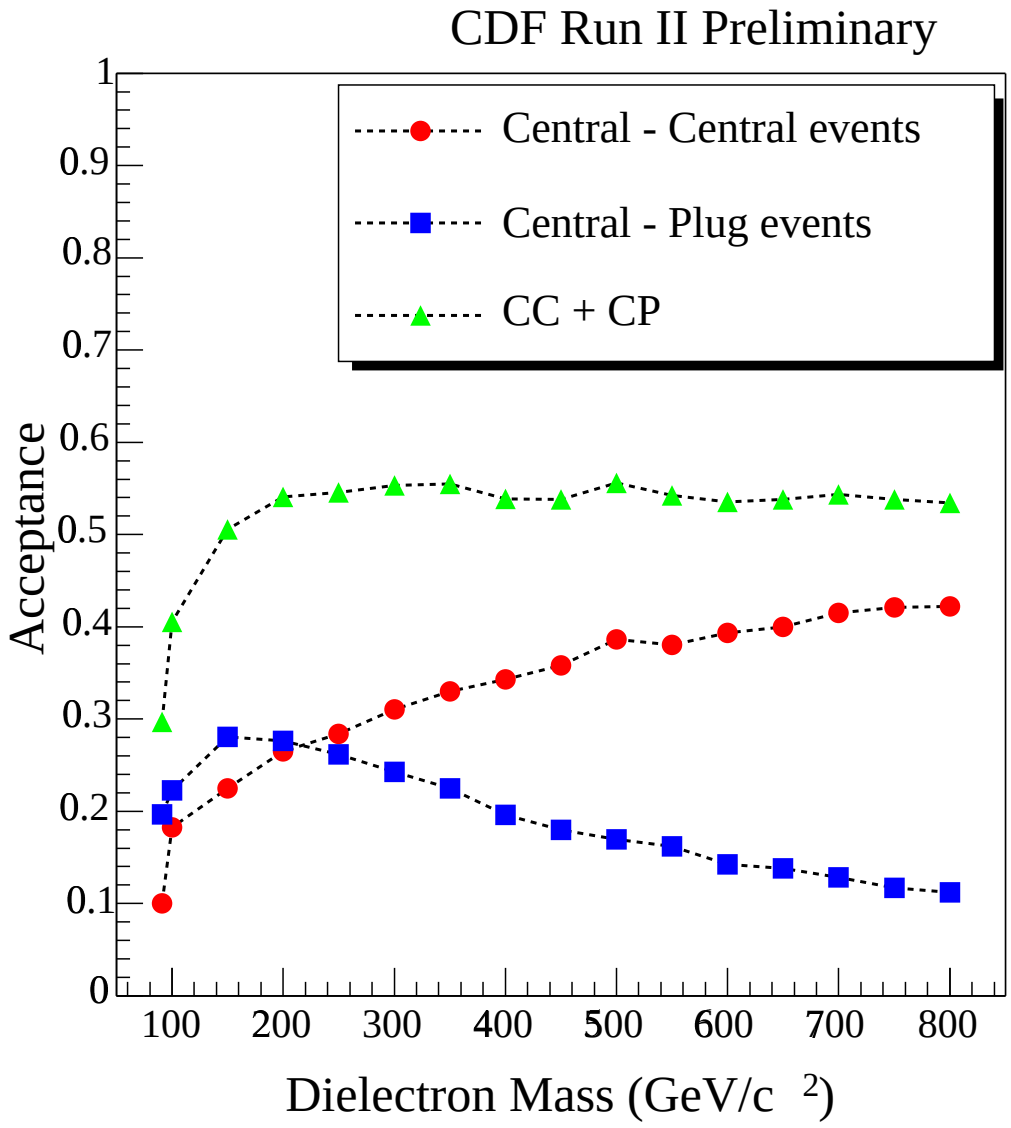

Figure 5.4: Dielectron mass dependency of geometrical and kinematical acceptance of scalar particle.

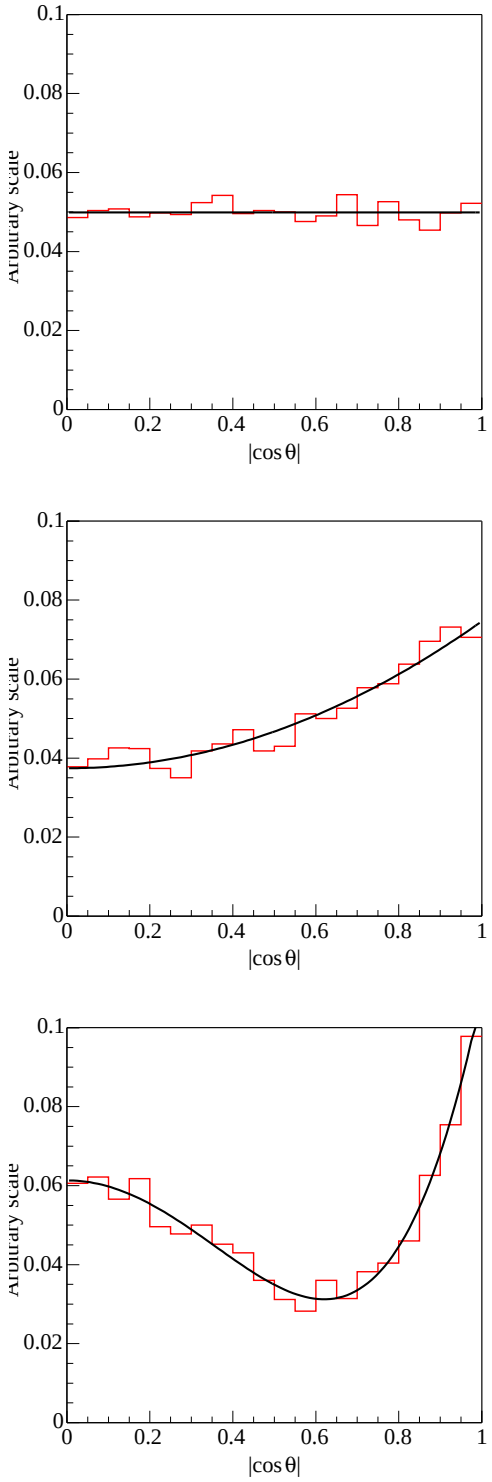

Figure 5.5: Angular distributions for a spin-0, spin-1 and spin-2 particles at $M = 600$ GeV (generator level).

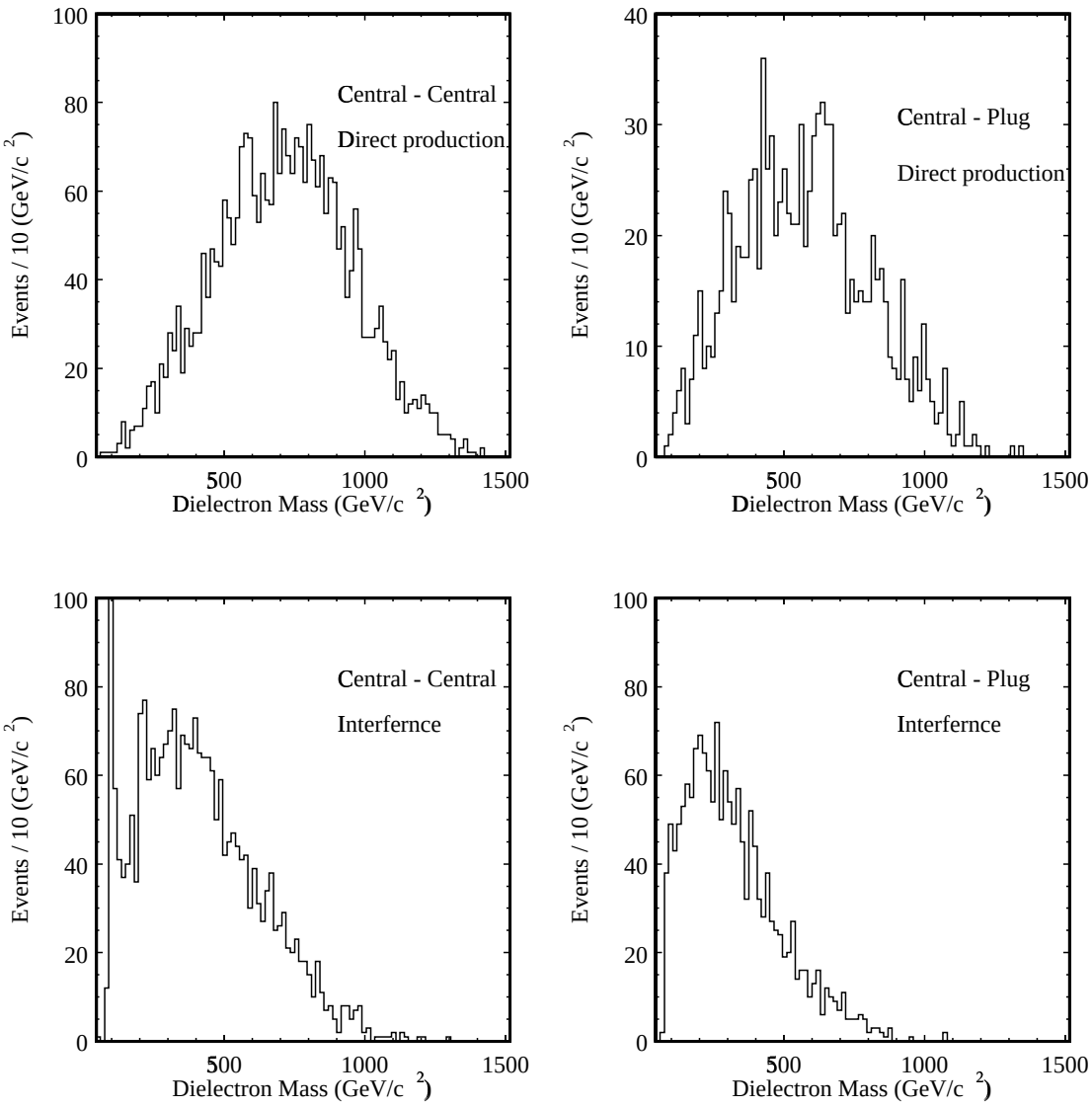

Figure 5.6: Dielectron invariant mass distributions for direct production and interference term of the large extra dimension processes.

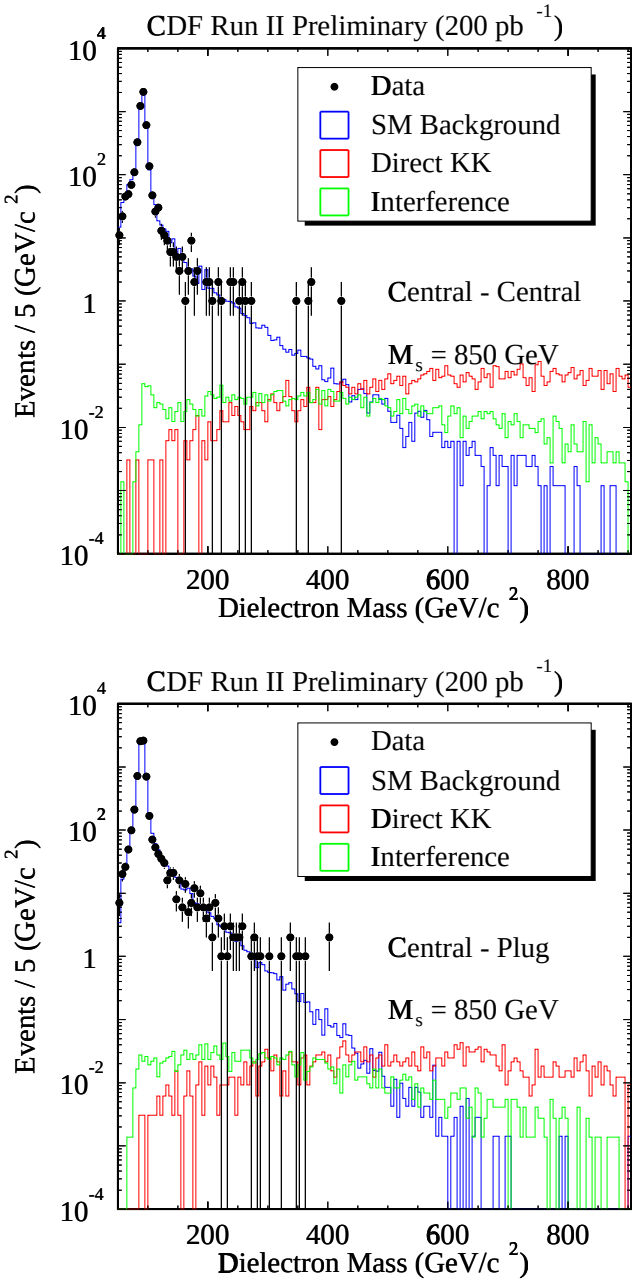

Figure 5.7: Dielectron invariant mass distributions of observed events with expected ones from Drell-Yan Monte Carlo events, the QCD background events, the Electroweak background events other than Drell-Yan and LED for Central-Central and Central-Plug.

	Central-Central	**Central-Plug**
Acceptance (A_Z)	$10.1 \pm 0.1\%$	$18.3 \pm 0.7\%$
ID Efficiency (ε_{ID})	$92.4 \pm 0.4\%$	$79.2 \pm 0.5\%$
Trigger efficiency (ε_{trig})	$99.9 \pm 0.1\%$	$96.8 \pm 0.1\%$
$\lvert z_0 \rvert < 60$ cm cut efficiency (ε_{z_0})	$95.2 \pm 0.5\%$	$95.2 \pm 0.5\%$
Observed Events (N_Z)	4573	7095
Expected Background Events (N_{BG})	91.6	194.4
Integrated Luminosity (pb^{-1})	199.6 ± 11.7	
Z boson cross section ($\sigma \cdot Br$)	$254.5 \pm 3.9 \pm 15.5$	$261.7 \pm 5.8 \pm 18.7$

Table 5.3: Z boson cross section and parameters for the cross section calculation.

5.5 Z Boson Cross Section

To check our analysis, we calculate the Z boson cross section times branching fraction decaying to dielectron $\sigma \cdot Br(Z \to e^+e^-)$. The cross section is calculated using following formula

$$\sigma \cdot Br(p\bar{p} \to Z \to e^+e^-) = \frac{N_Z - N_{BG}}{A_Z \cdot \varepsilon_{ID} \cdot \varepsilon_{trig} \cdot \varepsilon_{z_0} \cdot \mathcal{L}} \tag{5.22}$$

where N_Z is the number of observed $Z \to e^+e^-$ candidates and N_{BG} is the estimated number of QCD background and dielectron events other than Drell-Yan. A_Z is the kinematical and geometrical acceptance of $Z \to e^+e^-$ estimated from Monte Carlo. ε_{ID} is the dielectron selection efficiency, ε_{trig} is the trigger efficiency, ε_{z_0} is the $|z_0| < 60$ cut efficiency and $\mathcal{L}$ is the integrated luminosity.

To select the Z boson candidates, we require that the dielectron invariant mass should be between 70 GeV/c^2 and 110 GeV/c^2. With this requirement, a sample of 11668 Z's is obtained (4573 of these are Central-Central events and 7095 are Central-Plug events). Integrated luminosity for this calculation is 199.6 ± 11.7 pb^{-1}. These parameters and Z boson cross section are summarized in Table 5.3. The first error is statistical and the second error corresponds to the systematic uncertainty. NNLO theoretical calculation of $\sigma \cdot Br(Z \to e^+e^-)$ is 252 pb. Our calculation agrees with theoretical calculation within errors.

Chapter 6

Limits on new physics

In this chapter, we conclude that we observe high mass dielectron events at a rate expected background processes. We set upper limits on the cross section of resonant particles (spin-0, spin-1 and spin-2) times branching ratio decaying into dielectrons ($\sigma \cdot Br(e^+e^-)$) as a function of the invariant mass of new particles and finally determine the lower mass limits for new particles. We also set lower limits on the effective Planck scale of large extra dimensions.

6.1 Procedure for setting limit

A binned likelihood method is used with the contents of the bins treated with Poisson statistics. The probability associated with ith bin is

$$P_i(n_i, \mu_i) = \frac{\mu_i^{n_i} e^{-\mu_i}}{n_i!}, \tag{6.1}$$

where n_i is the number of events observed in ith bin, μ_i is the number of events expected in the ith bin :

$$\mu_i = \alpha N_i^s + N_i^b \tag{6.2}$$

with N_i^s and N_i^b the number of events predicted in the ith bin by new particles and background expected, respectively. Expected background events are fixed as described in section 4.4. The likelihood function is defined as the total probability, which is the product of the individual probabilities for each bin,

$$L(\alpha) = \prod_{i=1}^{N} P_i(n_i, \mu_i) = \prod_{i=1}^{N} \frac{\mu_i^{n_i} e^{-\mu_i}}{n_i!}, \tag{6.3}$$

where N is the total number of bins. The 95% C. L. upper limit on $\alpha(\equiv \alpha_{95})$ is calculated by

$$0.95 = \frac{\int_0^{\alpha_{95}} L(\alpha)d\alpha}{\int_0^{\infty} L(\alpha)d\alpha} \tag{6.4}$$

We calculate the likelihood function for Central-Central (L_{CC}) and Central-Plug (L_{CP}) separately. Total likelihood function is defined by

$$L_{CC+CP}(\alpha) = L_{CC}(\alpha) \times L_{CP}(\alpha) \tag{6.5}$$

The 95% C. L. lower limit on the number of signal events (N_{95}) is obtained by

$$N_{95} = \alpha_{95} \times N^s \tag{6.6}$$

Then it can be translated to the 95% C. L. limit on the production cross section times branching ratio (σ_{95}) by

$$\sigma_{95} = \frac{N_{95}}{\mathcal{L} \cdot \varepsilon} = \frac{\alpha_{95} \times N^s}{\mathcal{L} \cdot \varepsilon} = \alpha_{95} \times \sigma_{exp}, \tag{6.7}$$

where σ_{exp} is total expected cross section for new particle mass.

For the effective Planck scale (M_s), we also use binned likelihood method. The effective cross section of Drell-Yan process (SM+LED) is factorizable into parameter-independent shapes multiplied by factors of η :

$$\sigma = \sigma_{SM} + \eta\sigma_{int} + \eta^2\sigma_{KK} \tag{6.8}$$

where $\eta = \frac{\lambda}{M_s^4}$. and λ is a dimensionless parameter of order ± 1. In order to set limits on M_s, we set limits on η by calculating likelihood function of η ($L(\eta)$),

$$L(\eta) = \prod_{i=1} \frac{\mu_i^{n_i} e^{-\mu_i}}{n_i!} \tag{6.9}$$

We calculate the likelihood function for Central-Central (L_{CC}) and Central-Plug (L_{CP}) separately. Total likelihood function is defined by

$$L_{CC+CP}(\eta) = L_{CC}(\eta) \times L_{CP}(\eta) \tag{6.10}$$

We define 95% C. L. limits on η (η_{95}) as the following :

$$0.95 = \frac{\int_0^{\eta_{95}} L(\eta)d\eta}{\int_0^{\infty} L(\eta)d\eta} \tag{6.11}$$

We note that in the limit of infinite statistics likelihood function becomes a Gaussian as a consequence of the central limit theorem. In this case, the integral (6.4) and (6.11) become equivalent to

$$\ln L = \ln L_{max} - \frac{s^2}{2} \tag{6.12}$$

where s is the number of standard deviations. For 95% C. L. one finds $s = 1.96$. The corresponding limit value then follows from

$$\ln L_{max} - \ln L = 1.92 \tag{6.13}$$

Figure 6.1 shows the logarithm of a likelihood function compared to the likelihood function itself. This illustrates the two different methods which can be used to arrive at the 95% C.L. on a parameter. Generally, both methods of maximum likelihood and likelihood integration yields same limits. However, we use likelihood integration for setting limits.

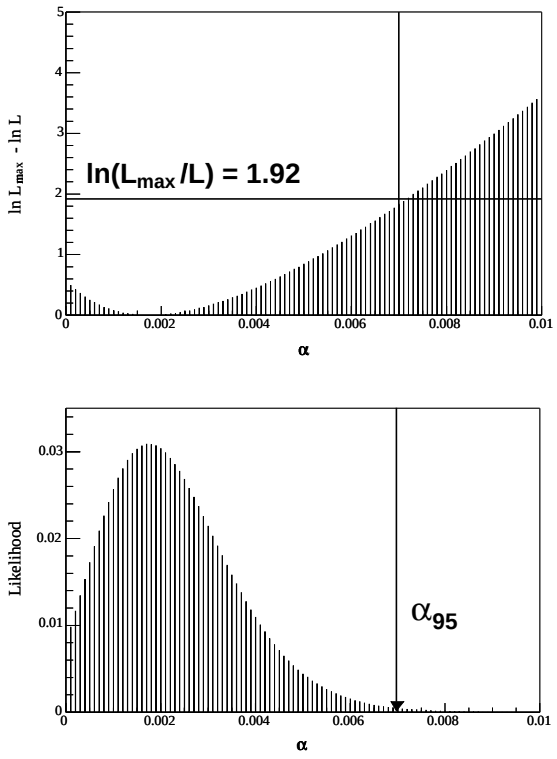

Figure 6.1: The logarithm of a likelihood function (top) compared to the likelihood function itself (bottom), illustrating the two different methods which can be used to arrive at the 95% C. L. on a parameter.

6.2 Systematic uncertainties

To account for the effects of systematic uncertainties on α and η, a set of pseudo-experiments is performed. We generate pseudo-experiments (100 events for resonant particles and 1000 events

for LED) by Poisson fluctuating the expected number of signal and background events. For each pseudo-experiment, these numbers of events are selected according to the corresponding nominal templates. Each pseudo-experiments fit to these same templates to determine α_{fit} and η_{fit}. We do this using MINUIT by minimizing negative log likelihood where the likelihood function is defined in equations 6.3 and 6.9. Figure 6.2 shows the distributions of the fit variable α and the pull distributions from pseudo-experiments with the expected number of events for signal in the case where the Z' mass is 600 GeV/c^2 and $\alpha = 1$ for Central-Central and Central-Plug. α_{pull} is defined as $\alpha_{pull} = (\alpha_{true} - \alpha_{fit})/\alpha_{error}$ where α_{pull} is the error returned by the fit. Figure 6.3 shows the distributions of the fit variable η and the pull distributions from pseudo-experiments with the expected number of events for signal in the case where $\eta = 5 \times 10^{-12}$ GeV^{-4} for Central-Central and Central-Plug. η_{pull} is defined as $\eta_{pull} = (\eta_{true} - \eta_{fit})/\eta_{error}$ where η_{error} is the error returned by the fit.

Refitting each pseudo-experiments to the templates with 1σ varied yields a new fitted value α'_{fit} and η'_{fit}. We determine $\Delta\alpha$ and $\Delta\eta$ by looking at the difference of mean value of pseudo-experiments. This entire process is repeated for each mass point of resonant particles and η from 0.04×10^{-10} GeV^{-4} to 0.13×10^{-10} GeV^{-4}.

We consider the sources of systematic uncertainty as following :

- Luminosity

  6% uncertainty is estimated due the integrated luminosity.

- Acceptance calculation

  The geometrical and kinematical acceptance is calculated with the Monte Carlo simulation described in Section 5.3. We assume that the acceptance of background events is same as one of signal events. We employ different set of parton distribution function (PDF). Used PDF sets are CTEQ3L, CTEQ3M, GRV94L and GRV94M. We generate 5,000 events of Z' at 600 GeV/c^2 with different set of PDF. Uncertainties of 3% for Central-Central and 5% for Central-Plug are estimated in the acceptance due to the different PDF choice, independent of resonant particles and large extra dimensions. Another systematic uncertainty due to statistical error of the Monte Carlo acceptance calculation is 0.7% in the mass range above 150 GeV/c^2. We also estimate the relative change of the acceptance by increasing the amount of material in the detector. We estimate the systematic uncertainty due to increase of the mount of the material to be 0.3% for Central-Central and 2.6% for Cental-Plug. The changes include adding 10% of the material between the beamline

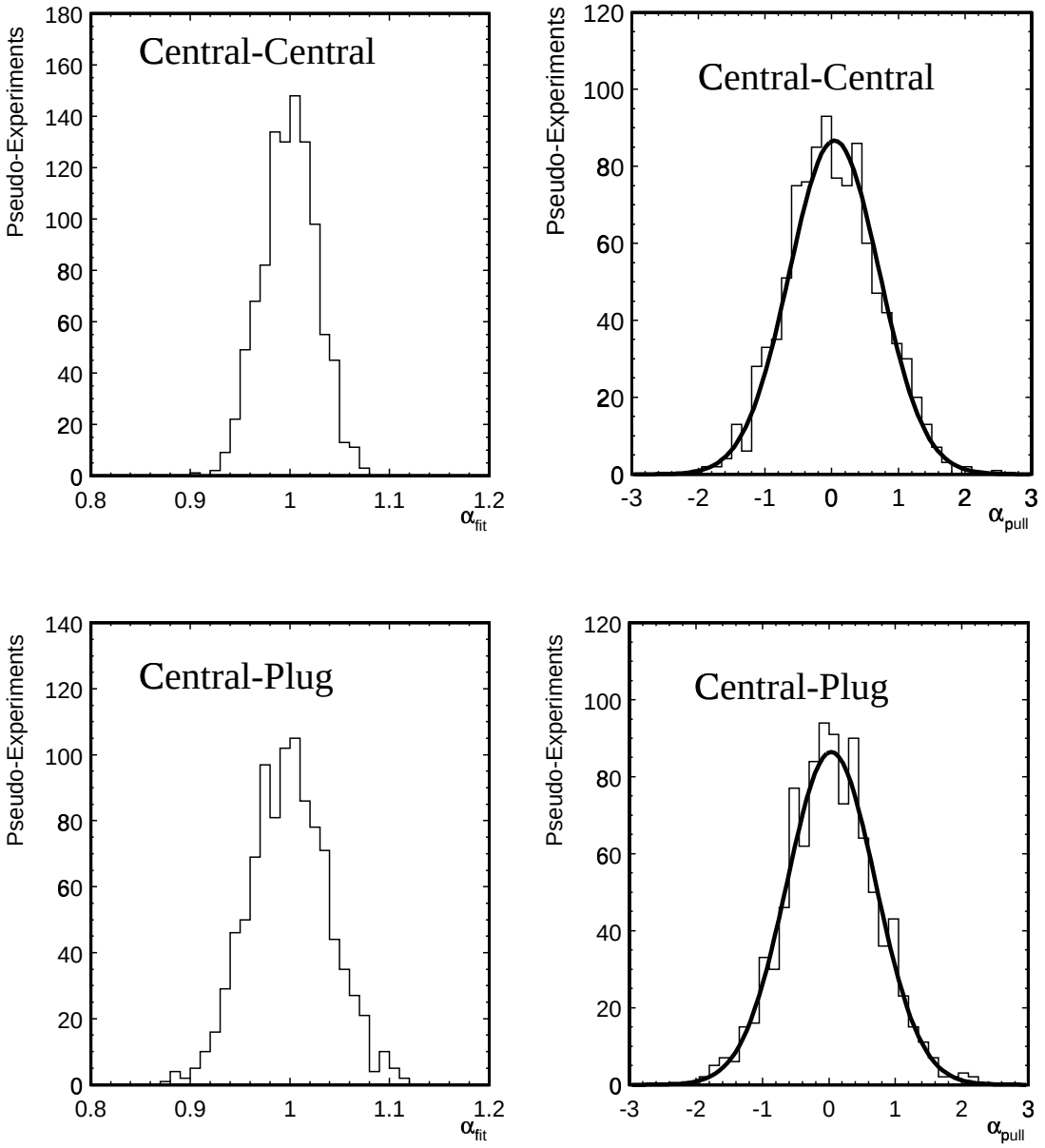

Figure 6.2: Results of pseudo-experiments with the expected number of events for signal in the case where the Z' mass is 600 GeV/c^2 and $\alpha = 1$ for Central-Central (top) and Central-Plug (bottom). Left two plots show the distributions of the fit variable α and right two plots show the pull distributions.

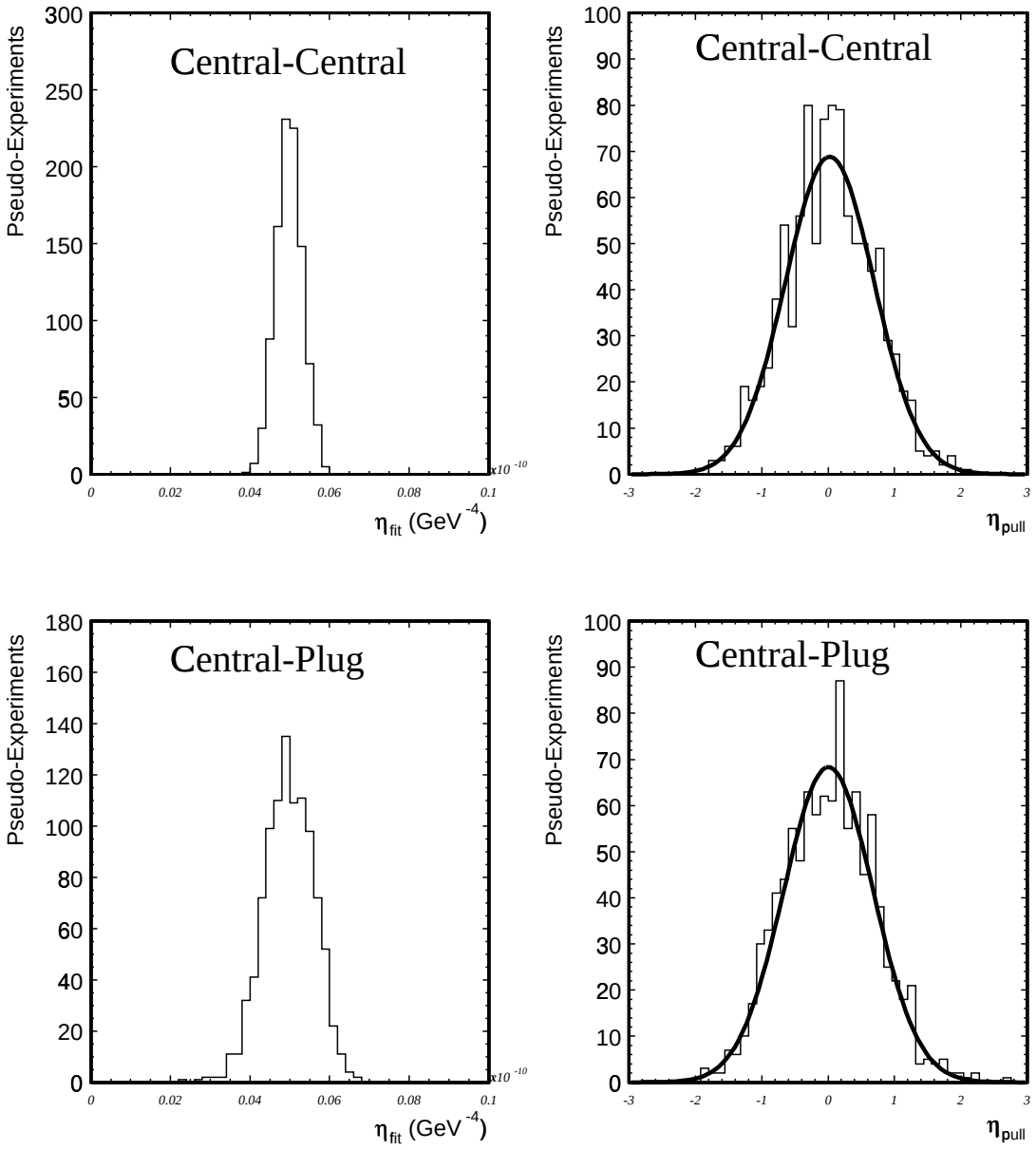

Figure 6.3: Results of pseudo-experiments with the expected number of events for signal in the case where $\eta = 5 \times 10^{-12}$ GeV^{-4} for Central-Central (top) and Central-Plug (bottom). Left two plots show the distributions of the fit variable η and right two plots show the pull distributions.

and the COT inner layer in the central region, and adding $0.5X_0$ to electrons in the plug region.

- Electron identification efficiency
  A systematic uncertainty due to the efficiency of electron identification cuts is 0.6% . This uncertainty is caused by statistical uncertainties in $Z \rightarrow e^+e^-$ control sample which is used to study the electron identification cuts.

- Event vertex
  A systematic uncertainty due to the efficiency of event vertex cut $z_0 < 60$ cm is estimated to be 0.5%.

- Energy scale
  To estimate uncertainty due to the energy scale, we choose to vary the energy scale by 1% for CEM and 2.5% for PEM.

- Energy resolution
  To estimate uncertainty due to the energy resolution, we remove smearing

- QCD background normalization
  We estimate $195 \pm 132.2(stat.) \pm 82.5(sys.)$ QCD background events in the Central-Central and $402.5 \pm 141.1(stat.) \pm 212.2(sys.)$ events in the Central-Plug categories. We take the statistical errors of the QCD background events as systematic uncertainties. To estimate systematic uncertainty for QCD background events, we change the regions A, B, C and D in Figure 4.3.

- QCD background shape
  To estimate systematic uncertainty due to the QCD shape, we add hadron energy to the default shape. Figure 6.4 shows the difference of QCD shape between the default ones and ones with hadron energy.

Table 6.1 and 6.2 show the systematic uncertainties as a function of mass for Z' for Central-Central and Central-Plug, respectively. Table 6.3 and 6.4 show the systematic uncertainties as a function of mass for Randall-Sundrum graviton for Central-Central and Central-Plug, respectively. Table 6.5 and 6.6 show the systematic uncertainties as a function of mass for sneutrino for Central-Central and Central-Plug, respectively. Systematics for high mass region of Central-Plug resonant particles go up. This is caused by low mass tail in Central-Plug mass distribution

for higher mass of particles as in Figure 5.1. Figure 6.5 and Figure 6.6 show the systematic uncertainty in η as a function of η of LED for $\lambda < 0$ and $\lambda > 0$, respectively.

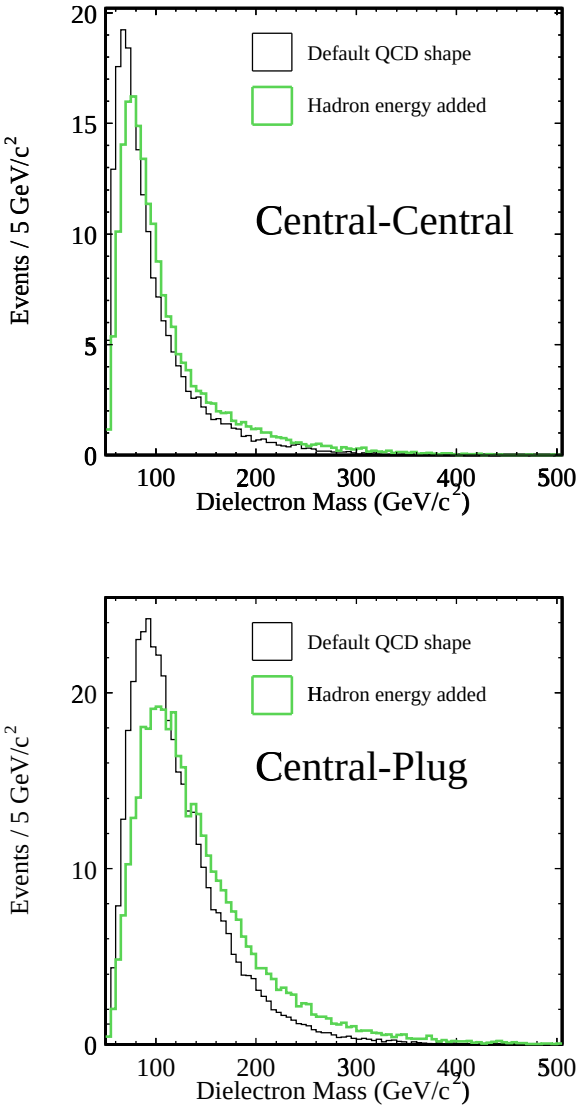

Figure 6.4: QCD background shape of default ones and ones with hadron energy added.

The full systematic uncertainty must be incorporated into the likelihood function. We convolve the systematic uncertainty into the likelihood function, L, by replacing each point of L by a Gaussian distribution centered at that point with width $\Delta\alpha$ or $\Delta\eta$. To get the value of a particular point of the smeared likelihood function, we integrate all the contributions from the

mass (GeV/c^2)	Lum.	Effi.	CEM resolution	CEM Scale	QCD shape	QCD normalize	Total
200	6.0%	5.1%	0.0%	0.9%	1.5%	2.1%	8.3%
250	6.0%	4.4%	0.3%	1.7%	1.6%	1.6%	7.9%
300	6.0%	4.7%	1.2%	2.0%	0.1%	1.1%	8.1%
350	6.0%	4.3%	0.3%	2.5%	0.3%	0.7%	7.8%
400	6.0%	4.3%	0.7%	4.0%	0.8%	0.7%	8.5%
450	6.0%	4.2%	0.0%	1.5%	0.4%	0.4%	7.5%
500	6.0%	4.7%	0.7%	1.0%	0.7%	0.6%	7.8%
550	6.0%	4.3%	0.7%	0.3%	0.2%	0.3%	7.5%
600	6.0%	4.8%	0.6%	0.7%	0.3%	0.7%	7.8%
650	6.0%	4.6%	0.8%	1.1%	0.7%	0.9%	7.8%
700	6.0%	4.6%	1.3%	1.0%	0.9%	0.6%	7.8%
750	6.0%	4.3%	2.4%	2.3%	0.3%	0.3%	8.1%
800	6.0%	4.3%	0.7%	1.2%	0.0%	0.9%	7.6%

Table 6.1: Systematic uncertainty in α as a function of $Z^{'}$ mass for Central-Central.

mass (GeV/c^2)	Lum.	Effi.	CEM resolution	CEM Scale	PEM resolution	PEM Scale	QCD shape	QCD normalize	Total
200	6.0%	8.2%	0.1%	0.1%	0.0%	3.7%	2.9%	4.5%	12.0%
250	6.0%	8.3%	0.0%	0.9%	0.2%	3.1%	2.4%	2.6%	11.3%
300	6.0%	8.4%	0.4%	0.8%	0.4%	3.2%	1.5%	2.9%	11.3%
350	6.0%	8.8%	0.5%	0.2%	0.6%	2.3%	1.1%	1.6%	11.1%
400	6.0%	8.2%	0.6%	0.5%	0.2%	3.0%	1.6%	2.1%	10.9%
450	6.0%	8.4%	0.7%	0.9%	1.6%	1.1%	1.6%	1.8%	10.8%
500	6.0%	8.7%	1.1%	1.0%	0.4%	0.1%	1.5%	2.2%	11.0%
550	6.0%	8.0%	0.8%	0.9%	1.1%	1.2%	0.8%	2.6%	10.5%
600	6.0%	8.4%	0.8%	1.9%	1.8%	4.6%	2.1%	1.7%	12.0%
650	6.0%	8.5%	4.9%	2.9%	1.4%	8.8%	2.2%	2.9%	15.3%
700	6.0%	7.7%	3.1%	4.9%	2.2%	12.0%	2.5%	3.6%	17.2%
750	6.0%	8.1%	4.1%	6.2%	4.6%	11.8%	3.0%	6.3%	19.2%
800	6.0%	8.5%	5.5%	5.2%	2.5%	11.2%	3.0%	6.8%	18.7%

Table 6.2: Systematic uncertainty in α as a function of Z' mass for Central-Plug.

mass (GeV/c^2)	Lum.	Effi.	CEM resolution	CEM Scale	QCD shape	QCD normalize	Total
200	6.0%	4.9%	2.0%	2.3%	1.4%	1.8%	8.6%
250	6.0%	4.7%	3.1%	3.7%	0.6%	1.5%	9.1%
300	6.0%	4.9%	1.0%	3.6%	0.3%	1.1%	8.6%
350	6.0%	4.9%	1.9%	2.9%	0.4%	0.7%	8.5%
400	6.0%	4.6%	1.7%	2.9%	0.2%	0.6%	8.3%
450	6.0%	4.1%	3.0%	3.5%	0.5%	0.4%	8.6%
500	6.0%	4.8%	1.7%	0.9%	0.5%	1.1%	8.0%
550	6.0%	4.9%	0.7%	2.1%	0.2%	0.5%	8.0%
600	6.0%	4.3%	0.9%	1.3%	0.4%	1.3%	7.6%
650	6.0%	4.6%	1.3%	0.4%	0.0%	0.6%	7.7%
700	6.0%	4.9%	0.6%	1.1%	0.1%	1.4%	8.0%
750	6.0%	4.7%	0.5%	2.1%	0.7%	1.0%	8.0%
800	6.0%	4.7%	0.8%	1.7%	0.6%	1.5%	8.0%

Table 6.3: Systematic uncertainty in α as a function of Randall-Sundrum graviton mass for Central-Central.

mass (GeV/c^2)	Lum.	Effi.	CEM resolution	CEM Scale	PEM resolution	PEM Scale	QCD shape	QCD normalize	Total
200	6.0%	8.4%	0.5%	1.0%	0.4%	5.8%	2.0%	5.5%	13.3%
250	6.0%	7.9%	1.6%	1.0%	0.3%	5.2%	1.8%	3.5%	12.0%
300	6.0%	8.6%	1.5%	1.2%	0.6%	6.5%	0.9%	3.1%	12.9%
350	6.0%	7.7%	0.5%	1.2%	0.1%	2.9%	1.6%	2.8%	10.8%
400	6.0%	8.2%	0.0%	0.6%	0.2%	3.0%	2.1%	1.9%	11.0%
450	6.0%	7.6%	0.8%	0.8%	0.2%	2.1%	0.9%	1.5%	10.1%
500	6.0%	8.2%	1.9%	1.8%	0.1%	2.1%	1.7%	1.8%	11.0%
550	6.0%	8.1%	1.7%	2.4%	0.6%	4.9%	2.0%	2.6%	12.0%
600	6.0%	7.9%	2.6%	1.3%	2.5%	6.4%	1.2%	4.1%	13.1%
650	6.0%	9.1%	5.9%	3.2%	3.3%	7.3%	2.0%	5.2%	16.1%
700	6.0%	7.9%	8.3%	7.2%	4.2%	9.4%	3.2%	5.0%	19.0%
750	6.0%	8.0%	7.6%	6.7%	3.4%	14.2%	2.6%	8.0%	22.0%
800	6.0%	8.4%	12.4%	13.8%	8.0%	18.1%	4.5%	10.9%	31.3%

Table 6.4: Systematic uncertainty in α as a function of Randall-Sundrum graviton mass for Central-Plug.

mass (GeV/c^2)	Lum.	Effi.	CEM resolution	CEM Scale	QCD shape	QCD normalize	Total
200	6.0%	4.4%	2.7%	4.4%	0.6%	1.2%	9.2%
250	6.0%	5.0%	2.7%	3.4%	0.5%	0.8%	9.0%
300	6.0%	4.8%	1.5%	4.5%	0.4%	0.9%	9.1%
350	6.0%	4.4%	0.8%	2.4%	0.0%	0.7%	7.9%
400	6.0%	5.0%	1.6%	3.4%	0.3%	0.5%	8.7%
450	6.0%	4.2%	0.9%	3.1%	0.0%	0.1%	8.0%
500	6.0%	4.4%	2.4%	4.5%	0.0%	0.8%	9.1%
550	6.0%	5.2%	0.3%	3.9%	0.0%	0.4%	8.9%
600	6.0%	4.4%	1.1%	3.4%	0.3%	0.2%	8.2%
650	6.0%	4.8%	1.8%	2.8%	0.3%	0.9%	8.4%
700	6.0%	4.9%	2.6%	3.4%	0.3%	0.5%	8.9%
750	6.0%	4.7%	1.1%	3.9%	0.1%	0.5%	8.6%
800	6.0%	4.7%	0.1%	1.1%	0.7%	0.3%	7.7%

Table 6.5: Systematic uncertainty in α as a function of sneutrino mass for Central-Central.

mass (GeV/c^2)	Lum.	Effi.	CEM resolution	CEM Scale	PEM resolution	PEM Scale	QCD shape	QCD normalize	Total
200	6.0%	8.3%	0.0%	1.4%	0.5%	5.1%	1.4%	3.4%	12.1%
250	6.0%	8.2%	0.4%	1.0%	0.3%	4.9%	1.8%	1.7%	11.6%
300	6.0%	8.2%	0.3%	0.4%	0.5%	4.0%	1.4%	1.8%	11.2%
350	6.0%	8.2%	0.6%	1.3%	0.0%	4.2%	1.0%	1.2%	11.2%
400	6.0%	8.4%	1.7%	1.2%	0.5%	1.4%	2.3%	1.3%	11.0%
450	6.0%	8.2%	0.6%	0.5%	0.3%	0.8%	0.4%	0.5%	10.2%
500	6.0%	8.7%	0.8%	0.9%	0.6%	0.7%	0.9%	0.5%	10.7%
550	6.0%	8.0%	1.4%	2.5%	1.9%	3.4%	0.1%	1.2%	11.2%
600	6.0%	8.6%	2.0%	1.7%	0.2%	1.6%	0.0%	0.4%	11.0%
650	6.0%	8.8%	1.7%	2.0%	0.7%	3.4%	0.2%	0.1%	11.5%
700	6.0%	8.1%	1.6%	1.2%	1.0%	2.1%	0.6%	0.5%	10.6%
750	6.0%	8.7%	5.7%	3.7%	3.1%	7.4%	0.1%	0.8%	14.9%
800	6.0%	7.5%	9.0%	7.0%	3.6%	9.5%	1.0%	1.4%	18.1%

Table 6.6: Systematic uncertainty in α as a function of sneutrino mass for Central-Plug.

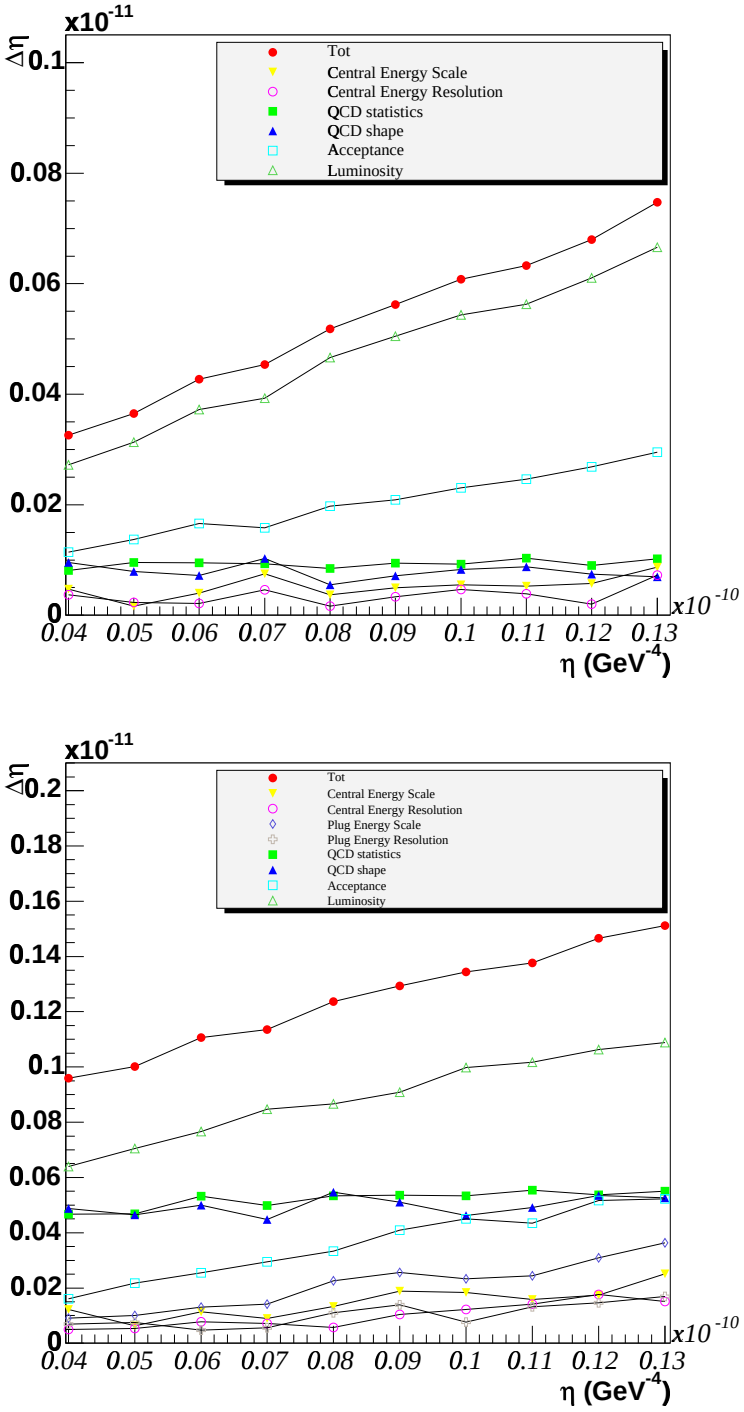

Figure 6.5: Systematic uncertainty in η as a function of η of of LED ($\lambda < 0$) for Central-Central (top) and Central-Plug (bottom).

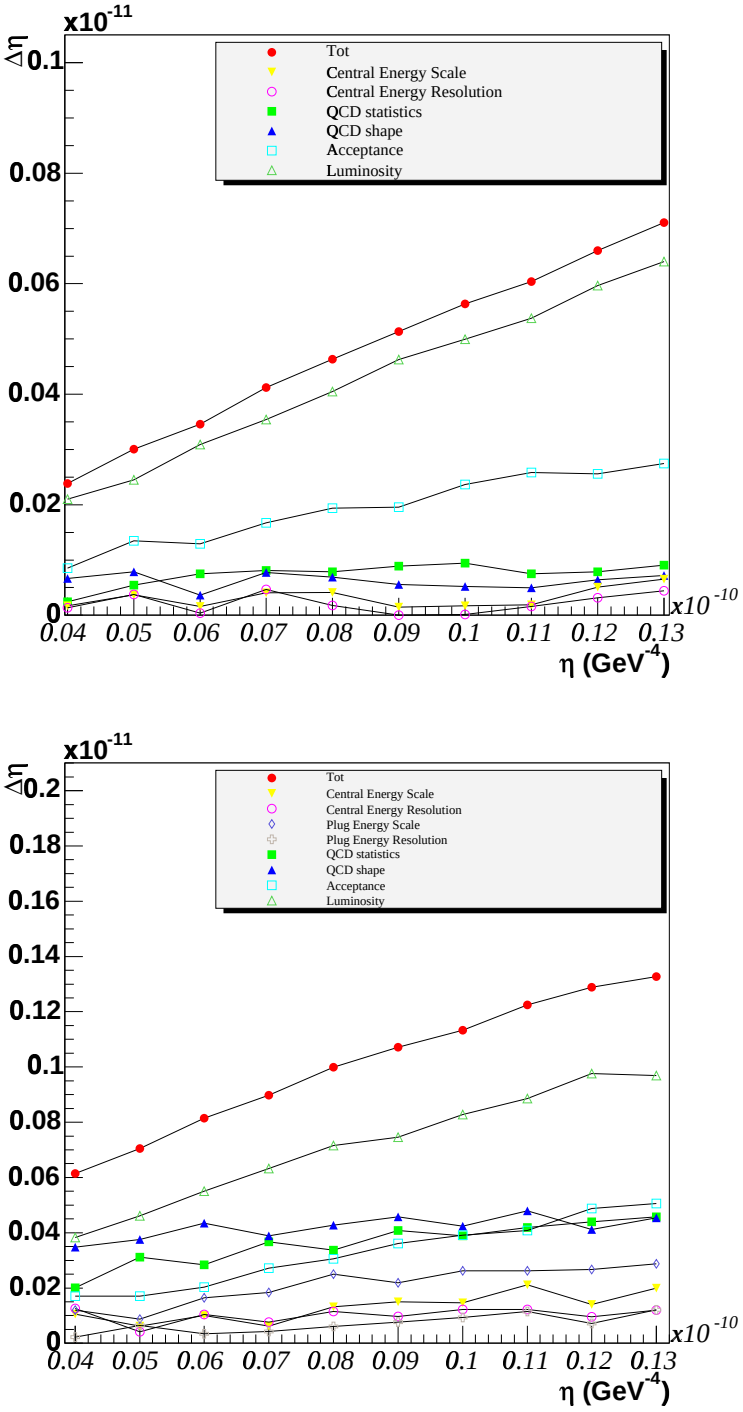

Figure 6.6: Systematic uncertainty in η as a function of η of of LED ($\lambda > 0$) for Central-Central (top) and Central-Plug (bottom).

Gaussian replaced points of the unsmeared likelihood function, L_{smear},

$$L_{smear}(\alpha) = \int_0^\infty L(\alpha^{'}) \frac{e^{-\frac{(\alpha-\alpha^{'})^2}{2\Delta\alpha^{'2}}}}{\sqrt{2\pi\Delta\alpha^{'2}}} d\alpha^{'} \tag{6.14}$$

or

$$L_{smear}(\eta) = \int_0^\infty L(\eta^{'}) \frac{e^{-\frac{(\eta-\eta^{'})^2}{2\Delta\eta^{'2}}}}{\sqrt{2\pi\Delta\eta^{'2}}} d\eta^{'} \tag{6.15}$$

To combine likelihoods of Central-Central (L_{CC}) and Central-Plug (L_{CP}), we can simply multiply the likelihood functions together to produce the combined likelihood. The only compilation arises in that there are common sources of systematic uncertainty and therefore correlated uncertainties between the samples. These sources are the Central energy scale and resolution, the error on acceptances due to PDF choice, the error on luminosity and the systematic error of event vertex fiduciality on the total efficiency.

We account for the correlated systematics. The full systematic uncertainty, $\Delta\alpha(\eta)$ is broken into two pieces, $\Delta\alpha(\eta)^{uncorr}$ and $\Delta\alpha(\eta)^{corr}$. We throw three normalized Gaussian numbers, x_1, x_2 and x_3, then we construct the smeared values $\alpha^{'}$ and $\eta^{'}$ as follows :

$$\alpha^{'}_{CC} = \alpha_{CC} + x_1\Delta\alpha^{corr}_{CC} + x_2\Delta\alpha^{uncorr}_{CC} \tag{6.16}$$

$$\alpha^{'}_{CP} = \alpha_{CP} + x_1\Delta\alpha^{corr}_{CP} + x_3\Delta\alpha^{uncorr}_{CP} \tag{6.17}$$

and

$$\eta^{'}_{CC} = \eta_{CC} + x_1\Delta\eta^{corr}_{CC} + x_2\Delta\eta^{uncorr}_{CC} \tag{6.18}$$

$$\eta^{'}_{CP} = \eta_{CP} + x_1\Delta\eta^{corr}_{CP} + x_3\Delta\eta^{uncorr}_{CP} \tag{6.19}$$

In this way, we can smear the correlated systematics in the same direction. We obtain the final smeared likelihood function by multiplying two smeared likelihood functions together.

6.3 Limits on $Z^{'}$

Cross section limits on $\sigma \cdot Br(Z^{'} \rightarrow e^+e^-)$ as a function of the $Z^{'}$ mass is shown in Figure 6.7. The top solid lines are the predicted $\sigma \cdot Br(Z^{'} \rightarrow e^+e^-)$ for various $Z^{'}$ models. The interaction of the predicted curve and 95% C.L. limit curve determines the 95% C.L. lower limit on the $Z^{'}$ mass. To get the predicted cross section, we use PYTHIA 6.203 with CTEQ5L parton distribution function and an overall correction factor $K_f = 1.3$. We also derive 95% C.L. limits on the mass of $Z^{'}$ for several E_6 models. Table 6.7 shows $Z^{'}$ mass limits from Central-Central,

CDF Run II Preliminary (200 pb^{-1})

	Central-Central (GeV)	Central-Plug (GeV)	Combined (GeV)
SM	720	625	750
η	625	550	650
ψ	590	530	625
χ	570	520	610
I	520	480	570

Table 6.7: Z' limits from Central-Central, Central-Plug and combined two samples.

Central-Plug and combined two samples. Table 6.8 shows the history of Z' search at CDF in dielectron mode. Our result becomes the best limit in the world from the direct searches.

We also set limits on Little Higgs model Z_H mass. Limit curve from Z' is directly applicable to Little Higgs model Z_H. Figure 6.8 shows the results. The cross section limit curve is exactly same as in Figure 6.7. Table 6.9 shows Little Higgs model Z_H mass limits from Central-Central, Central-Plug and combined two samples for .

We also study statistical consideration for the Z' limit using pseudo-experiment to check the reliability of the results. We repeat the experiment helped by the pseudo-experiment 1000 times. The value of each bin of the pseudo-experiment is chosen randomly from Poisson distribution which has the mean value of the expected background. We fit new data to a combination of the signal plus background and obtain 95% C.L. upper limit. The systematic uncertainties are not taken into account in this study. Figure 6.10 shows the result of our study for Z' limit. The points of expected limits show 95% C.L. upper limit values corresponding to the mean value from 1K times pseudo-experiment. 1σ and 2σ bands around the mean values are also shown. The limits we observed lie within the expected region from our statistical consideration.

6.4 Limits on Technicolor Particles

We compare the theoretical prediction of $\sigma(\rho_T) \cdot Br(\rho_T \to e^+e^-)$ and $\sigma(\omega_T) \cdot Br(\omega_T \to e^+e^-)$ with the cross section limit obtained for the Z' search. Since the width of ρ_T and ω_T resonances is expected to be very narrow and the angular distribution of dielectrons from ρ_T and ω_T would be the same as that from Z', the limit curve from the Z' analysis is directly applicable

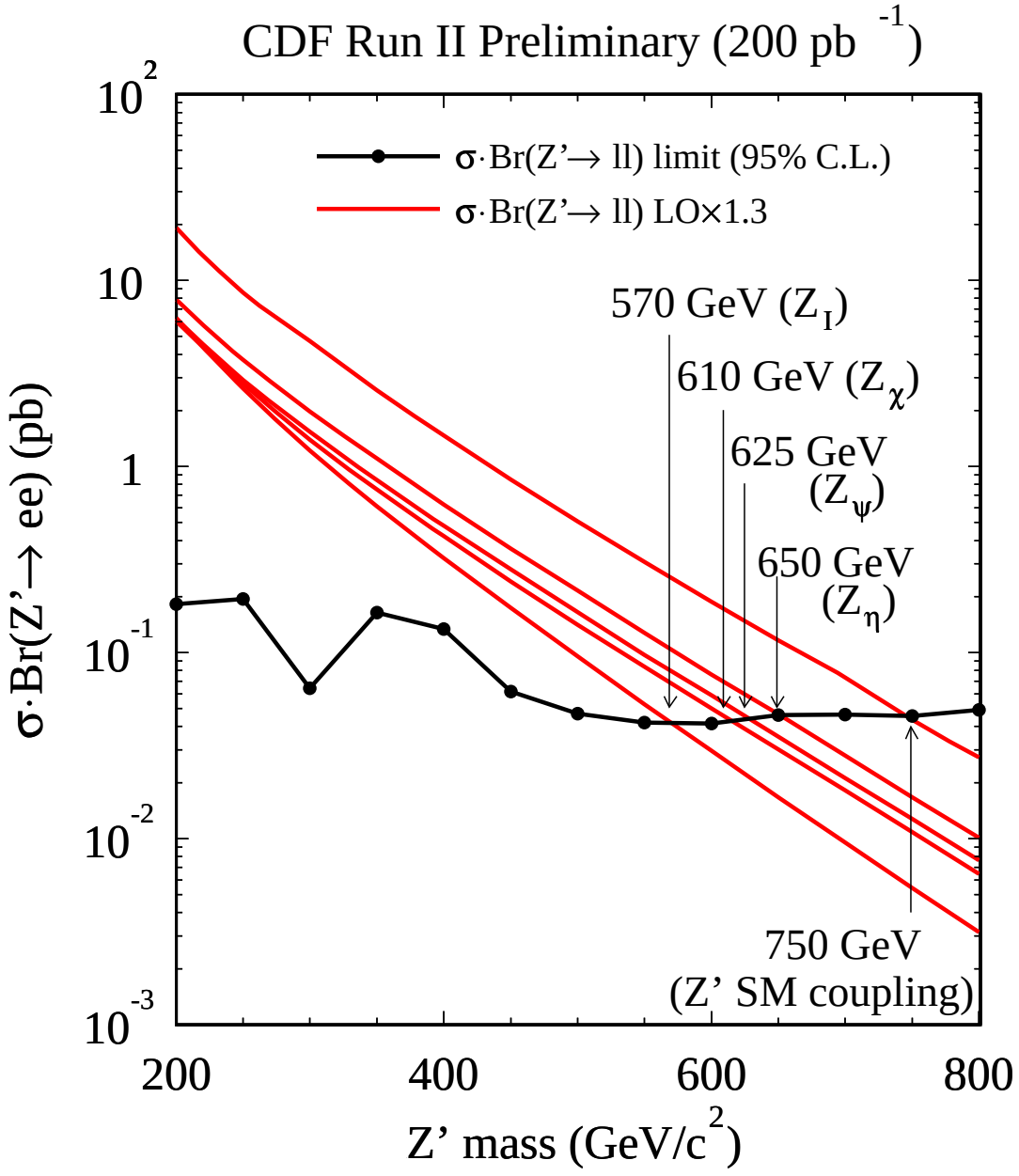

Figure 6.7: 95% confidence level limit on $\sigma \cdot Br(Z^{'} \rightarrow e^{+}e^{-})$ for 200 pb^{-1} of integrated luminosity as a function of $Z^{'}$ mass.

run	**Luminosity** (pb^{-1})	**Mass limit (95% C.L.)** (GeV/c^2)	$\sigma_{95\%} \cdot Br$ (pb)
Run0	4.05	387	1.31
RunIa	19.7	505	0.35
RunIb	90	640	0.06
RunII	10.4	460	0.75
RunII	72	650	0.1
RunII	126	720	0.06
RunII	200	750	0.04

Table 6.8: Summary of mass limits of Z'.

CDF Run II Preliminary (200 pb^{-1})

	Central-Central (GeV)	Central-Plug (GeV)	Combined (GeV)
$\cot\theta = 0.1$	775	670	800
$\cot\theta = 0.7$	700	610	730
$\cot\theta = 0.5$	620	550	650

Table 6.9: Little Higgs model Z_H limits from Central-Central, Central-Plug and combined two samples.

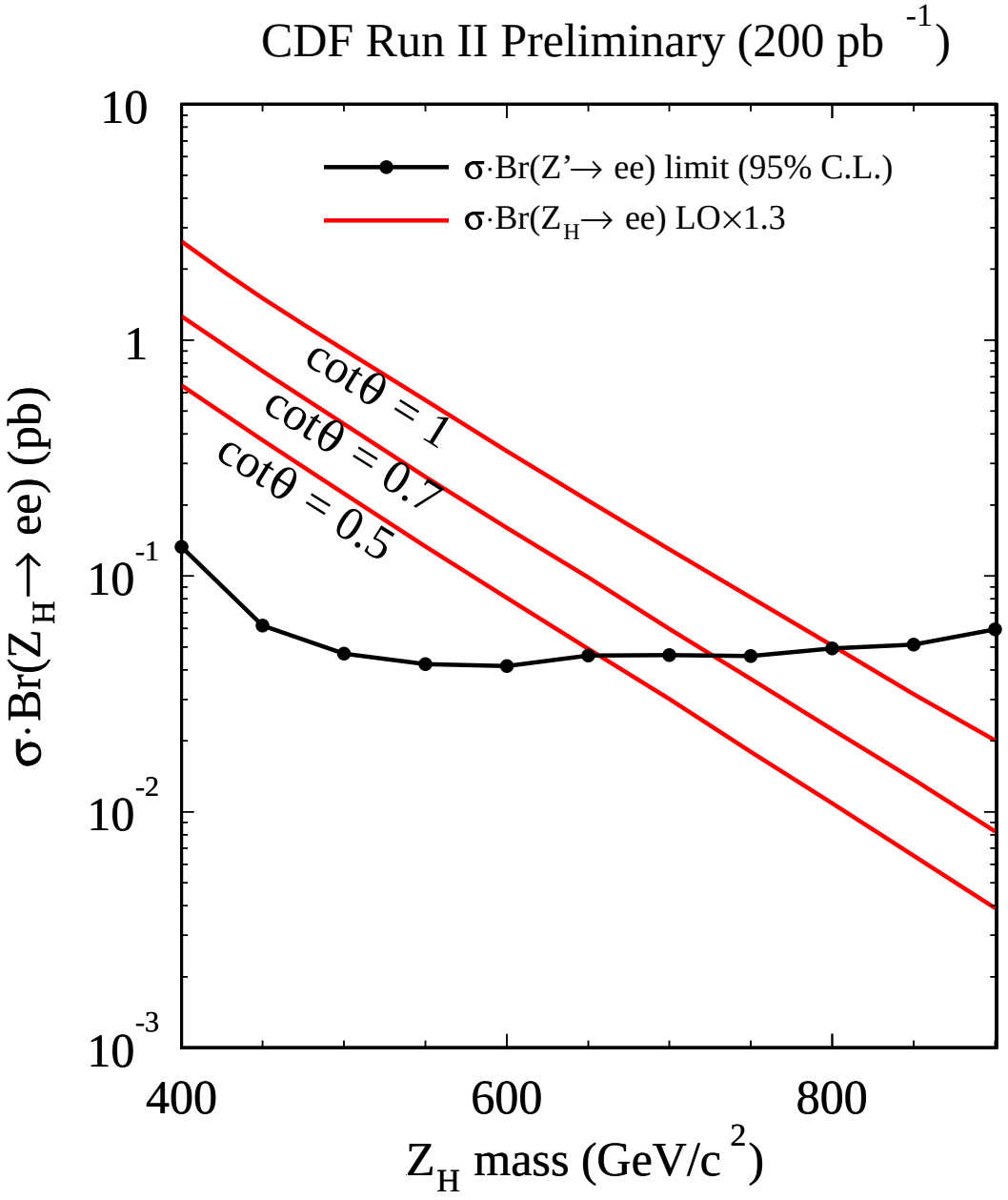

Figure 6.8: 95% confidence level limit on $\sigma \cdot Br(Z' \to e^+e^-)$ for 200 pb^{-1} of integrated luminosity as a function of Z_H mass for Little Higgs model Z_H.

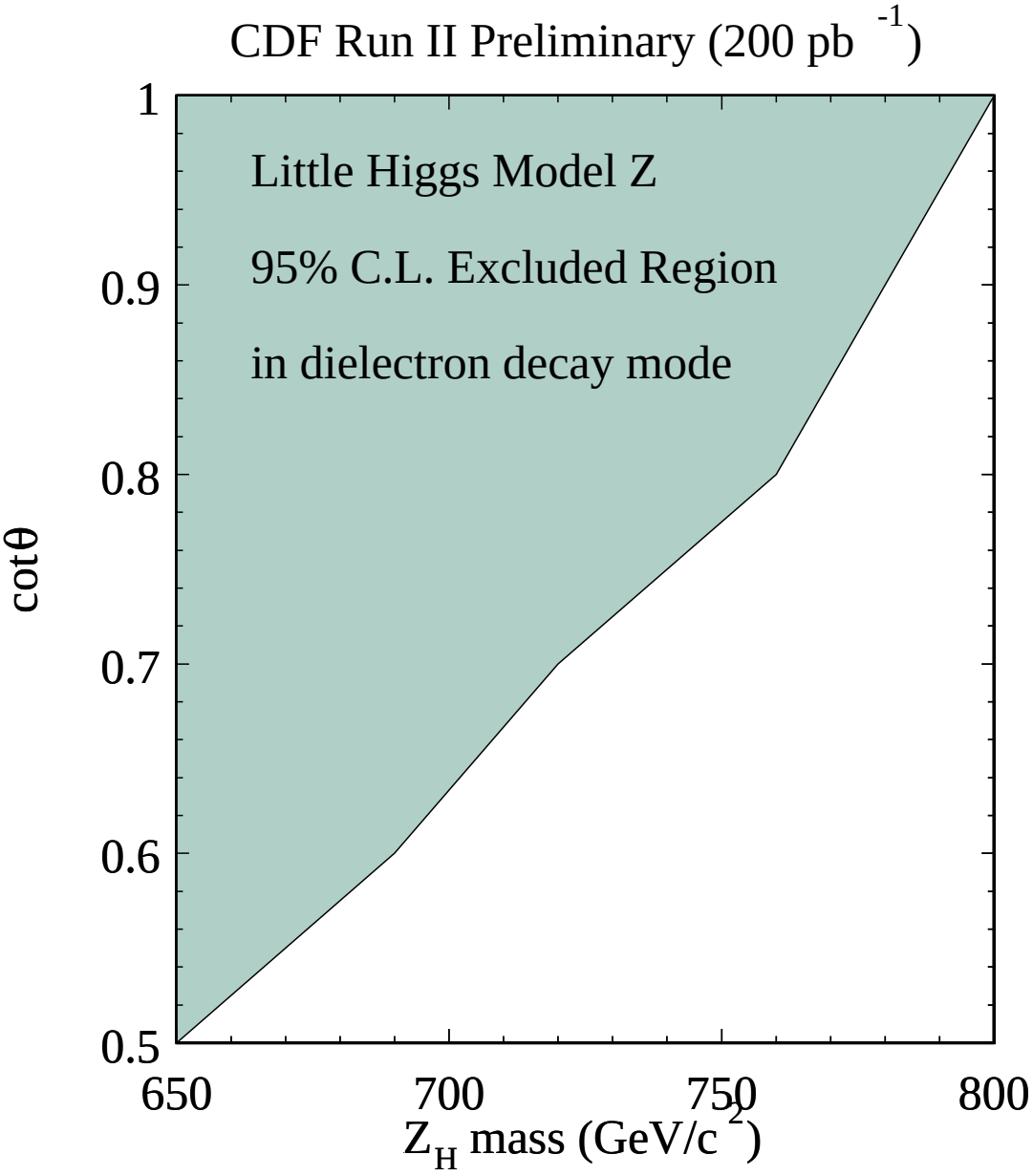

Figure 6.9: 95% confidence level exluded region on the plane for Little Higgs model Z_H mass vs. $\cot\theta$.

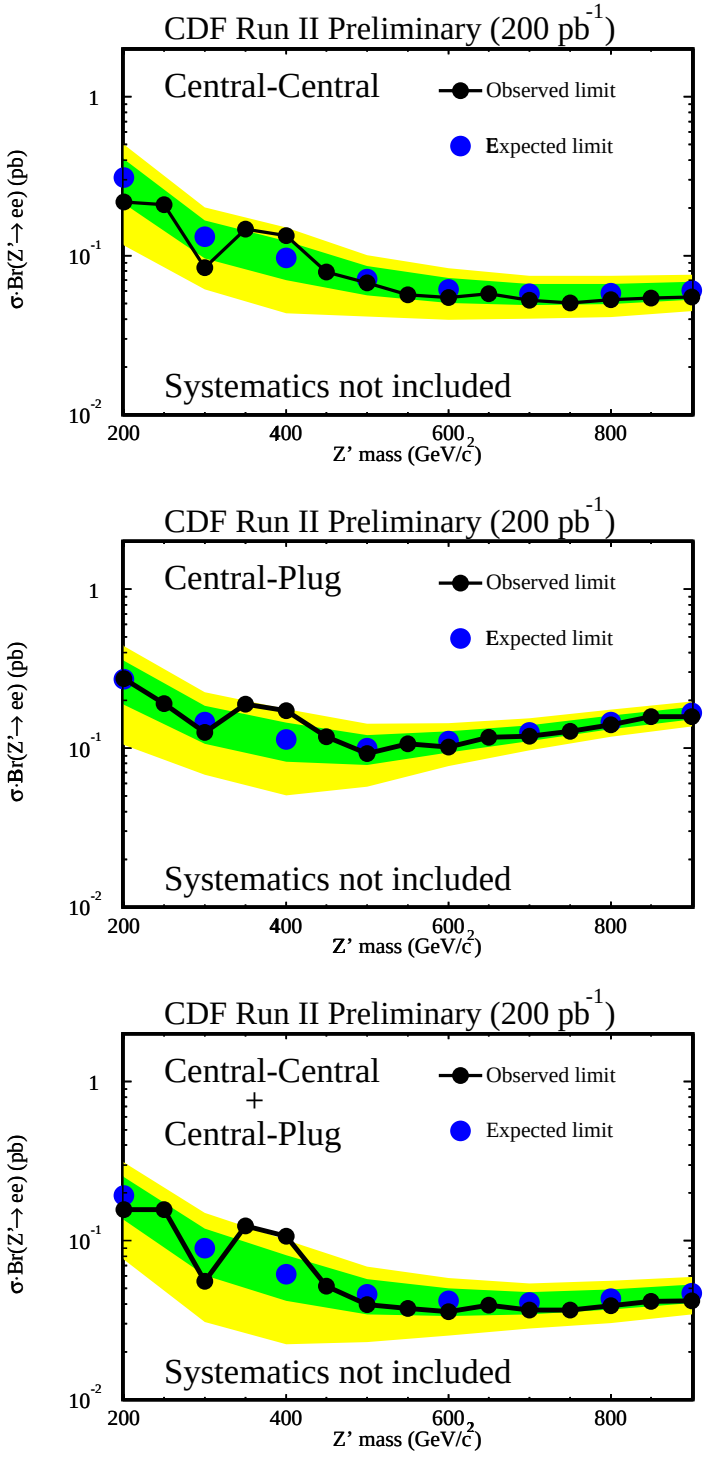

Figure 6.10: 95% confidence level upper limit obtained from the pseudo-experiment for cnetral-central, cnteral-plug and combined for $Z^{'}$ bosons.

to this technicolor search. Figure 6.11 shows the results. The predicted products of cross section and branching ratio for the process $\bar{p}p \to \rho_T, \omega_T \to e^+e^-$ depend on the mass difference between the vector mesons (ρ_T, ω_T) and the technipions (π_T). We set this mass difference to be 100 GeV ($M_{\rho_T} = M_{\omega_T} = M_{\pi_T} + 100$ GeV). The ω_T production cross section is sensitive to the charges of the technifermions (taken to be $Q_U = Q_D - 1 = 4/3$), as well as to a mass parameter M_T that controls the rate for $\omega_T \to \gamma + \pi_T^0$. The value of this parameter is unknown. Two parameters, M_A for axial-vector and M_V for vector couplings appear and their values are comparable. We set $M_A = M_V = M_T$. Ref. [49] suggests a value of several hundred GeV. We set this parameter to be 200 GeV $< M_T <$ 400 GeV. To get the predicted cross section for the processes $\bar{p}p \to \rho_T \to e^+e^-$ and $\bar{p}p \to \omega_T \to e^+e^-$, we use PYTHIA 6.203 with CTEQ5L parton distribution function and an overall correction factor $K_f = 1.3$.

6.5 Limits on Randall-Sundrum Graviton

The 95% C.L. limit on $\sigma \cdot Br(G \to e^+e^-)$ is shown in Figure 6.12 as a function of the graviton mass and the 95% C.L. excluded region in the k/M_{Pl} and graviton mass plane. The top solid lines in the plot are the predictions of $\sigma \cdot Br(G \to e^+e^-)$. The interactions of the predicted curves and 95% C.L. limit curves determine the 95% C.L. lower limits on the graviton mass for each k/M_{Pl}. To get the predicted cross section, we use PYTHIA 6.203 with CTEQ5L parton distribution function and an overall correction factor $K_f = 1.3$. We consider the region $k/M_{Pl} < 0.1$. Table 6.10 shows Randall-Sundrum graviton mass limits from Central-Central, Central-Plug and combined two samples.

Figure 6.14 shows the result of pseudo-experiment to check the reliability of the results for Randall-Sundrum graviton limit. The points of expected limits show 95% C.L. upper limit values corresponding to the mean value from 1K times pseudo-experiment. 1σ and 2σ bands around the mean values are also shown. The systematic uncertainties are not taken into account in this study. The limits we observed lie within the expected region from our statistical consideration.

6.6 Limits on RPV Sneutrino

The 95% C.L. limit on $\sigma \cdot Br(\tilde{\nu} \to e^+e^-)$ is shown in Figure 6.15 as a function of the sneutrino mass for the various $\lambda'^2 \cdot Br$ and the 95% C.L. excluded region in the $\lambda'^2 \cdot Br$ and sneutrino mass plane. The top solid lines in the plot are the predictions of $\sigma \cdot Br(\tilde{\nu} \to e^+e^-)$. The interactions

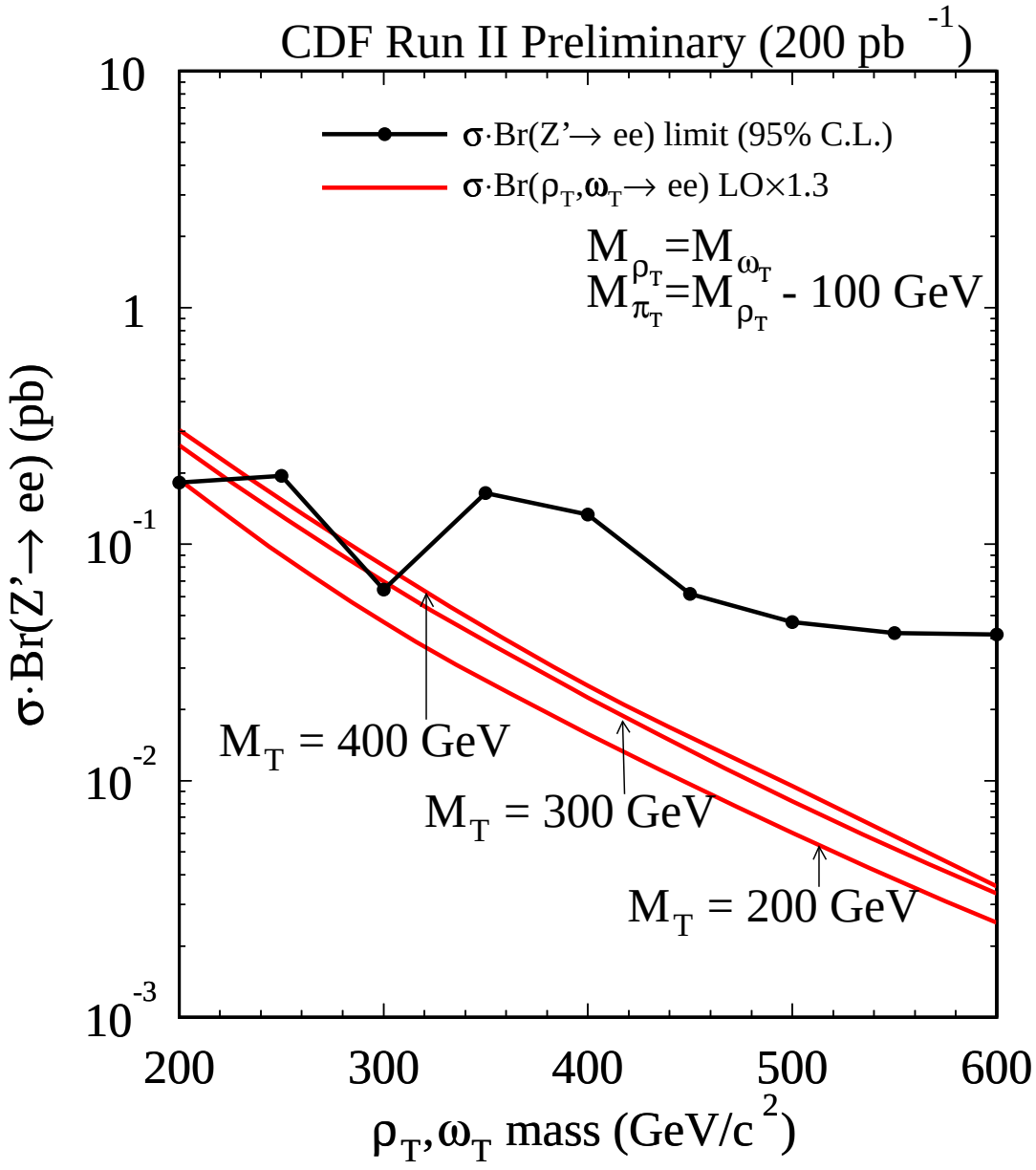

Figure 6.11: 95% confidence level limit on $\sigma \cdot Br(Z' \to e^+e^-)$ for 200 pb^{-1} of integrated luminosity as a function of ρ_T and ω_T mass.

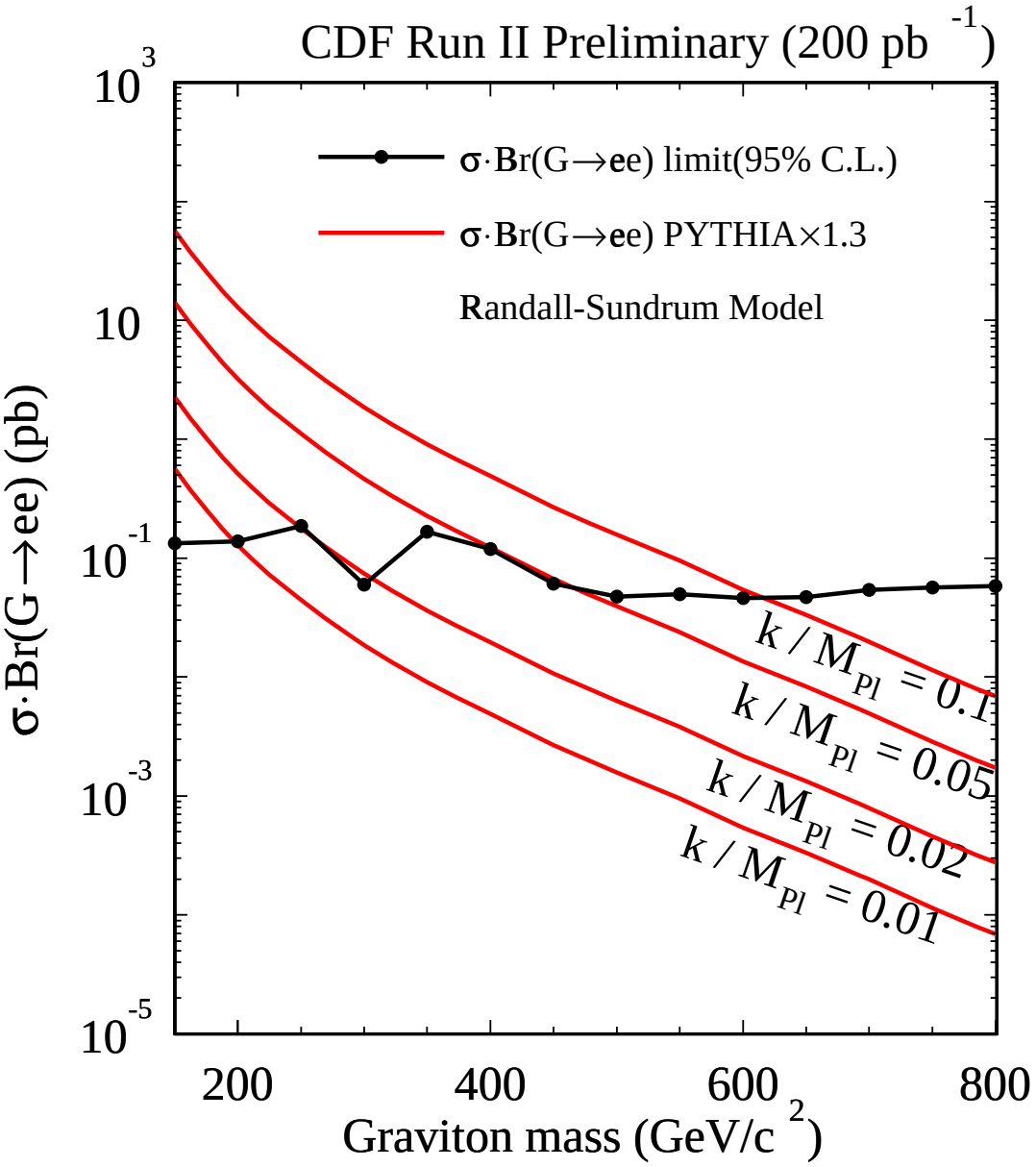

Figure 6.12: 95% confidence level limits on $\sigma \cdot Br(G \rightarrow e^+e^-)$ for 200 pb^{-1} of integrated luminosity as a function of graviton mass for different $k/\bar{M}_{Pl}$.

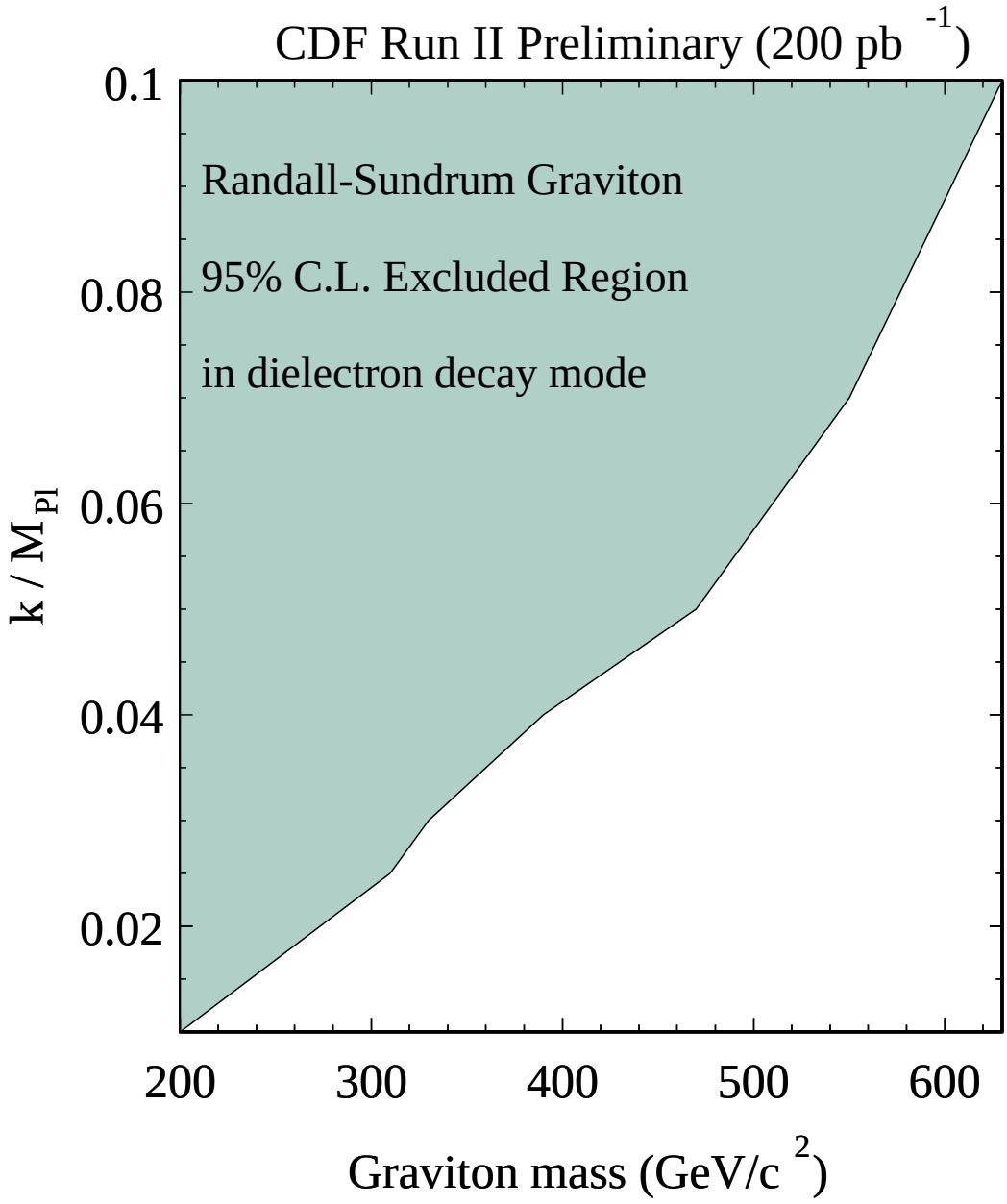

Figure 6.13: 95% confidence level exluded region on the plane for graviton mass vs. $k/\bar{M}_{Pl}$.

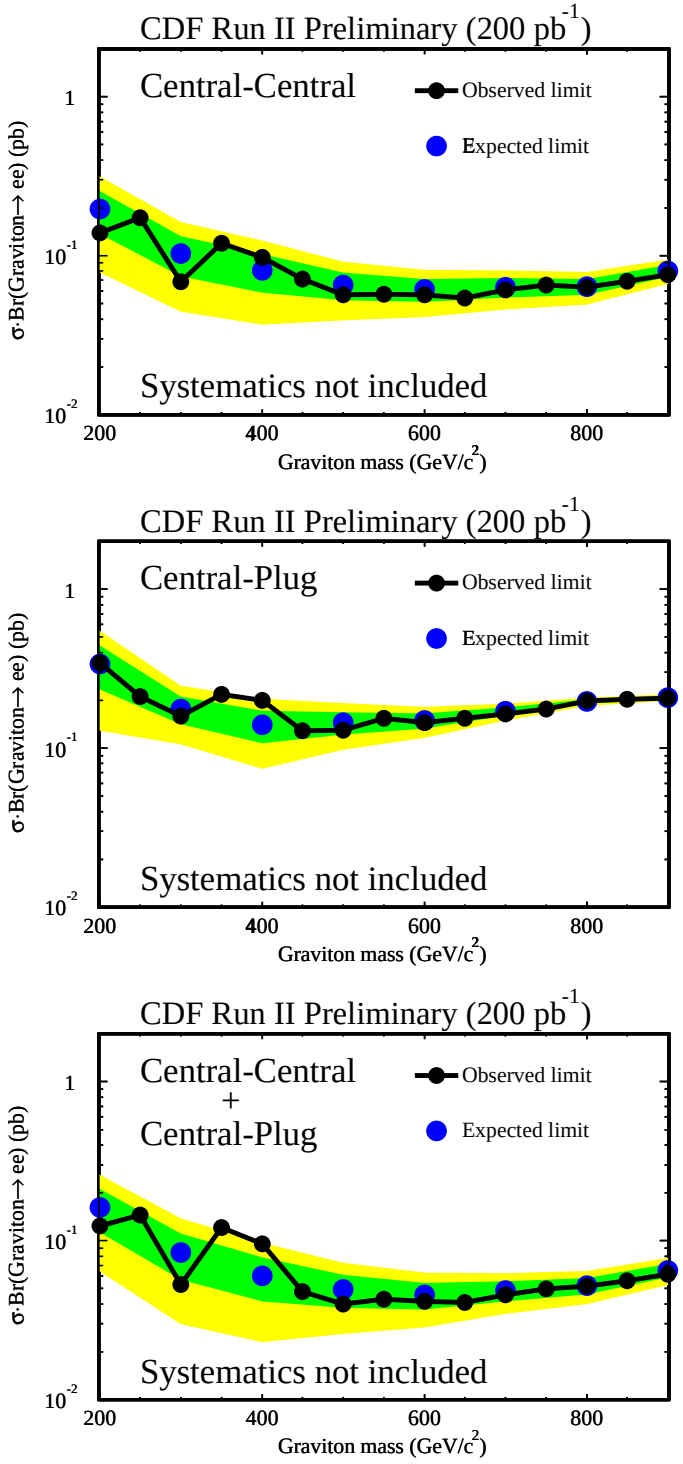

Figure 6.14: 95% confidence level upper limit obtained from the pseudo-experiment for cnetral-central, cnteral-plug and combined for Randall-Sundrum graviton.

CDF Run II Preliminary (200 pb^{-1})

	Central-Central (GeV)	Central-Plug (GeV)	Combined (GeV)
$k/M_{Pl} = 0.1$	590	490	620
$k/M_{Pl} = 0.05$	400	350	470
$k/M_{Pl} = 0.02$	300	220	310
$k/M_{Pl} = 0.01$	190	165	200

Table 6.10: Randall-Sundrum graviton mass limits from Central-Central, Central-Plug and combined two samples.

of the predicted curves and 95% C.L. limit curves determine the 95% C.L. lower limits on the sneutrino mass for each $\lambda'^2 \cdot Br$. Table 6.11 shows R-parity violating sneutrino mass limits from Central-Central, Central-Plug and combined two samples.

The predicted product of cross section and branching ratio for the process $\bar{p}p \to \tilde{\nu} \to e^+e^-$ depends on λ' from initial state vertex and slepton's branching fraction, Br :

$$\sigma \propto \lambda'^2 \times Br \tag{6.20}$$

Using this product, $\lambda'^2 \cdot Br$, we can set limits on sneutrino mass as a function of $\lambda'^2 \cdot Br$ [11]. The theoretical cross section shown in Figure 6.15 were obtained scaling NLO calculation by $\lambda'^2 \cdot Br$ [13]. Table 6.12 shows the LO and NLO calculation of RPV sneutrino production in $\bar{p}p$ collisions at $\sqrt{s} = 1.96$ TeV with CTEQ5 parton distribution function and $\lambda' = 0.01$.

Figure 6.17 shows the result of pseudo-experiment to check the reliability of the results for sneutrino limit. The points of expected limits show 95% C.L. upper limit values corresponding to the mean value from 1K times pseudo-experiment. 1σ and 2σ bands around the mean values are also shown. The systematic uncertainties are not taken into account in this study. The limits we observed lie within the expected region from our statistical consideration.

6.7 Limits on Effective Planck Scale

We also use the observed dielectron events with invariant mass to set 95% C.L. limits on effective Planck scale. Figure 6.18 and Figure 6.19 show the likelihood function of η for the fit to data for $\lambda < 0$ and $\lambda > 0$, respectively. Blue colored histograms in this figure represent the smeared likelihood function. From the combined likelihood of Central-Central and Central-Plug, the

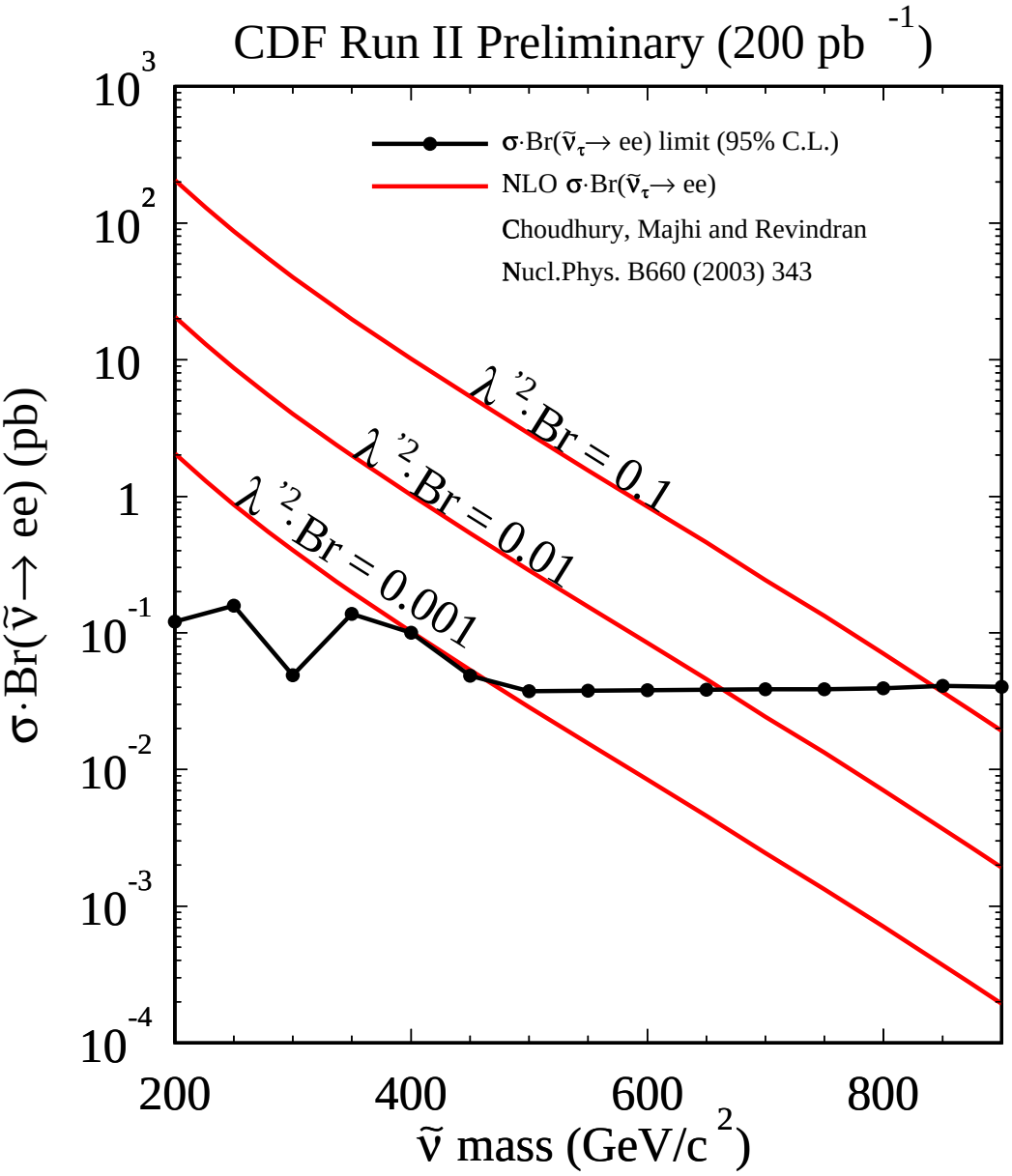

Figure 6.15: 95% confidence level limits on $\sigma \cdot Br(\tilde{\nu} \to e^+e^-)$ for 200 pb^{-1} of integrated luminosity as a function of sneutrino mass for different $\lambda'^2 \cdot Br$.

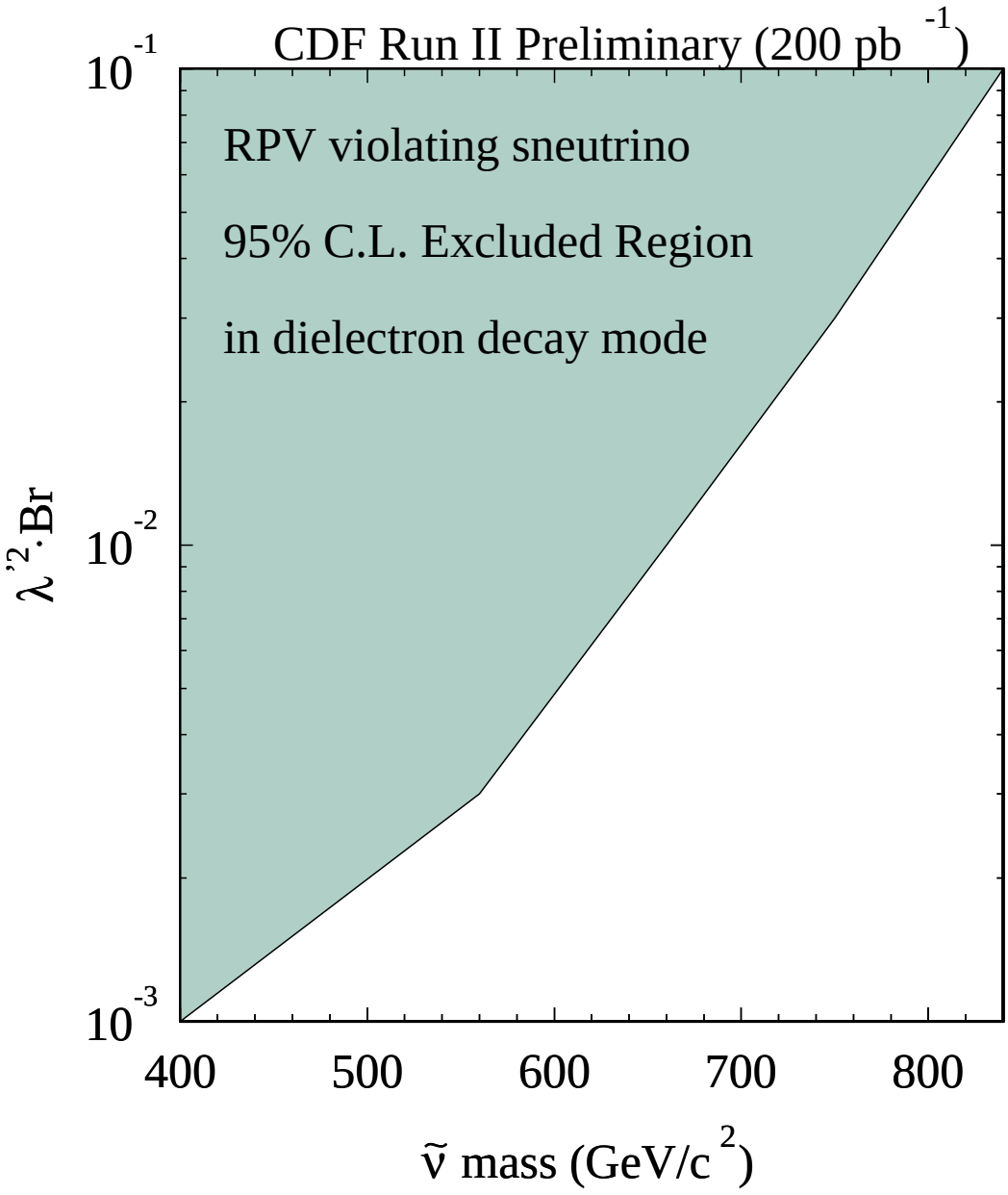

Figure 6.16: 95% confidence level exluded region on the plane for sneutrino mass vs. $\lambda'^2 \cdot Br$.

CDF Run II Preliminary (200 pb^{-1})

	Central-Central (GeV)	Central-Plug (GeV)	Combined (GeV)
$\lambda'^2 \cdot Br = 0.1$	830	710	840
$\lambda'^2 \cdot Br = 0.01$	650	550	660
$\lambda'^2 \cdot Br = 0.001$	400	340	400

Table 6.11: RPV sneutrino mass limits from Central-Central, Central-Plug and combined two samples.

Mass ($m_{\tilde{\nu}_i}$) (GeV)	Cross Section (pb)	
	LO	NLO
100	0.748	1.117
200	6.84×10^{-2}	0.103
300	1.36×10^{-2}	2.01×10^{-2}
400	3.54×10^{-3}	5.09×10^{-3}
500	1.04×10^{-3}	1.43×10^{-3}
600	3.17×10^{-4}	4.21×10^{-4}
700	9.72×10^{-5}	1.22×10^{-4}
800	2.91×10^{-5}	3.54×10^{-5}
900	8.25×10^{-6}	9.62×10^{-6}
1000	2.16×10^{-6}	2.41×10^{-6}

Table 6.12: LO and NLO calculation of sneutrino production in $\bar{p}p$ collisions at $\sqrt{s} = 1.96$ TeV with CTEQ5 parton distribution function and $\lambda' = 0.01$.

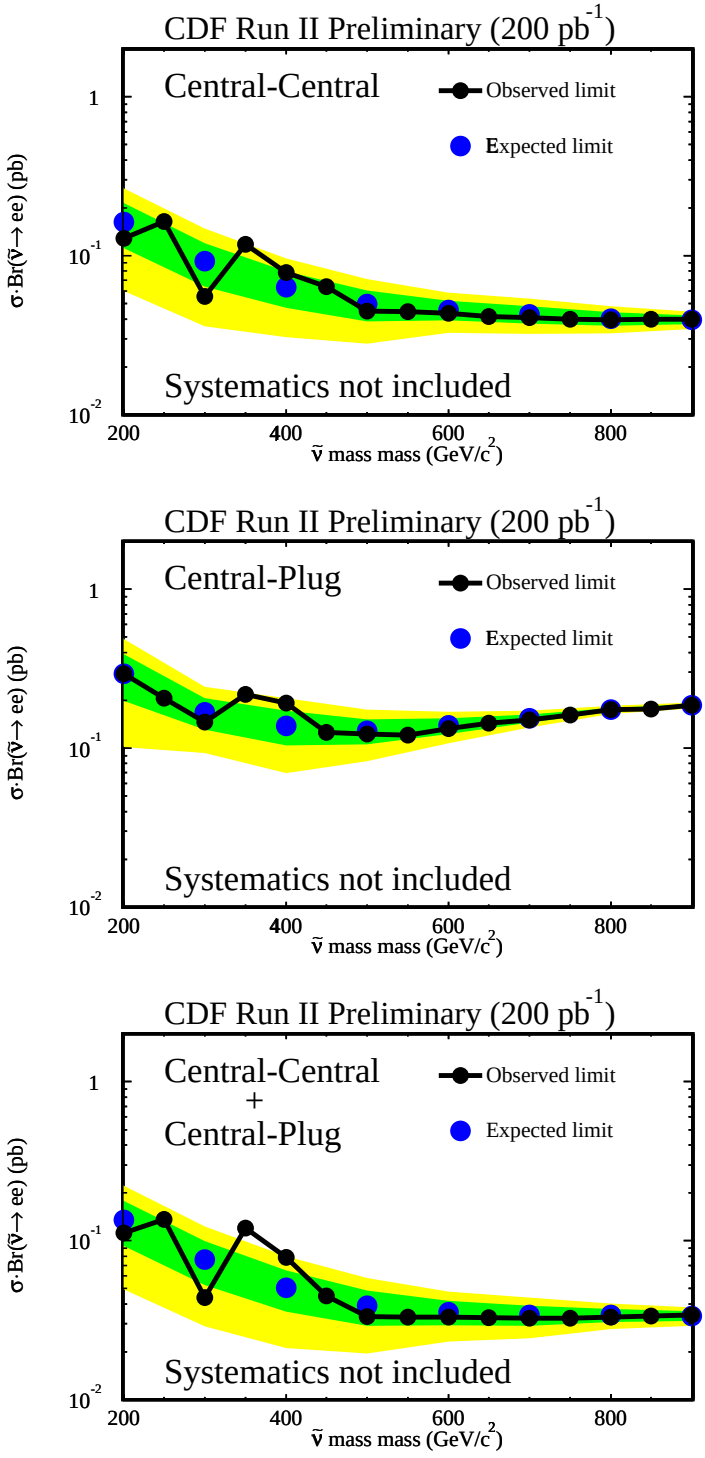

Figure 6.17: 95% confidence level upper limit obtained from the pseudo-experiment for cnetral-central, cnteral-plug and combined for sneutrino.

CDF Run II Preliminary (200 pb^{-1})

	η_{95} (10^{-12}GeV^{-4})		Hewett (GeV)		HLZ (GeV)					GRW (GeV)
	$\lambda < 0$	$\lambda > 0$	$\lambda < 0$	$\lambda > 0$	$n = 3$	$n = 4$	$n = 5$	$n = 6$	$n = 7$	
Central-Central	1.05	1.18	987	959	1315	1105	999	929	879	1105
Central-Plug	2.23	2.47	818	797	1089	916	827	770	728	916
Combined	1.05	1.18	987	959	1315	1105	999	929	879	1105

Table 6.13: Effective Planck scale limits from Central-Central and Central-Plug combined.

limits on η are 1.05×10^{-12} GeV^{-4} for $\lambda < 0$ and 1.17×10^{-12} GeV^{-4} for $\lambda > 0$. The 95% C.L. lower limirs on effective Planck scale are 987 GeV and 961 GeV for $\lambda = -1$ and $+1$ respectively in the Hewett convention when the LED K-factor is 1.0. Table 6.13 show the results in the other conventions of Han, Lykken and Zhang (HLZ) [20] and Giudice, Rattazzi and Wells (GRW) [21] for Central-Central, Central-Plug and combined. Definitions of λ conventions are $\frac{2}{\pi}\lambda_{Hewett} = F_{GRW} = F_{HLZ}$, $F_{GRW} = 1$ and $F_{HLZ} = \frac{2}{n-2}(n > 2)$.

Figure 6.20 and Figure 6.21 show the results of pseudo-experiment to check the reliability of the results for effective Planck scale limit. The histograms show the distributions of 95% C.L. lower limit values from 1K times pseudo-experiment. The arrows indicate the our observed limits. The systematic uncertainties are not taken into account in this study. The limits we observed lie within the expected region from our statistical consideration.

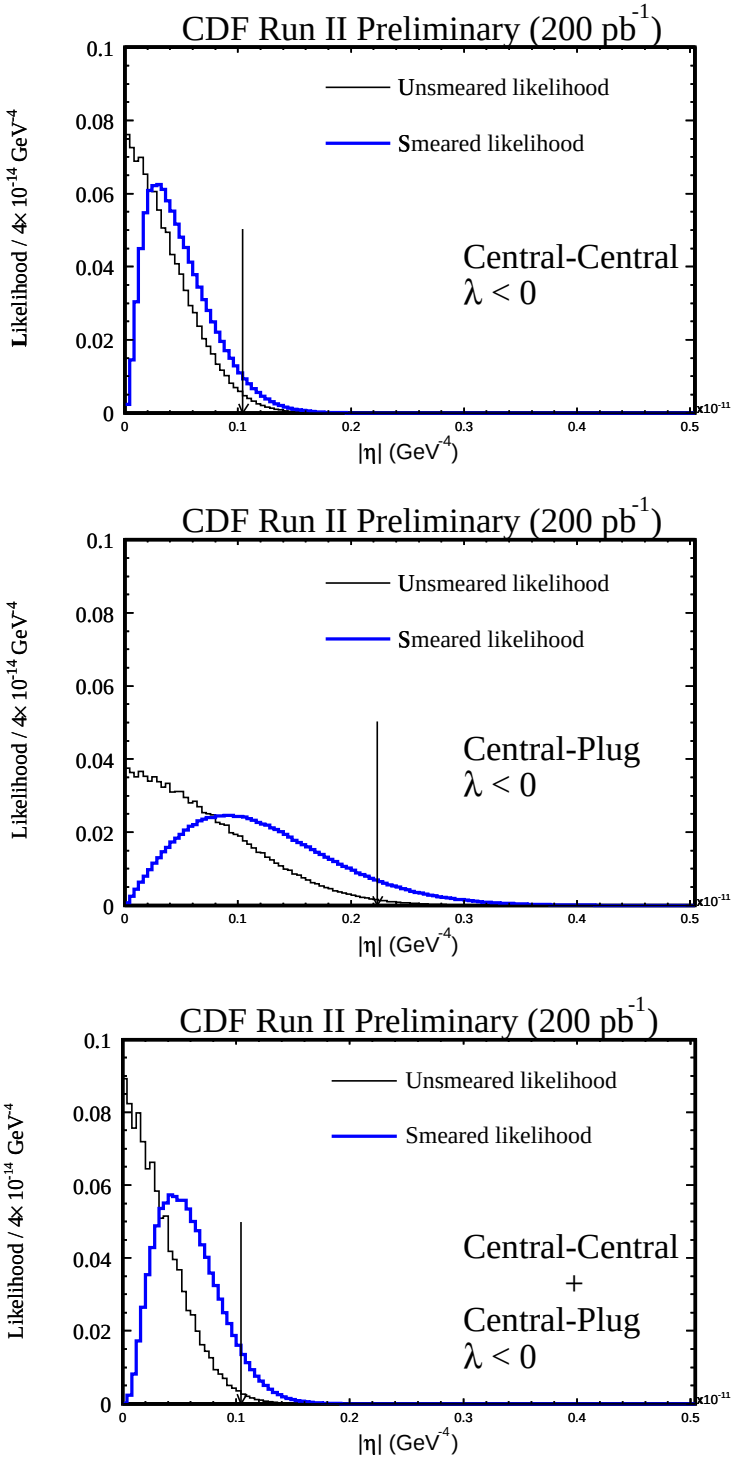

Figure 6.18: Likelihood functions for the fit to the data before and after smearing for $\lambda < 0$.

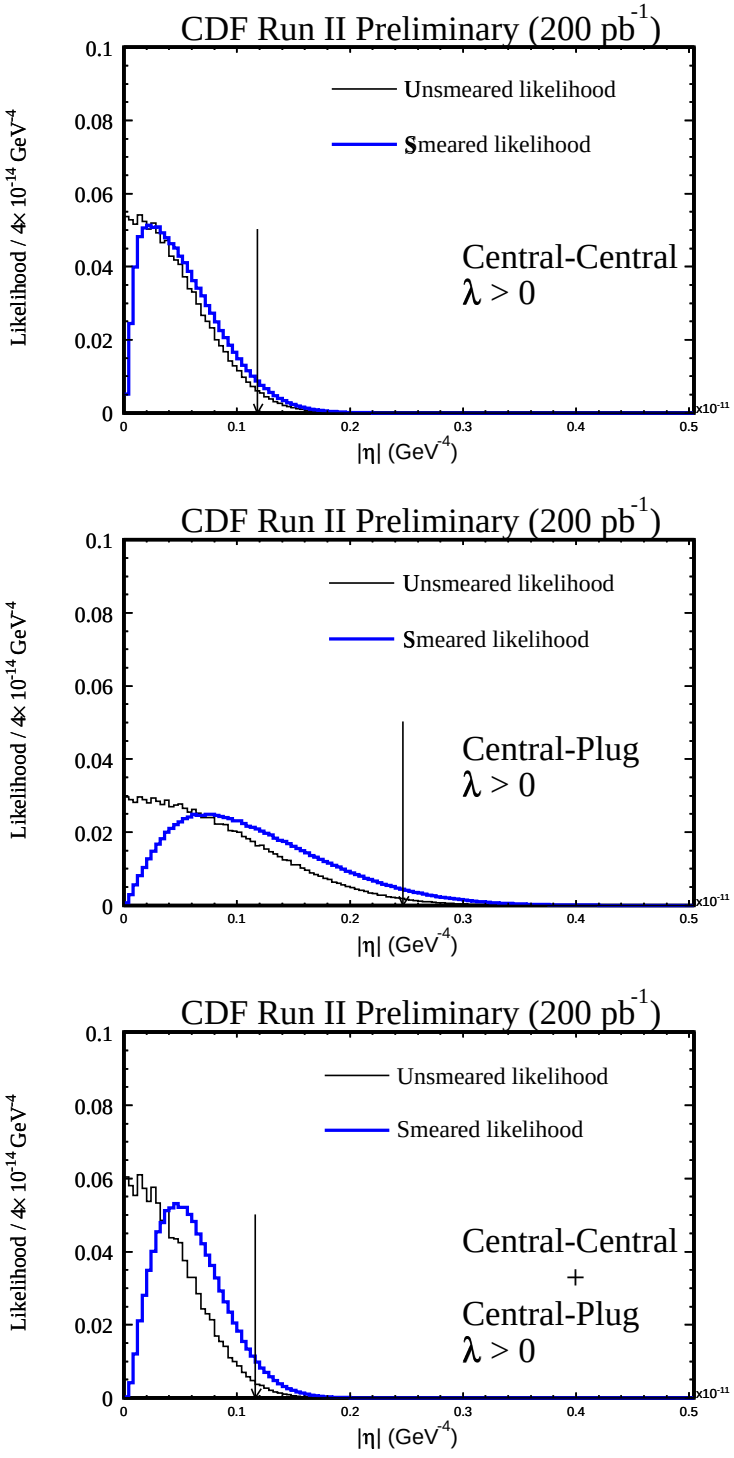

Figure 6.19: Likelihood functions for the fit to the data before and after smearing for $\lambda > 0$.

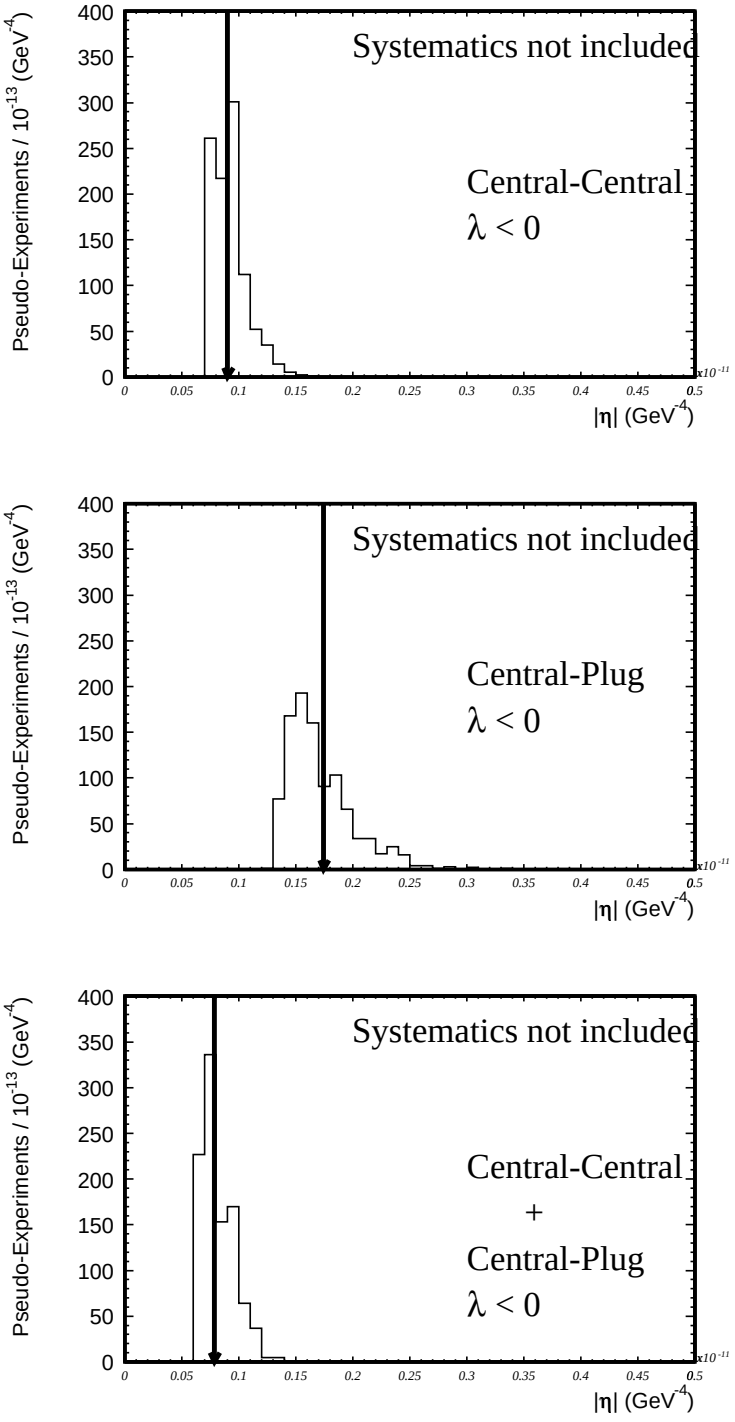

Figure 6.20: η_{95} for 1000 pseudo-experiments for $\lambda < 0$.

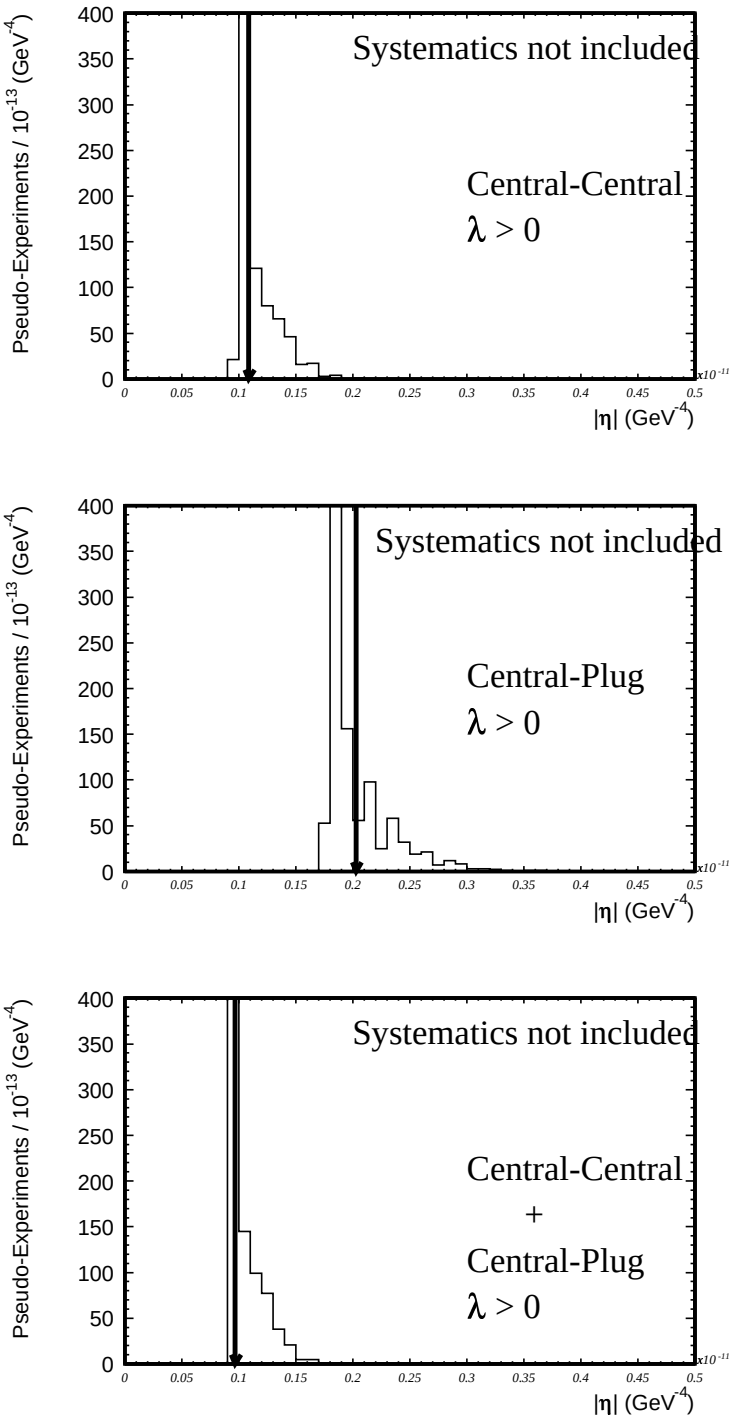

Figure 6.21: η_{95} for 1000 pseudo-experiments for $\lambda > 0$.

Chapter 7

Conclusions

We have performed search for new physics in the production of dielectrons at high energies using the data sample collected with the upgraded Collider Detector at Fermilab (CDF II) at the Tevatron $\bar{p}p$ collider, and correspond to an integrated luminosity of approximately 200 pb^{-1} at $\sqrt{s} = 1.96$ TeV , taken during the period March 2002 - September 2003. No evidence is found for new physics and we obtain 95% confidence level limits on the production cross section times branching ratio for resonant particles as a function of the dielectron invariant mass. We also set 95% confidence level lower limits on the effective Planck scale of large extra dimensions. Lower bounds on new particles' mass at 95% confidence level:

- $Z^{'}$ for Standard Model coupling :

$$M_{Z'} > 750 \text{ GeV}/c^2$$

- Little Higgs model Z_H for $\cot\theta = 0.1$:

$$M_{Z_H} > 800 \text{ GeV}/c^2$$

- Randall-Sundrum graviton for $k/M_{Pl} = 0.1$:

$$M_G > 620 \text{ GeV}/c^2$$

- R-parity violating sneutrino for $\lambda^{'2} \cdot Br = 0.1$:

$$M_{\tilde{\nu}} > 840 \text{ GeV}/c^2$$

- Effective Planck scale of large extra dimensions for Hewett convention :

$$M_s > 987 \text{ GeV}/c^2 (\text{for} \lambda < 0),$$

$$M_s > 961 \text{ GeV}/c^2 (\text{for} \lambda > 0)$$

are obtained. The results for little Higgs model Z_H and Randall-Sundrum graviton are the first experimental limits obtained from this analysis.

Bibliography

[1] N. Arkani-Hamed, S. Dimopoulos and G. R. Dvali, "The hierarchy problem and new dimensions at a millimeter," Phys. Lett. B **429**, 263 (1998) [arXiv:hep-ph/9803315].

[2] I. Antoniadis, N. Arkani-Hamed, S. Dimopoulos and G. R. Dvali, "New dimensions at a millimeter to a Fermi and superstrings at a TeV," Phys. Lett. B **436**, 257 (1998) [arXiv:hep-ph/9804398].

[3] N. Arkani-Hamed, S. Dimopoulos and G. R. Dvali, "Phenomenology, astrophysics and cosmology of theories with sub-millimeter dimensions and TeV scale quantum gravity," Phys. Rev. D **59**, 086004 (1999) [arXiv:hep-ph/9807344].

[4] L. Randall and R. Sundrum, "A large mass hierarchy from a small extra dimension," Phys. Rev. Lett. **83**, 3370 (1999) [arXiv:hep-ph/9905221].

[5] L. Randall and R. Sundrum, "An alternative to compactification," Phys. Rev. Lett. **83**, 4690 (1999) [arXiv:hep-th/9906064].

[6] N. Arkani-Hamed, A. G. Cohen and H. Georgi, "Anomalies on orbifolds," Phys. Lett. B **516**, 395 (2001) [arXiv:hep-th/0103135].

[7] N. Arkani-Hamed, A. G. Cohen and H. Georgi, "Twisted supersymmetry and the topology of theory space," JHEP **0207**, 020 (2002) [arXiv:hep-th/0109082].

[8] N. Arkani-Hamed, A. G. Cohen, T. Gregoire and J. G. Wacker, "Phenomenology of electroweak symmetry breaking from theory space," JHEP **0208**, 020 (2002) [arXiv:hep-ph/0202089].

[9] I. Low, W. Skiba and D. Smith, "Little Higgses from an antisymmetric condensate," Phys. Rev. D **66**, 072001 (2002) [arXiv:hep-ph/0207243].

[10] J. L. Hewett and T. G. Rizzo, "Low-Energy Phenomenology Of Superstring Inspired E(6) Models," Phys. Rept. **183**, 193 (1989).

[11] B. Allanach *et al.* [R parity Working Group Collaboration], "Searching for R-parity violation at Run-II of the Tevatron," arXiv:hep-ph/9906224.

[12] S. Lola, "Resonant single chargino and neutralino versus fermion antifermion production at the linear collider," arXiv:hep-ph/9912217.

[13] D. Choudhury, S. Majhi and V. Ravindran, "QCD corrections to resonant slepton production in hadron colliders," Nucl. Phys. B **660**, 343 (2003) [arXiv:hep-ph/0207247].

[14] J. Kalinowski, R. Ruckl, H. Spiesberger and P. M. Zerwas, "R-parity violating SUSY signals in lepton pair production at the Tevatron," Phys. Lett. B **414**, 297 (1997) [arXiv:hep-ph/9708272].

[15] [CDF Collaboration], "Search for lepton flavor violating decays of a heavy neutral particle in p Phys. Rev. Lett. **91**, 171602 (2003) [arXiv:hep-ex/0307012].

[16] K. D. Lane, "Technihadron production and decay rates in the technicolor straw man model," arXiv:hep-ph/9903372.

[17] K. Lane and S. Mrenna, "The collider phenomenology of technihadrons in the technicolor Straw Man Model," Phys. Rev. D **67**, 115011 (2003) [arXiv:hep-ph/0210299].

[18] J. L. Hewett, "Indirect collider signals for extra dimensions," Phys. Rev. Lett. **82**, 4765 (1999) [arXiv:hep-ph/9811356].

[19] A. K. Gupta, N. K. Mondal and S. Raychaudhuri, "Constraining large extra dimensions using dilepton data from the Tevatron collider," arXiv:hep-ph/9904234.

[20] T. Han, J. D. Lykken and R. J. Zhang, "On Kaluza-Klein states from large extra dimensions," Phys. Rev. D **59**, 105006 (1999) [arXiv:hep-ph/9811350].

[21] G. F. Giudice, R. Rattazzi and J. D. Wells, "Quantum gravity and extra dimensions at high-energy colliders," Nucl. Phys. B **544**, 3 (1999) [arXiv:hep-ph/9811291].

[22] H. Davoudiasl, J. L. Hewett and T. G. Rizzo, "Experimental probes of localized gravity: On and off the wall," Phys. Rev. D **63**, 075004 (2001) [arXiv:hep-ph/0006041].

[23] J. Bijnens, P. Eerola, M. Maul, A. Mansson and T. Sjostrand, "QCD signatures of narrow graviton resonances in hadron colliders," Phys. Lett. B **503**, 341 (2001) [arXiv:hep-ph/0101316].

[24] T. Han, H. E. Logan, B. McElrath and L. T. Wang, "Phenomenology of the little Higgs model," Phys. Rev. D **67**, 095004 (2003) [arXiv:hep-ph/0301040].

[25] F. Abe *et al.* [CDF Collaboration], "The Cdf Detector: An Overview," Nucl. Instrum. Meth. A **271**, 387 (1988).

[26] F. Abe *et al.* [CDF Collaboration], "Evidence for top quark production in anti-p p collisions at s**(1/2) = Phys. Rev. Lett. **73**, 225 (1994) [arXiv:hep-ex/9405005].

[27] F. Abe *et al.* [CDF Collaboration], "Evidence for top quark production in anti-p p collisions at s**(1/2) = Phys. Rev. D **50**, 2966 (1994).

[28] F. Abe *et al.* [CDF Collaboration], "Kinematic evidence for top quark pair production in W + multi - jet events Phys. Rev. D **51**, 4623 (1995) [arXiv:hep-ex/9412009].

[29] T. Affolder *et al.* [CDF Collaboration], "Measurement of the top quark mass with the Collider Detector at Fermilab," Phys. Rev. D **63**, 032003 (2001) [arXiv:hep-ex/0006028].

[30] T. Affolder *et al.* [CDF Collaboration], "Measurement of the W boson mass with the Collider Detector at Fermilab," Phys. Rev. D **64**, 052001 (2001) [arXiv:hep-ex/0007044].

[31] K. Hagiwara *et al.* [Particle Data Group Collaboration], "Review Of Particle Physics," Phys. Rev. D **66**, 010001 (2002).

[32] F. Bedeschi *et al.* [CDF Collaboration], "Design And Construction Of The Cdf Central Tracking Chamber," Nucl. Instrum. Meth. A **268**, 50 (1988).

[33] L. Balka *et al.* [CDF Collaboration], "The Cdf Central Electromagnetic Calorimeter," Nucl. Instrum. Meth. A **267**, 272 (1988).

[34] S. Bertolucci *et al.* [CDF Collaboration], "The Cdf Central And Endwall Hadron Calorimeter," Nucl. Instrum. Meth. A **267**, 301 (1988).

[35] K. Byrum *et al.*, "Shower Maximum Trigger For Electrons And Photons At Cdf," Nucl. Instrum. Meth. A **364**, 144 (1995).

[36] F. Abe *et al.* [CDF Collaboration], "A Precision measurement of the prompt photon cross-section in p anti-p Phys. Rev. Lett. **73**, 2662 (1994) [Erratum-ibid. **74**, 1891 (1995)].

[37] K. Byrum *et al.* [CDF Collaboration], "The Cdf Forward Muon System," Nucl. Instrum. Meth. A **268**, 46 (1988).

[38] G. Ascoli *et al.*, "Cdf Central Muon Detector," Nucl. Instrum. Meth. A **268** (1988) 33.

[39] W. Wagner, H. Stadie, T. Arisawa, K. Ikado, K. Maeshima, H. Wenzel and G. Veramendi, "Online monitoring in the CDF II experiment," FERMILAB-CONF-02-269-E *Prepared for International Europhysics Conference on High-Energy Physics (HEP 2001), Budapest, Hungary, 12-18 Jul 2001*

[40] B. Angelos *et al.* [CDF Collaboration], "Online monitoring and module maintenance for CDF in the upcoming Fermilab Tevatron Run II," *Prepared for International Conference on Computing in High-Energy Physics and Nuclear Physics (CHEP 2000), Padova, Italy, 7-11 Feb 2000*

[41] P. Canal *et al.*, "Online monitoring in the upcoming Fermilab Tevatron run-II," IEEE Trans. Nucl. Sci. **47** (2000) 240.

[42] D. Acosta *et al.* [CDF Collaboration], "Measurement of prompt charm meson production cross sections in p anti-p collisions at s**(1/2) = 1.96-TeV," arXiv:hep-ex/0307080.

[43] D. Acosta *et al.* [CDF Collaboration], "Search for the flavor-changing neutral current decay D0 $\rightarrow$ mu+ mu- in p anti-p collisions at s**(1/2) = 1.96-TeV," Phys. Rev. D **68**, 091101 (2003) [arXiv:hep-ex/0308059].

[44] D. Acosta *et al.* [CDF II Collaboration], "Measurement of the mass difference m(D/s+) - m(D+) at CDF II," Phys. Rev. D **68**, 072004 (2003) [arXiv:hep-ex/0310043].

[45] J. M. Campbell and R. K. Ellis, "An update on vector boson pair production at hadron colliders," Phys. Rev. D **60**, 113006 (1999) [arXiv:hep-ph/9905386].

[46] R. Bonciani, S. Catani, M. L. Mangano and P. Nason, "NLL resummation of the heavy-quark hadroproduction cross-section," Nucl. Phys. B **529**, 424 (1998) [arXiv:hep-ph/9801375].

[47] J. C. Collins and D. E. Soper, "Angular Distribution Of Dileptons In High-Energy Hadron Collisions," Phys. Rev. D **16**, 2219 (1977).

[48] J. L. Rosner, "Forward-Backward Asymmetries in Hadronically Produced Lepton Pairs," Phys. Rev. D **54**, 1078 (1996) [arXiv:hep-ph/9512299].

[49] K. D. Lane, "Technihadron production and decay in low-scale technicolor," Phys. Rev. D **60**, 075007 (1999) [arXiv:hep-ph/9903369].